ABSTRACT

EXPERIMENTAL STUDIES OF WAVE PROPAGATION IN THREE-DIMENSIONAL PHOTONIC CRYSTALS

by
John M. Tobias

Photonic crystals were proposed fifteen years ago. Propagation is selectively prevented through these crystals resulting in a photonic band gap, that is, a frequency region where light cannot propagate. These frequency bands are analogous to electronic band gaps in solid-state crystals.

The optical properties of the photonic crystal in regions near the band gap remain relatively unexplored. Yet, there is significant evidence to suggest that this avenue of investigation can provide useful optical and microwave applications. Numerical studies have predicted that the effective permittivity near the photonic band gap approaches zero and becomes negative. Self-collimation of the propagating beam and ultrarefraction, where radiation is redirected through large angles in the crystal, are predicted. Although not considered as the ideal structure, the face centered cubic (fcc) opaline photonic is crystal studied for reasons of practical realization.

The tools to examine the diffraction effects of photonic crystals, and in particular those for three-dimensional structures, are somewhat lacking. To this end, commercial simulation software and a series of experimental studies were employed to gain insight of this unique wave propagation problem.

The emphasis of this study was upon frequency and polarization selectivity based on the azimuthal and incident angles with respect to the crystal morphology. Some of the

results are consistent with calculations for two-dimensional crystals. However, they are demonstrated here in three-dimensional crystals for the first time.

Defect modes, where the photon density of states is modified to allow propagation in a certain direction was also explored. Although not optimized for low loss, significant evidence was found for the existence of defect modes in the fcc crystal.

Modification of the photonic crystal by adding periodic features with negative permittivity (metal) was examined as well. The addition of metal changed the refractive index contrast leading to frequency selective self-imaging beam splitting, as well as modification of the subwavelength self-imaging characteristic length.

It is expected that the experimental data will be useful toward in developing better theoretical approaches for photonic crystalline optics.

EXPERIMENTAL STUDIES OF WAVE PROPAGATION IN THREE-DIMENSIONAL PHOTONIC CRYSTALS

by
John M. Tobias

A Dissertation
Submitted to the Faculty of the
New Jersey Institute of Technology
In Partial Fulfillment of the Requirements for the Degree of
Doctor of Philosophy in Electrical Engineering

Department of Electrical and Computer Engineering

May 2002

APPROVAL PAGE

EXPERIMENTAL STUDIES OF WAVE PROPAGATION IN THREE-DIMENSIONAL PHOTONIC CRYSTALS

John M. Tobias

Apr. 30, 02

Dr. Haim Grebel, Dissertation Advisor — Date
Professor, Department of Electrical and Computer Engineering, NJIT

4/30/02

Dr. Gerald Whitman — Date
Professor, Department of Electrical and Computer Engineering, NJIT

4/30/02

Dr. Gregory A. Kriegsmann — Date
Professor, Department of Mathematical Sciences
Foundation Chair, Applied Mathematics, NJIT

4/30/2002

Dr. John F. Federici — Date
Associate Professor, Department of Physics, NJIT

4/30/2002

Dr. Karl D. Moeller — Date
Research Professor, Department of Physics, NJIT

BIOGRAPHICAL SKETCH

Author: John M. Tobias

Degree: Doctor of Philosophy

Date: May, 2002

Date of Birth:

Place of Birth:

Undergraduate and Graduate Education:

- Doctor of Philosophy in Electrical Engineering,
  New Jersey Institute of Technology, New Jersey, 2002

- Master of Science in Electrical Engineering,
  University of Maryland, Baltimore County, Maryland, 1992

- Bachelor of Science in Physics,
  Seton Hall University, New Jersey, 1987

Major: Electrical Engineering

Publications:

Tobias, J.M. & Grebel, H. (1999).
Self imaging in photonic crystals in a subwavelength range. *Optics Letters*, 24, 1660-1662.

Tobias, J.M., Ajgaonkar, M., & Grebel, H. (2002).
Morphology-dependent Transmission Through Photonic Crystals. Journal of the Optical Society of America B, 19, 385-389.

DEDICATION

With imagination, determination, effort, and endurance, all is possible.

ACKNOWLEDGMENT

Over the past eight years of study, many people and organizations were very helpful in furthering my efforts. First, I would like to recognize and thank Professor Haim Grebel, my Dissertation Advisor, for his patience, wisdom and guidance over the past several years.

Secondly, I would like to thank my dissertation committee, Professors Kriegsmann, Whitman, Federici and Moeller, for their participation and many useful suggestions.

My efforts would not be at all possible without the generous funding support of the United States Army. In particular I would like to recognize Steven Horne and Fernando Mancini for granting time for this endeavor as well as Steven Jakubowski and Kenneth Blum for use of laboratory facilities. I also extend a special recognition and thanks to Mr. Lawrence Goldberg of the Research and Development Center Technical library for his help in locating arcane and ancient technical papers.

Last, but certainly not least, I would like to recognize my wife, Carol, and children, Sarah, Rachel and Daniel, for their encouragement and understanding over the course of the years of this work.

TABLE OF CONTENTS

TABLE OF CONTENTS
(Continued)

Chapter **Page**

TABLE OF CONTENTS
(Continued)

Chapter **Page**

TABLE OF CONTENTS
(Continued)

TABLE OF CONTENTS
(Continued)

Chapter **Page**

LIST OF TABLES

LIST OF FIGURES

LIST OF FIGURES
(Continued)

Figure **Page**

LIST OF FIGURES
(Continued)

Figure **Page**

LIST OF FIGURES
(Continued)

Figure **Page**

LIST OF FIGURES
(Continued)

LIST OF FIGURES
(Continued)

Figure **Page**

LIST OF FIGURES
(Continued)

Figure **Page**

LIST OF FIGURES
(Continued)

Figure **Page**

LIST OF FIGURES
(Continued)

Figure **Page**

CHAPTER 1

INTRODUCTION

1.1 Discussion of the Technical Problem

An enormous proliferation of optical devices has occurred in recent years. Optical devices are now ubiquitous in telecommunication applications. This trend continues into other applications. A major field for the application of optical devices is in integrated optics, the combination of optical and electronic devices, ideally, on one integrated circuit. Major advantages result from this technology, stemming from the large bandwidth of optical waveguides, the lack of inductive effects to disperse signals, and the lack of radiated interference to distort signals. While waveguide applications concentrate on passage of data, there are many other applications for optical devices. For example, another major application is the conversion of optical signals to electrical signals, giving rise to light emission and detection applications.

In the past, optical and electrical devices were made of discrete components. A trend toward integration of optical and electrical devices has occurred in the past ten years. Many specific applications resulted from this trend, for example the now ubiquitous charge-coupled devices used for image acquisition as well as solid-state lasers and detectors used in data storage. Yet, the field of integrated optics, that is, the engineering of optical and electrical devices as a single component, is in its infancy. The key toward development of integrated optics is the understanding of the interaction of radiation with matter. Thus, a major emphasis of this investigation is the propagation and diffraction properties of a relatively new class of materials, the photonic crystal.

In particular, the close-packed face centered cubic (fcc) crystal remains a relatively unexplored area for exploitation as an optical device. Until quite recently, the ability to tailor the fabrication of fcc crystals was limited. However, it is now possible to construct fcc crystals that are custom tailored[1]. Consequently, it is possible to fabricate fcc crystals for use as optical devices and possibly construct effective photonic crystals through a self-assembly process.

Several advantages are apparent from utilization of fcc photonic crystals. In addition to the increasing ease of assembly, large diffraction effects are possible. Consequently, small devices or very thin optical elements are envisioned. Elements with sizes of a few wavelengths of light lend themselves to integration with increasingly smaller solid-state devices. Nano-sized (on the scale of 10^{-9} m) structures for the manipulation of radiation are possible. Ultimately one can imagine applications in lasers, spectroscopy, imaging, wavelength multiplexing and in optical masks for solid-state fabrication.

In the realization of close-packed fcc-structure photonic crystals, parameters available for design are limited. In terms of geometry, the designer is limited to d, the feature size, which in turn limits Λ, the period of the structure. Another aspect of the design geometry is the orientation of the crystal with respect to the radiation propagation direction in the crystal. This aspect has been explored to a large degree by the development of models to predict the photonic band gaps in materials. With the variation of crystal orientation the packing density is not affected, unless the media can be distributed in a filler or matrix of some other material, which also affects Λ.

Consequently, attention is focused upon the close-packed fcc structure. Although

it may be relatively simple to fabricate, this structure poses significant challenges in characterization as a photonic crystal, or even as an optical component, for that matter. Analytical methods have not been developed to account for wave propagation within the crystal. Due to the close packing, electromagnetic simulations fail in providing precise information on the amplitude and phase of the propagating wave. Despite this, simulations were found to be useful in providing general guidance for the conduct of experiments. In addition, the maximum advantage of modern fabrication technology is realized if the elements of the fcc crystal are at the same size or even smaller than the wavelength of the light to be controlled. This also complicates the problem, since simulations do not handle computations in this regime well.

Electromagnetic simulations and numerical methods are not useful without qualification. In the study of past work in the area of photonic crystals, particularly for those operating as optical components, one can find that there remain many unexplored topics. Further, much of the work performed was limited to their stop band properties or was limited to one or two-dimensional crystals. Here, the study is extended to three dimensional crystal structures.

Consequently, this study relies upon the experimental characterization of the fcc crystals where individual crystal element size is on the order of the wavelength of the propagating beam. This characterization is a first step in the development a general theory for propagation in three-dimensional photonic crystals as of well as the ultimate realization of useful devices.

1.2 Literature Review

1.2.1 Diffraction and Gratings

Diffraction arises when electromagnetic waves interact with an obstruction. It has been said that "...an exact solution for a particular diffracting configuration is amongst the most troublesome to be dealt with in optics..."[2]. Despite this formidable statement, it is easy to describe the observable effects of diffraction. A brief review is presented for the reader, however, more detailed references are available[2]. In general, there are two types of diffraction, Fraunhofer and Fresnel diffraction. Consider a situation as illustrated in

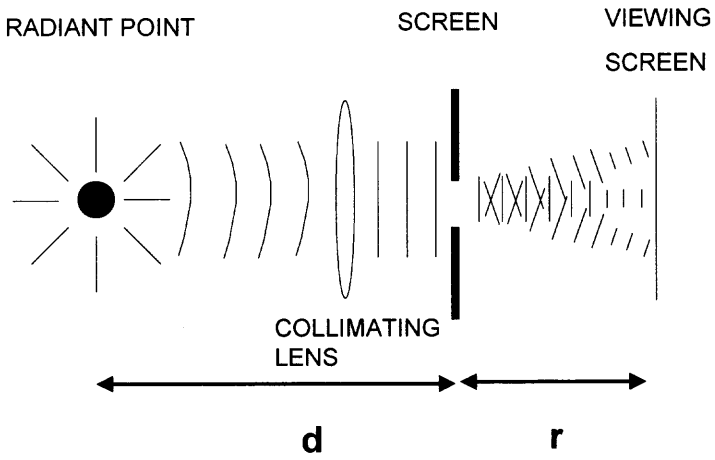

Figure 1.1 Illustration of Fraunhofer diffraction.

Figure 1.1. An opaque screen with an aperture is illuminated by plane waves from a distant radiant point at distance, d. The lens in the figure is there to collimate the beam on the left of the aperture. At the outset, imagine that the viewing screen is very close to the aperture at distance, r. The arrangement projects an image of the aperture upon the viewing screen at right. Close examination would reveal some fringes of light and dark regions about the periphery of the image of the aperture. When the light source is

monochromatic, fringes appear as a result of diffraction by the aperture. For reasons of analytical simplification, one may distinguish between the diffraction pattern in the near-field (close to the aperture) and in the far-field (away from the aperture). The fringes at the periphery of the image of the aperture are an example of Fresnel, or near field, diffraction. Fresnel diffraction is rather complicated and is only solved for simple systems by using graphical means or through tabulated values of the Fresnel integrals. If the screen is moved so that the range, r, becomes very large, a pattern of light and dark regions would remain without the image of the aperture. At this point, moving the screen further away increases the size of the pattern, but would not change the pattern itself. In this case, the screen is exhibiting Fraunhofer, or far field diffraction.

1.2.2 Fraunhofer Diffraction

If the aperture is a single slit of width b and height D, as illustrated in Figure 1.2,

the instantaneous electric field intensity from Fraunhofer diffraction is described by writing:

$$E = \frac{E_L D}{R}\left(\frac{\sin\beta}{\beta}\right)\sin(\omega t - kR) \tag{1.1}$$

where: E_L is the electric field per unit length at the aperture (source strength), D and R are as defined in Figure 1.2, $\omega = 2\pi f$ (angular frequency), $\beta = (kb/2)\sin\theta$, where $k \equiv 2\pi/\lambda$. However, performing actual measurements the irradiance is used, defined as the time average of the square of the electric field, $I(\theta) = c\varepsilon_0\langle E^2\rangle$, expressed in units of watts per square meter^2. Thus, it is possible to write:

$$I(\theta, R) = \frac{c\varepsilon_0}{2}\left(\frac{E_L D}{R}\right)^2\left(\frac{\sin\beta}{\beta}\right)^2 \tag{1.2}$$

as $\sin\beta/\beta = 1$ when $\theta = 0$, let

$$I(0,R) = \frac{c\varepsilon_0}{2}\left(\frac{E_L D}{R}\right)^2 \tag{1.3}$$

assuming R is fixed, the result is:

$$I(\theta) = I(0)\left(\frac{\sin\beta}{\beta}\right)^2 \tag{1.4}$$

This expression can be written more compactly as $I(\theta) = I(0)\text{sinc}^2\beta$.

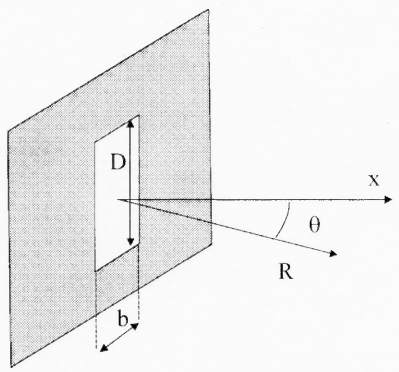

Figure 1.2 Single slit geometry.

If a periodic multiplicity of slits is visualized, at distance, a, between each other, the irradiance pattern[2] can be written:

$$I(\theta) = I_0\left(\frac{\sin\beta}{\beta}\right)^2\left(\frac{\sin N\alpha}{\sin\alpha}\right)^2 \tag{1.5}$$

Note that I_0 is the irradiance at a single slit and $\alpha = 0, \pm\pi, \pm 2\pi, \ldots$. The location of the principal maxima can also be written as:

$$a\sin\theta_m = m\lambda \tag{1.6}$$

where: a is the distance between slits, m = 0, ±1, ±2, ... There will also be subsidiary maxima at locations where sin(Nα) has greatest value. To visualize this, a diffraction pattern and associated geometry is illustrated in Figure 1.3. The vertical axis of the lower graph is the intensity while the horizontal axis is the interval, in units of sinθ, from the center of the diffraction pattern. The pattern is projected onto a screen and the intensity

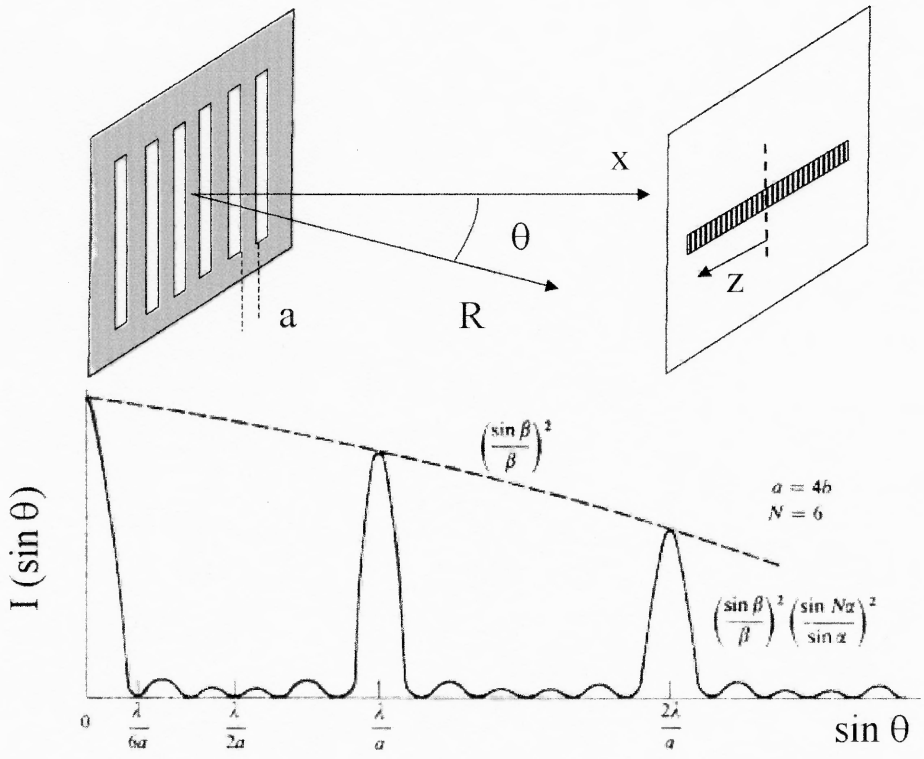

Figure 1.3 Diffraction pattern arising from six slits (N = 6) , spaced at four times the slit width (a = 4b) and the resulting projected pattern.

maxima are periodic along z. Note the decreasing intensity of each principal maxima and the subsidiary maxima in between. Fraunhofer diffraction is observed for other aperture geometries, notably the circular aperture which is the well-known Airy disk.

In this basic description of the Fraunhofer (far field) diffraction, it is noted that there are several approximations (e.g. Fraunhofer approximation) are used in developing

these expressions as well as several assumptions. In the system described by Figure 1.2 it is assumed that $b >> \lambda$ and $R >> d$. Once out of this regime, the Fraunhofer description of diffraction ceases to be valid.

Multiple slit diffraction describes a commonly used optical device, the diffraction grating. This description (Figure 1.3) assumes a transmission grating since the situation lends itself to develop some intuition of the three-dimensional photonic crystal. It is noted that three-dimensional gratings are possible. A three-dimensional diffraction system is manifest in the transmission of x-rays through a crystal resulting in the well-known Laue pattern. Fundamentally, sites of constructive interference result on the Laue pattern where the atomic planes of the crystal obey the Bragg Law, $2a \sin\theta = m\lambda$, where a in this case is the interplanar spacing of the atomic planes. Note that the scale is preserved, that is, the planar spacing is much larger than the wavelength and the ranges are much larger than the crystal size preserving the validity of the Fraunhofer diffraction theory.

1.2.3 Gratings and Filters

Using gratings as filters in optical and microwave applications was proposed some time ago[3]. Using gratings in a waveguide or optical path it is possible to realize high and low pass filters. A series of gratings were found to promote spectral filtering (Ulrich)[3]. Since then, many studies have concentrated on the experimental and theoretical development of this application. As a natural progression, this work led into investigation of arrays of apertures (grids) in opaque screens. Recent work codifies these grids into two categories: inductive and capacitive grids.

Inductive grids[4] are usually realized by the perforation of a metallic opaque screen. Consequently, one can envision the reduced size of the metallic areas between the apertures as inductive elements. (Electromagnetic surface waves, also known as surface plasmons, are discussed in more detail later.) The modification of the surface wave is thought to couple to the wave transmitted through the grating, changing the properties of the transmission. Wood's anomaly (a discontinuity in the reflected diffraction efficiency of a grating with respect to the incident angle) is a well-known consequence of this phenomena routinely observed in gratings.

Capacitive grids[5] are realized by inversion, that is, by separating the conducting elements. Thus, surface waves are modified by the capacitive elements and couple to the transmitted wave in a fashion analogous to the inductive grid.

Intense study of these grids continues to this day and researchers have made analogies between the behavior of these grids and two-dimensional photonic crystals[6]. Recent grating work concentrates on subwavelength features in the gratings.

1.2.4 Subwavelength Features and Gratings

It has been recognized very recently that gratings with subwavelength features can modify a beam transmitted through them. In fact, recent observations of this phenomena have yielded surprising results. In 1998, Ebbesen, observes unusual transmission characteristics[7] through a hexagonal array of subwavelength circular apertures. In exploring the effects of the aperture depth, he notes that the coupling mechanisms through the array are not well understood. Later work by Bomzon demonstrates the use of subwavelength features in transmission dielectric gratings to modify beam polarization[8]. The basis for these effects are attributed by Bomzon to optical singularities

appearing at points where the phase or amplitude either are undefined or have abrupt changes. Despite this recent work, grating effects that are of interest in this study were first explored quite some time ago.

1.2.5 Self-Imaging: Talbot and Rayleigh

Self-imaging occurs when a beam is transmitted through periodic media. At regular intervals of range along the axis of the transmitted rays, images resembling the periodic media can be observed. Earliest observation of the self-imaging effect due to transmission through a periodic media was made by Talbot[9] in the early 19th century. In his series of experiments, Talbot used a darkened room and the most intense light available to him, solar light. The light was reduced to a relatively small point and directed through a mirror to the periodic media. In fact, Talbot described five experiments performed on light transmission through periodic media, the results of which are important and bear discussion in turn.

The first experiment transmitted the solar light through a vertically oriented Fraunhofer grating as illustrated in Figure 1.4. With the grating placed at a range d = 20

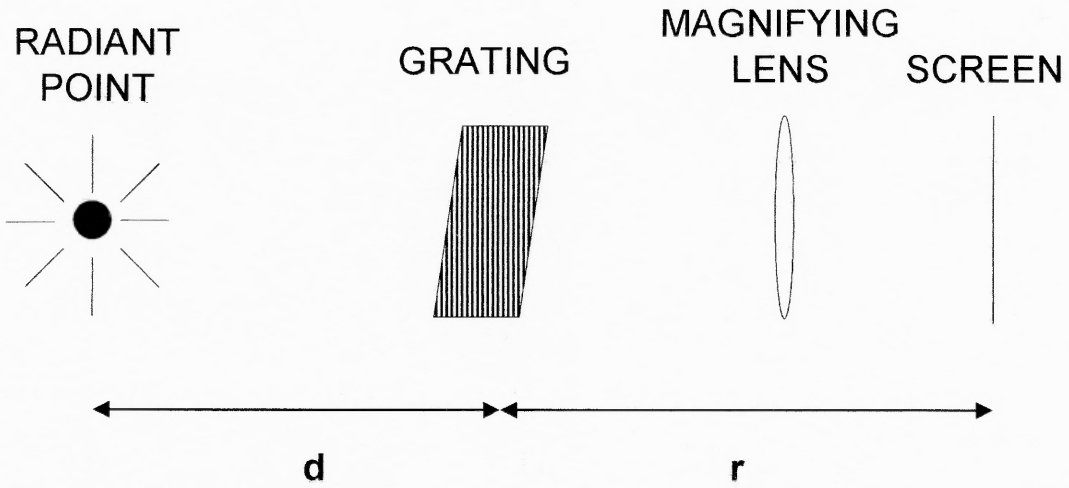

Figure 1.4 Illustration of Talbot's first experiment.

feet and the grating to screen range, r, varied from zero to a few feet, Talbot observed a series of red and green lines parallel to the lines on the grating projected upon the screen. At the range increased, the color of the lines shifted to yellow and blue and thence repeated the pattern out to a range of two feet.

Talbot's second experiment imposed a second grating perpendicular to the first as illustrated in Figure 1.5. A two-dimensional version of the alternating red/green and blue/yellow effects was observed. Talbot describes these as a fabric woven with red and green threads.

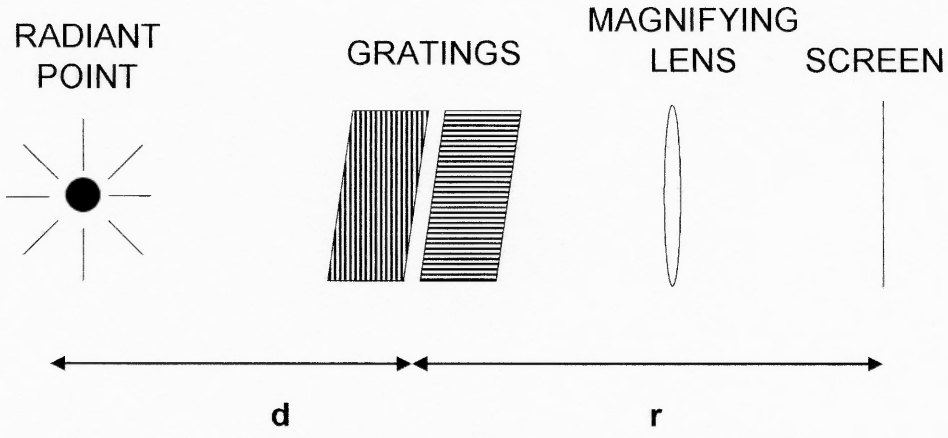

Figure 1.5 Illustration of Talbot's second experiment. A second grating is imposed in the beam perpendicular to the first.

In Talbot's third experiment, an opaque copper plate is substituted in place of the single grating. This plate had several holes of regular periodic spacing and equal diameter drilled into it. As the range, r, varied, the rows of circles were observed with lines separating them. At a particular range of r, close to the plate an image was observed where a spot appeared in each of the circles on the plate, which Talbot attributes to interference, as it was known in his time. In the fourth and fifth experiments, the plate

and lens incident angle was varied with respect to the beam. Talbot notes that various patterns were observed similar to the fabric woven of various colors and that the patterns remain distinct as if in the focus of the lens despite its distance from the lens.

Rayleigh presents the first analysis of the Talbot experiments[10]. The first observations made by Raleigh is that the variation of color as a function of the range, r, denotes that the effect is dependent upon wavelength of the incident light. Consequently, Rayleigh then reproduced Talbot's experiment with monochromatic light. Tabulating his results, (Table 1.1) he documented the positions of best and worst definition for each instance of monochromatic light used.

Rayleigh also notes that the successive image reproduced along the distance (range) from the grating is, in fact, a photographic negative. He first proposes the proportionality of the self-imaging distance (the periodic range between images), to d^2/λ, where d is the period of the grating. This was determined by Rayleigh experimentally as well as analytically.

Table 1.1 Results of Rayleigh's Self-Imaging Experiment

Red light, λ= 0.664 μm*		Green light, λ= 0.576 μm*	
Best	Worst	Best	Worst
1 ¾	3 5/8	1 ¼	3 ¾
5 ¾, 6 ¾	7 ½	6 ¼	8 5/8
10 ¼	12 ½	11	14 ¼
15 1/8	17	16 ½	19 ¾
19 ¾	21 7/8	22 1/8	25 ¼
24 ¾	27	27 ¾	31 ½
29 ¼	32 1/8	33 ¼	37
34 ½	37 ½	-	-
Dimension in inches.			
* Wavelength experimentally determined by Rayleigh.			

Ultimately Rayleigh arrives at the following expression for the self-imaging distance:

$$z = \frac{\lambda}{1 - \sqrt{\left(1 - \frac{\lambda^2}{d^2}\right)}} \tag{1.7}$$

where d is the period of the grating. Since, in this case, $\lambda^2 << d^2$ so that $z = 2d^2/\lambda$, which matched Rayleigh's experimental observations. This expression is recognized as the classical self-imaging distance[11], where z denotes the linear distance from the periodic media where an image forms, also called a *Talbot plane*. Rayleigh pointed out that there may be subordinate periods that are omitted due to the approximations used and more importantly, that this approximation does not rigorously apply to the principal periods themselves, as one might expect from the omission of higher-order effects.

1.2.6 Recent Work in Self-Imaging

Subordinate image planes were revisited by researchers much later. These subordinate images were observed out of the Talbot self-imaging planes. Cowley and Moodie, in their extensive study of Fourier images[12], arrived at the existence of a suborder n, for the image occurring at $z = 2d^2/n\lambda$, where n is an integer. In their development, they considered periodicities of objects comprised of unit cells using squares or rectangles. Early computational work conducted by Rogers hinted at yet other subordinate Talbot planes[13,14] at non-integral values of n, and further suggested that $n = 2/p$, where p is an integer, resulting in $z = d^2/p\lambda$. Further developments using Fresnel optics principles were conducted by Winthrop and Worthington[15] ultimately suggesting the form of $z = \nu(2d^2/\lambda)+\beta(2d^2/\lambda)$, where ν is an integer (including zero) and $\beta = N/n$, where $n = 2N/p$, where N and p are integers.

A recent development in the theory of self-imaging is the formal identification of constructive interference planes to explain all Talbot planes. In the wave-optics treatment by Latimer and Crouse, diffraction modes were correlated by phase difference and examined at the Talbot planes[14]. Modes of the same order produce a stronger self-image while higher order modes produce weaker images. For the sake of completeness, this theory is presented here. The relation given by Latimer and Crouse[14] for the self-imaging distance is:

$$\frac{1}{R_1}+\frac{1}{R_2}=\frac{1}{nT} \tag{1.8}$$

where the variables are determined using a multiple slit grating model as illustrated in Figure 1.6. R_1 is the distance from the light source to the grating and R_2 is the distance from the grating to the Talbot plane. $T = a^2/\lambda$, where a is the distance between each slit, and $n = j^2/q$, where j is an integral multiple of a, found from d, the distance from the center of the grating to the individual slit position, e.g., $j = d/a$, and q is the diffraction order from Bragg's law. For example, the upper slit in Figure 1.6 would have $j = 1$, since it is at a distance of $d = ja$ from the center. The diffraction order is given, in general by the expression:

$$d(\sin\phi+\sin\theta)=m\lambda \tag{1.9}$$

where d is the distance between slits, $d = ja$, φ = incident angle, from normal to the grating, θ = transmitted angle from normal to the grating and m is an integer to express diffraction order. The parameter q is set equal to m in this equation. Notice the possible values of j increases as the extent of the grating increases. These definitions of j and q tend to limit the possible values of n in the expression for the self-imaging distance so there are not an infinite number of possible Talbot planes. Although this is cited as a

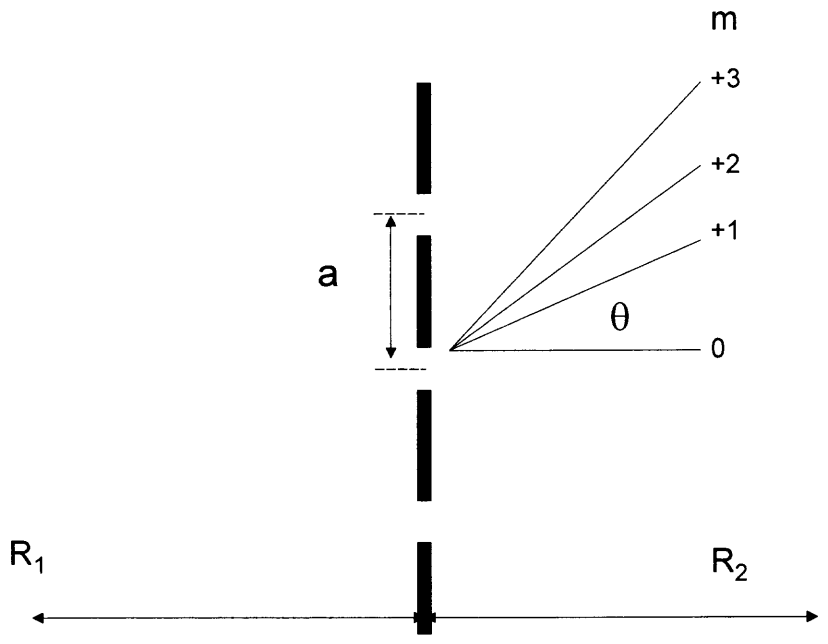

Figure 1.6 Latimer-Crouse Diffraction Model.

general solution to the self-imaging distance, it is a solution based on diffraction concepts and again reaches it's limit where the value of a, as illustrated, approaches the value of λ. Despite this, it remains useful as an explanation for some phenomena.

1.2.7 Applications of Self-Imaging

Self-imaging has found applications in several optical devices. One particular use is application of the self-imaging phenomena in optical waveguides. In it's most basic form, nearly all multimode optical fibers are rudimentary self-imaging devices. Simplest fibers are comprised of a core and cladding, where the index of refraction of the core is greater than that of the cladding. Beyond some angle, light incident on this boundary undergoes total internal reflection and is thus confined to propagation within the fiber core. In this sense, the fiber is self-focusing, yet all of the image information is not

necessarily preserved. Note the distinction that Talbot self-imaging is observed in free space and that a guiding media is not a necessary condition self-imaging, however. Other more sophisticated schemes employ graded-index or step-index fiber. Graded-index fibers operate by providing a gradient of the index of refraction as a function of fiber radius, thus causing internal reflection within the fiber. Similarly, step-index fibers provide a sharp contrast of refractive index. The gradient or contrast of the index of refraction is transverse to the propagation direction. An advantage of multiple index layers is that total internal reflection occurs in a greater range of angles, resulting in less light leaving the fiber core. The graded index provides yet another improvement upon this since its transmission properties generally ensure better preservation of the signal form.

Since the Talbot effect depends on the interaction of propagating modes, it is useful to point out that a variety of periodic, multi-mode interference (MMI) devices have received much attention for optical and microwave applications, recently[16,17]. An example (in one dimension) is the family of transverse Bragg waveguides[18]. The transverse Bragg waveguides achieve mode shaping and self-imaging through the diffraction of higher-order modes from the transverse Bragg planes[19]. The propagating modes interfere in the direction of the beam propagation *along* the diffracting planes. The diffraction pattern is periodic along the direction of propagation.

1.3 Propagation in Periodic Media

A characteristic of periodic media is translational symmetry. The permittivity of a periodic media can be expressed as:

$$\varepsilon(x) = \varepsilon(\mathbf{x} + \mathbf{a}) \tag{1.10}$$

where a is a lattice vector and x is a distance in the crystal across the periodic features. In more than one dimension, **x** and **a** are vectors, ε is the dielectric permittivity tensor. In three-dimensional media, the primitive lattice vectors of the crystal determines the translational invariance of the crystal. Maxwell's equations can be written in the in the general case as:

$$\nabla \times \vec{E} = -j\omega\mu\vec{H} \tag{1.11}$$

$$\nabla \times \vec{H} = j\omega\mu\vec{E} \tag{1.12}$$

Upon substitution of (**x** + **a**) for **x** in Maxwell's equations, the equations remain unchanged and the normal modes of the medium can be written as:

$$\vec{E} = \vec{E}_{\vec{K}}(\vec{x})e^{-i\vec{K}\bullet\vec{x}} \tag{1.13}$$

$$\vec{H} = \vec{H}_{\vec{K}}(\vec{x})e^{-i\vec{K}\bullet\vec{x}} \tag{1.14}$$

and $\mathbf{E_K}$, $\mathbf{H_K}$ are periodic:

$$\vec{E}_{\vec{K}}(\vec{x}) = \vec{E}_{\vec{K}}(\vec{x} + \vec{a}) \tag{1.15}$$

$$\vec{H}_{\vec{K}}(\vec{x}) = \vec{H}_{\vec{K}}(\vec{x} + \vec{a}) \tag{1.16}$$

This concept is known as the Bloch or Floquet theorem[20], where **K** is known as the Bloch wave vector. Consequently, a dispersion relation exists between the frequency ω, and **K**:

$$\omega = \omega(\vec{K}) \tag{1.17}$$

Without further elaboration, one can see that the frequency is dependent upon the value of **K,** a vector. This implies that the direction of the Bloch wave vector affects the propagating mode frequency.

Regions in the frequency domain where **K** becomes complex can exist and the resulting Bloch wave is evanescent. Consequently, like the example of total internal reflection, the wave will be completely reflected and will not propagate in the media. There are only certain spectral bands where propagation can occur for a particular frequency. A simple example is a Bragg reflector, where the reflectivity is dependent upon the angle of incidence. Interpreting this by Bloch theorem, at the incident angles where the reflection is high in the Bragg reflector, the Bloch wavevector is complex, prohibiting propagating modes. (An example of the solution of the Bloch theorem applied to propagating modes in the one-dimensional Bragg mirror case can be found in *Optical Waves in Crystals* by Yariv[20].)

Calculation of this dispersion relation for periodic media is not trivial, especially for three-dimensional crystal systems and is the topic of much research in photonic crystals. So far, numerical methods can calculate band diagrams for some three-dimensional crystal systems, but the Bloch formalism does not necessarily apply in the finite crystal cases that will be experimentally studied.

It is possible to qualitatively describe the performance of a simple periodic structure that will provide some insight into the physics of the photonic crystals studied. In Figure 1.7, a waveguide is illustrated of a dielectric guiding region and a region of alternating dielectric contrast that comprises the well-known transverse Bragg reflector.

The Bragg reflector is an example of one-dimensional periodic media. When the Bragg condition, $m\lambda = 2\Lambda\cos\theta$ (where Λ is the period and θ is the incident angle) is fulfilled for non-normal incidence to the Bragg reflector region, constructive interference in reflection occurs. Ultimately, the Bragg condition is an integral number of wavelengths between reflected rays from successive dielectric (or lattice, in a three-dimensional crystal) planes.

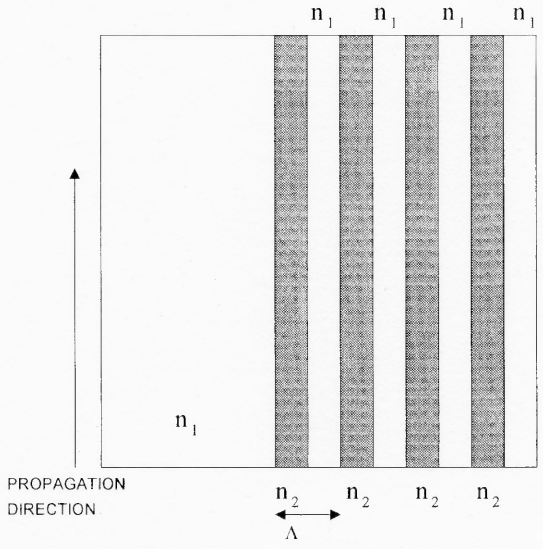

Figure 1.7 Asymmetrical transverse Bragg reflection waveguide.

When light is coupled into the waveguide, the guiding (slab) region has particular propagating constants permitting modes of propagation. Light leaving the guiding region and entering the Bragg reflector region is going either to fall within the band gap (of the Bragg reflector) and be entirely reflected back into the guiding region, or escape through the Bragg reflector. By engineering the period of the Bragg reflector dimensions of the waveguide and the dielectric contrast, mode shaping and self-imaging can be achieved[19].

A simple example is illustrated in Figure 1.8. In the example, a low-order even mode is illustrated. Assuming the central guiding region will support multimode propagation, one can easily imagine the superposition of several modes and the consequent effect on self-imaging location and intensity. By extension of this basic concept to three dimensions, it is expected that similar effects can be achieved. Adding periodicity in the direction of propagation transforms the problem from a multimode interference (MMI) device like the transverse Bragg waveguide to a new class of materials termed photonic crystals.

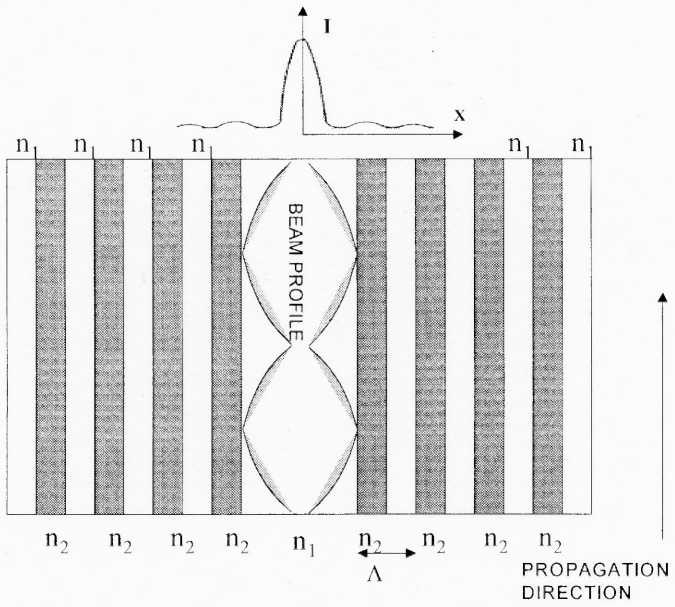

Figure 1.8 Beam propagation in the transverse Bragg waveguide. A particular mode (in this example a low-order even mode) will be confined to the guiding region by total internal reflection and attenuation of the x-components in the Bragg reflector regions.

1.4 Literature Review of Photonic Crystal

1.4.1 Introduction

Photonic crystals were recently proposed as a method to control light propagation[21]. These crystals are regular, repeating arrays of contrasting dielectric materials. Many

photonic crystal realizations are possible but, in general, one can categorize them in terms of the dimensions in which periodicity is exhibited. For example, in Figure 1.9, a one-dimensional photonic crystal has a periodic dielectric contrast relative to one axis only as in the Bragg reflector. Even with the relatively simple one-dimensional crystal all of the effects of a photonic crystal can be explored, as the all of the essential properties of the crystal are manifest. This distinction brings up a fine point in the definition of photonic crystal. In order for the crystal to exhibit a photonic bandgap, the media must have a periodic contrast in the direction of propagation.

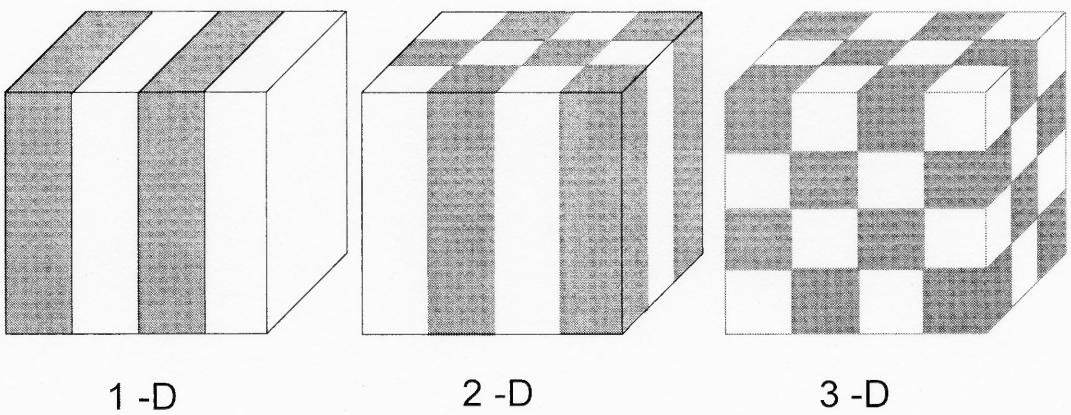

Figure 1.9 Representative photonic crystals illustrating periodicity and dielectric contrast.

In Figure 1.9, the one-dimensional crystal must have radiation propagating through it in a direction normal to the contrasting dielectric planes for any of the photonic crystal effects to appear. Thus, the transverse Bragg waveguides do not fall within the definition of a photonic crystal device, at least not for impinging plane waves. On the other hand, devices utilizing multilayered dielectric films are familiar, such as the quarter-wave stack (Bragg reflector) commonly utilized for frequency-selective, high-quality reflection. Once the transition is made from transverse one-dimensional crystal

architecture to a two or three-dimensional architecture, the photonic crystal effect becomes the major contributor to the propagation qualities of the crystal. The exact nature of these qualities are not fully known. Several properties have been predicted or identified by researchers in photonic crystal. These effects include the existence of a photonic bandgap, photon localization and superprism, or ultrarefractive effects.

1.4.2 Photonic Bandgap

A major goal of photonic crystal research to date has been the identification and characterization of a crystal structure with a complete photonic band gap, that is, a crystal that prevents wave propagation in all directions through the crystal. A complete photonic bandgap is useful, since the familiar quarter wave stack is limited to near-normal reflection – a three-dimensional photonic crystal would be highly reflective at any incident angle.

Without computing a bandgap, it is possible to deduce the nature of the effect of the crystal on a radiation field by recalling $c=\lambda_0 f$ and defining the wavenumber, $k= 2\pi/\lambda_0$. It then follows that the angular frequency is given by: $\omega=ck$, an equation known as the dispersion relation of the radiation field in free space. The density of states[22] of the propagating fields is proportional to an arbitrary volume, V, of free space and the frequency, ω, of the field:

$$D(\omega) \propto \frac{\omega^2 V}{\pi^2 c^3} \tag{1.18}$$

In a dielectric media of refractive index, n, the properties of the radiation field are modified. The propagation speed of the radiation field in the media, becomes the phase velocity, $\upsilon_p = c/n$, and the effective wavelength in the media becomes $\lambda_n = \lambda_0/n$.

Consequently, the value of ω is replaced by ω_n and c is replaced by υ_p in the density of states equation and $D(\omega)$ changes. Another technique to change $D(\omega)$ is to place contrasting dielectrics in a periodic arrangement.

Placement of the periodic dielectric contrast in the direction of propagation results in a photonic crystal, by definition. In some realizations, the crystal can be engineered to have a zero density of states at particular frequencies, which prevents propagation of the radiation field. In this region, there is no solution for the eigenvalue equations governing the wave propagation through the media. This region of zero density of states is termed a photonic bandgap. A complete photonic bandgap results when there is a photonic bandgap at a particular frequency for all axes of the crystal. An example of a photonic bandgap diagram illustrating a complete photonic bandgap is in Figure 1.10.

Initial discussion of the existence of the photonic bandgap was in the context of the construction of electrooptical devices, notably lasers, solar cells and transistors. From the initial identification of the concept[23] by Yablonovich in 1987, attention was turned toward utilizing the fcc structure in photonic crystal applications. A primary reason for this was the extensive study of electron bandgaps in semiconductors. Even at this early juncture of photonic crystal exploration, the analogous behavior of electron waves in semiconductors to electromagnetic waves was evident. The fcc case was intensively studied due to it's electronic bandgap properties and was well-known, thus making it a logical candidate for a photonic crystal realization. Yet, at the outset, some important differences were identified[21]. These differences have roots in the nature of approximations used in the band theory of solid-state materials. The primary differences identified by Yablonovitch were:

1) Dispersion relations for electrons are parabolic, while for photons the dispersion relations are linear.

2) The vector wave mathematics play a major role in the photonic bandgap theory. Contrast this to scalar wave approximations used for electronics. Ultimately the difference in electron spin and photon spin is the reason for this difference.

3) Electron band theory is approximate due to the neglect of electronic repulsion. Absence of photon interaction makes the photonic bandgap theory more exact.

After making these significant points concerning the nature of the photonic bandgap, a trial and error approach was taken to identify the photonic bandgap in fcc material using microwave techniques. The primary result of this effort was the identification of a photonic bandgap in a material of high relative permittivity with a

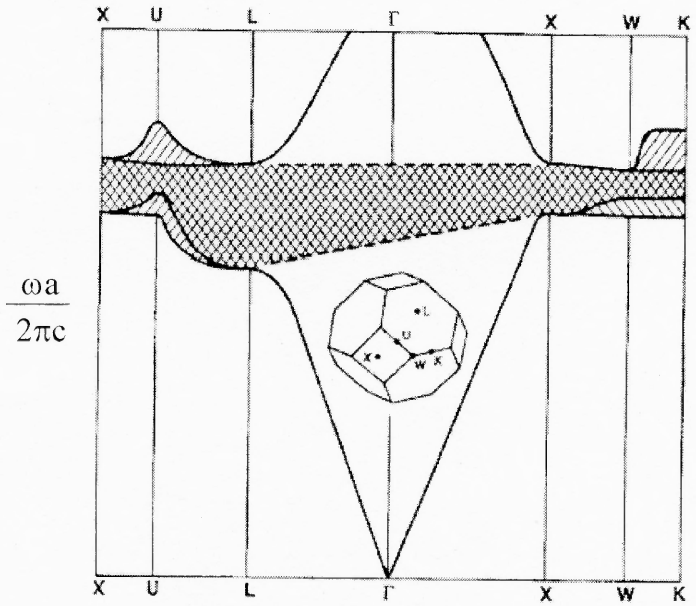

Figure 1.10 Example of a photonic bandgap, in this case, the complete photonic bandgap identified by Yablonovitch. Essentially, $\partial\omega(k)/\partial k$ (dispersion function) is plotted as a function of crystalline direction. The vertical axis is in terms of normalized frequency, $\omega a/2\pi c$. The horizontal axis relates the planes on the Brillouin zone of the crystal. The cross-hatched region is where k are prohibited. Thus, in this example, the k vectors are frustrated for all directions through the crystal since the gap extends across the irreducible Brillouin zone of the crystal.

close-packed fcc arrangement of spherical "air atoms." (The technique of using a high permittivity material as the majority bulk volume is sometimes termed "contrast inversion.") Similar experiments with photonic "atoms" of high relative permittivity fcc spheres in close-packed arrangements did not yield a bandgap[21]. This concept of using "air atoms" was further developed into optical-scale fcc structures with non-spherical features with improved complete photonic bandgaps,[24] but only with higher-contrast crystals. Typically, the contrast had to be in excess of 3:1 for the existence of significant bandgaps. Despite the emphasis on identification of a complete photonic bandgap, other properties of the photonic crystal are proving worthy of interest.

1.4.3 Photon Localization

John, citing the work of Yablonovitch, predicted that the bandgap in photonic crystals would lead to the experimental observation of photon localization[25]. A feature of this premise was the existence of some level of disorder in the lattice. Since the initial work by John, defect modes have been demonstrated by simulation[26] and experimentally[22]. Essentially, a defect mode is caused by the introduction of a controlled disorder in the periodic lattice. This controlled disorder changes the local periodicity and consequently the local photon density of states in the crystal. The presence of the bandgap is essential for photon localization. If the disorder is placed such that it allows an eigenmode solution for an electromagnetic wave in the bandgap of the crystal, localization of the wave in the crystal occurs. An example of the possibilities of such localization are predicted by Mekis in 1996, where nearly lossless transmission of radiation around low-radius bends is postulated by application of numerical methods. A further suggestion of this work is that unique modes may exist at the defect discontinuity such that a bound

localization may occur, in effect a trapping of the radiation. This "self-trapping" is also demonstrated[27].

1.4.4 Ultrarefraction

Quite recently, some other aspects of the effects of photonic crystals have come under scrutiny. Ultrarefraction, also termed "superprism," is an interesting effect that implies a radically changed refractive index beyond what one would expect based on estimating the bulk of the media by volume fraction. Lin reports a highly dispersive prism[28] operating in a frequency regime near the photonic bandgap. Larger than expected dispersion was measured when compared with classical expectations. According to this work, the effective index of refraction n_{eff}, increases in nonlinear fashion as the frequency approaches the photonic bandgap. Initial reports of "superprism" phenomena[29] were published in 1998. In this work, Kosaka reports "extraordinary angle-sensitive light propagation," where a change of a beam incident angle of 7° resulted in a 70° change in the output direction. Further, the paths showed bending contrary to the direction expected by application of Snell's Law, implying a negative index of refraction.

Modification of the group velocity is the proposed mechanism for this effect, as opposed to Lin's expectation of nonlinear n_{eff}. Further investigation into this effect by Enoch, et. al., reveals some theoretical basis[30] for these effects since the permittivity at the bandgap edges can approach zero and become a purely imaginary number inside the gap. One would expect that the refractive index inside the bandgap is a negative real number, but since the media is lossless, it must become imaginary. Enoch demonstrates the theory in numerical simulations conducted on two-dimensional photonic crystal. Several physical effects on the beam should be evident from the numerical predictions.

One predicted effect is a transmission analogy to the Goos-Hanschen effect[2], a larger than expected translation of the output beam from a crystal, compared to the location of the input beam. Another prediction from this work is an extreme beam widening or a splitting into separate emergent beams.

Following the initial reports of wide angular shift and numerical prediction of ultrarefractive effects, a self-collimation effect was also reported[31] by Kosaka. This work details beam dispersion within the photonic crystal as a function of the incident angle of the input beam. Under certain combinations of crystal direction and incident angle, a low loss collimating waveguide effect is observed through the crystal. The theoretical rationale for this effect is the incident wavevectors impinging on the dispersion surface of the photonic crystal. Kosaka contends that since the propagation of light in photonic

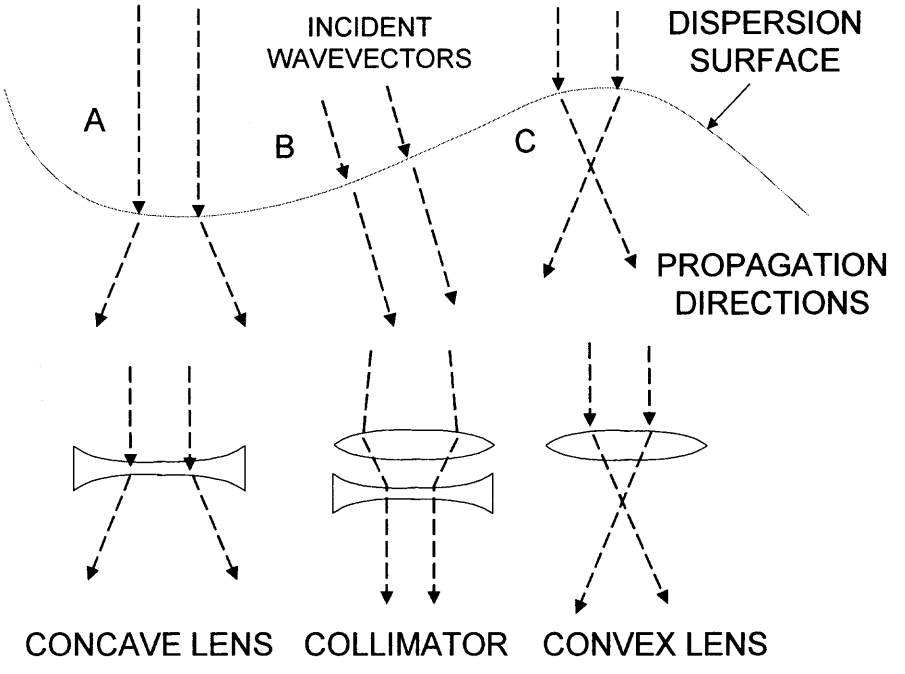

Figure 1.11 Illustration of relationship of incident wavevectors, dispersion surface and propagation directions (energy flow), with analogous conventional optical case, after Kosaka[13]. Propagation occurs normal to the dispersion surface.

crystal is governed by dispersion surfaces, or by the photonic bandgap (this corresponds to the index ellipsoid in conventional crystal optics) there is a region of the dispersion surface that will support self-collimation. Propagation direction is normal to the dispersion surface, under the circumstance that the group velocity and the energy velocity are the same when integrated over a crystal unit cell[31]. Kosaka depicts the possible situations as being analogous to optical components, reproduced here in Figure 1.11. Although the self-collimation case is illustrated by situation B in the figure, note case C, in which a beam incident with the dispersion surface acts as an analogue to a convex lens. Kosaka demonstrated that the transition between lensing and collimation was closely dependent upon frequency of the radiation and its incident angle upon the crystal.

1.4.5 Variation of Azimuthal Angle

Despite the investigation of the effect of incident angle variation on the beam propagation, azimuthal angle variation remained somewhat unexplored. As will be demonstrated, simulations in use for the prediction of photonic bandgaps do not predict development of bandgaps based on azimuthal orientation. Yet, recent work[32] demonstrates that different azimuthal orientation of finite photonic crystal (that is, crystals with dimensions on the order of a few wavelengths) does impact the beam transmission. This experimental work is amplified by a recent study based on numerical methods that predicts that ultrarefraction, or superprism, effects may occur with a dependency on the azimuthal angle of the fcc crystal[33].

Consider that the theoretical or numerical developments usually consider either infinite crystal, or more specifically a unit cell of an infinite crystal. It has been demonstrated that methods developed based on Bloch modes, which find common

application in simulation of photonic crystal, do not account for the physical realities of finite crystal[34]. Crystal finiteness is more realistic for many applications, especially for the realization of on-chip optical components where area is at a premium. The effect is thought to come from variation of the transverse modal propagation characteristics with respect to beam polarization. As the crystal is rotated about the propagation direction, the propagation of the transverse component of the wavevector is alternatively prohibited or permitted which affects the overall transmission.

CHAPTER 2

ELECTROMAGNETIC SIMULATIONS

To assist in the prediction of experimental behavior and to help design better experiments, electromagnetic simulation techniques were used. Simulations help in mapping the electric field for any "slice" of the structure, whereas the experiments possess a limited spatial resolution for obvious physical reasons.

Another reason for the use of simulation in this work is to answer the question of qualification, that is, how well the simulation matches the experiments. Simulations are critical design tools for complex systems such as photonic crystals. If it is possible to demonstrate the suitability of an existing simulation, then a powerful design tool for future research or for realization of device applications is acquired. Especially, in light of the fact that at this writing, general laws for photon crystalline optics have not been formulated.

2.1 Hewlett Packard High Frequency Structure Simulator

In this effort, a commercial simulation package was used, the Hewlett Packard High Frequency Structure Simulator (HPHFSS). The advantage of this approach is that the package has been well tested and verified as an accurate tool for many electromagnetic problems. HPHFSS lends itself to the construction of complicated structures via a computer-assisted drawing (CAD) interface, making it ideal for the realization of fcc crystal. Another significant advantage to this model, unlike many photonic crystal simulations, is that it uses the entire structure rather than a unit cell of the crystal.

HPHFSS employs the finite element method to solve the wave equation in three dimensions, with the ability to map the resultant fields. In general, the finite element method divides the full problem space into thousands of smaller regions and represents the field in each sub-region (element) with a local function. In HPHFSS, the geometric model is automatically divided into a large number of tetrahedra, where a single tetrahedron is formed by four equilateral triangles. This collection of tetrahedra is referred to as the finite element mesh. The value of a vector field quantity (such as the H-field or the E-field) at points inside each tetrahedron is interpolated from the vertices of the tetrahedron. At each vertex, HPHFSS stores the components of the field that are tangential to the three edges of the tetrahedron. In addition, the component of the vector field at the midpoint of selected edges that is tangential to a face and normal to the edge can also be stored. The field inside each tetrahedron is interpolated from these nodal values, thus a field can be calculated for the whole structure.

2.1.1 Inherent Limitations of the Finite Mesh Element

Although the HPHFSS poses several advantages, there are disadvantages as well. The primary disadvantage results from the implementation of the finite mesh elements used. Intuitively, it is apparent that as the interstitial spaces between contrasting dielectric features become smaller, a large number of tetrahedra are required to resolve the structure. This, in turn, leads to two problems. First is a problem of convergence and accuracy. If the mesh is too small, the computation will take excessive time to converge, or it will not converge at all. If the tetrahedra are too large, the result will be inaccurate. Determining an ideal mesh size was largely a process of trial and error. The second problem is computational limits of the hardware. If the mesh size is too small, the

program memory or the software itself will reach its physical limit before convergence, crashing the HPHFSS. Since the finite element method is iterative, the solution process is memory intensive. In the implementation, the physical memory exceeded the program limits making the software itself the limiting factor.

Despite this, it is easy to exceed the software limitations with these types of structures. In close-packed fcc structures, the spheres are in contact – a very bad situation for implementation of finite element mesh. The combination of curvature and close-packing made the HPHFSS quickly exceed its limits. Luckily, the overall size of the structures was generally not larger than a few wavelengths of the propagation wavelength used, so physical size limitations were self-enforcing. Nevertheless, since the HPHFSS remained a useful tool, some adjustments were necessary in order to control the number of tetrahedra used in the finite element solver. Progressive implementation of the controls proved helpful in reducing the size of the computational problem.

The first control was to use an approximate sphere. The spheres in the fcc media were approximated by a multifaceted polyhedron. This reduced the number of tetrahedra used in the HPHFSS by more clearly defining points of media contrast making the mesh generation algorithm force larger tetrahedra. A second control implemented was increased intersphere spacing thereby increasing the crystallographic period, Λ, of the structure. This is, unfortunately, a critical parameter in photonic crystals, so there will be some sacrifice in accuracy. To this end, the results are monitored as a function of crystallographic period, Λ. The final control was to take a one-quarter slice of the structure and impose appropriate periodic boundary conditions.

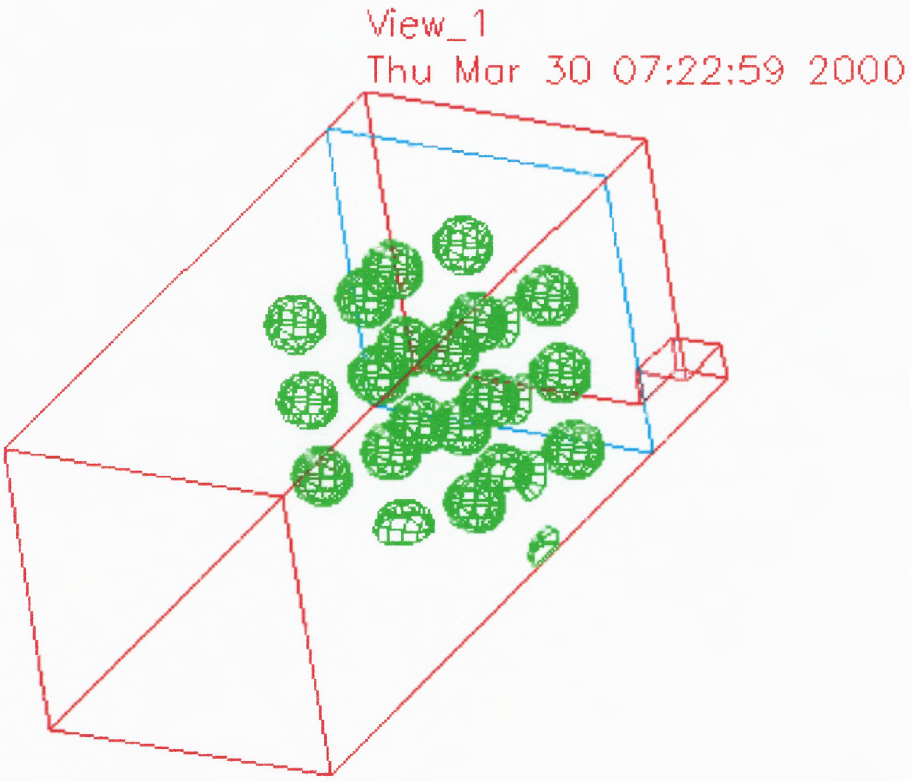

Figure 2.1 A sample structure realized in HPHFSS.

At the conclusion of this process, structures similar to the one depicted in Figure 2.1 were realized. Further controls were explored, such as manual reduction of the number of tetrahedra from the default numbers but, in general, this was not used due to an expected decrease in accuracy. At each stage, power conservation laws are checked with software and manually to verify accuracy. Despite these measures, it was not unusual for the simulation to run for several hours before producing a result, limiting the throughput of the simulation process.

2.1.2 HPHFSS Structures

An explanation of the HPHFSS structures is in order to better understand the simulation. Referring to Figure 2.1, the dielectric spheres are depicted in green. Once the sphere dimensions are defined, they can be realized in any material desired. Only the relative permittivity with respect to air is adjusted. In the figure, the spheres are arranged in an expanded fcc structure with the crystallographic period of $\Lambda = 1.5d_{sphere}$.

Boundary definition in the structure is critical due to the relatively small size, compared to the wavelength. In Figure 2.1, the red box defines the structure space. For the larger section of the structure, the outer surfaces bounded by the red lines are absorptive (called radiation boundaries in HPHFSS nomenclature), in essence immersing the dielectric media in an anechoic chamber. This necessity for accurate portrayal of the transmission through the crystal was first identified by Yablonovitch[21], thus it is recognized that it is essential to eliminate reflections in the structure. Since the simulation takes a one-quarter slice of the entire structure along the propagation direction, the horizontal bottom surface is a perfect conductor and the vertical surface at the front of the view is a perfect magnetic boundary (which forces the H-field to be normal to it) to match the electric field polarization of the input radiation. Input electric field was polarized vertically with respect to the structure. The source of radiation is a waveguide, detailed by the short stub outlined in red at the "front" of the structure (extreme right in the figure) that was bounded by perfect conductors. Having a short waveguide input, rather than just a direct port into the structure, is a technique necessary in HPHFSS to eliminate decaying modes that might interfere with field maps. (There is also a software issue concerning matching of port sizes into the media.) Some simulation

trials showed that these modes decay quite rapidly and thus almost any length of waveguide suffices for the purpose. Generally, a length of 10 mm to 20 mm is used. A map of the electric field magnitude can be taken for any cross-section of the structure. An example of a typical cross-section is outlined in light blue in Figure 2.1.

2.2 Simulation Results

2.2.1 Observations of the Electric Field Magnitude in the Crystal

A primary use of simulation is to gain physical insight of the system behavior. Thus, the three-dimensional fcc structure, within the limitations described, was the subject of a series of simulations to determine the effect of frequency variation and contrast variation on propagation through the crystal. An illustration is presented at Figure 2.2.

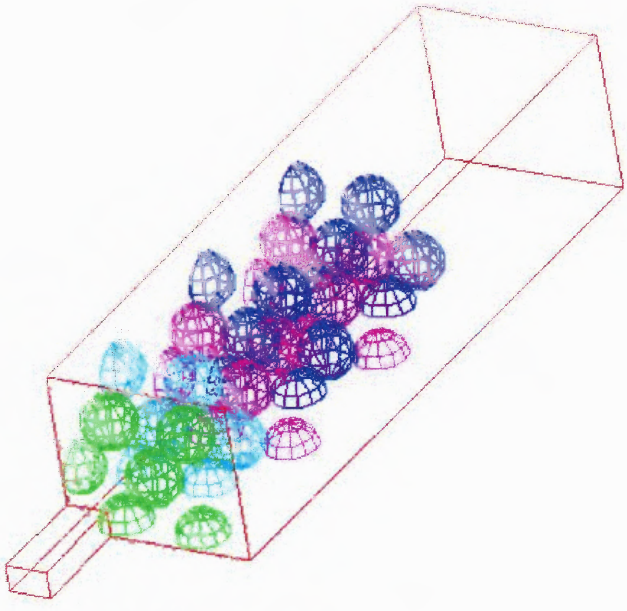

Figure 2.2 6-layer "expanded" fcc structure.

Despite the limitations imposed by the HPHFSS computational method, the simulation can yield useful insights. Figure 2.3 illustrates a typical result of the HPHFSS, a series of cross-sectional plots of the electric field magnitude for particular ranges within the crystal along the propagation direction. For easier visualization, the electric field magnitude at the center of each cross-section can be plotted as a function of propagation distance.

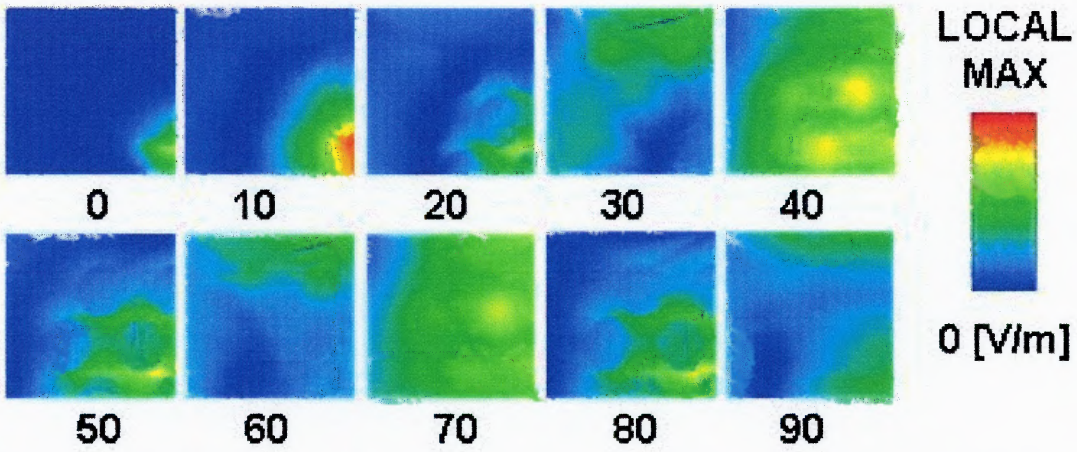

Figure 2.3 HFSS cross-sections depicting electric field magnitude in structure at 10 mm intervals along the direction of propagation. (f = 5 GHz, d_{sphere} = 10 mm, n = 1.5) Scale is depicted to the right, however the cross-sections are not normalized to each other. Thus each has it's own maximum on individual scales, although dark blue is always zero.

Overall, the simulations will show that Rayleigh's predictions for focusing within a periodic media generally hold where $\lambda/\Lambda < 1$. However, a periodic focusing occurs where $\lambda/\Lambda > 1$ and further, the periodic focusing occurs at intervals less than λ. This periodic focusing is similar to Talbot self-imaging.

Figures 2.4a-c depict the center E-field values as a function of range in the structure at frequencies of 5, 10 and 15 GHz respectively. The initial peak at the zero point is attributed to the launching source (waveguide) at the crystal surface (111).

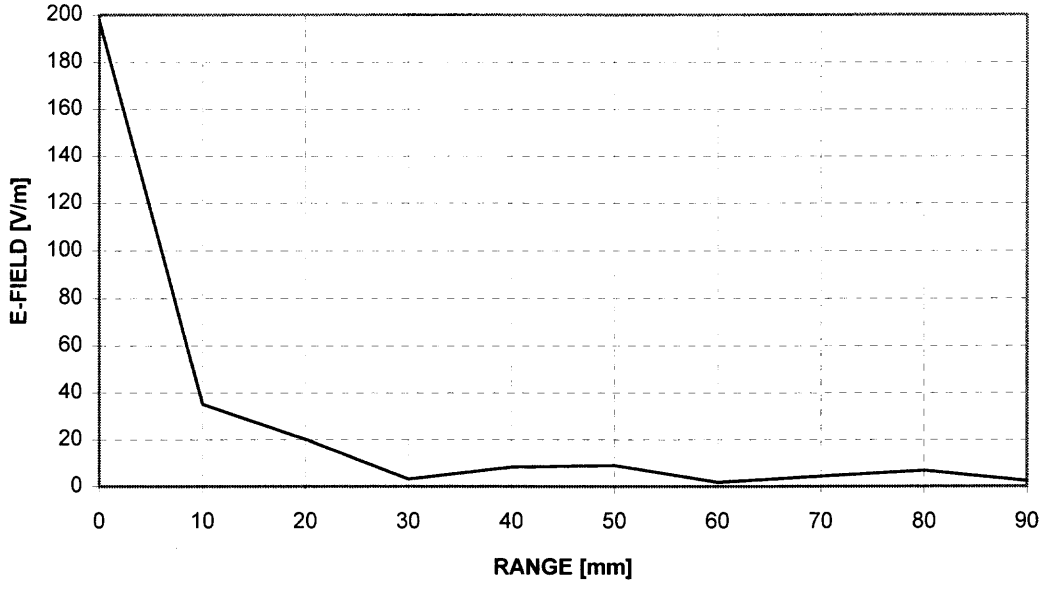

Figure 2.4a HPHFSS result for transmittance as a function of range within the crystal, f = 5 GHz, n = 1.5, d_{sphere} = 10 mm, 6-layer media.

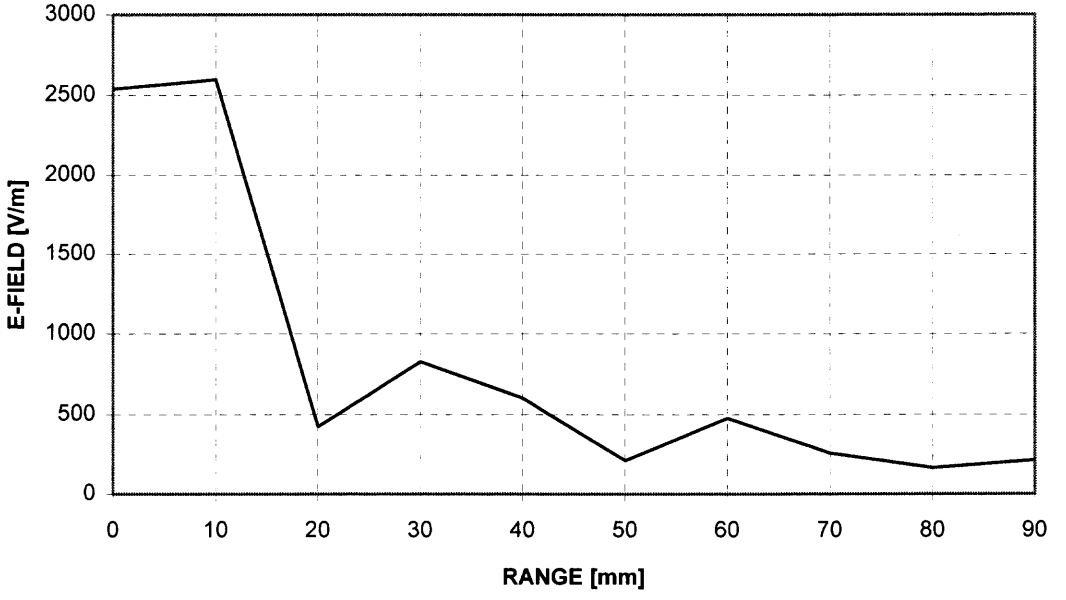

Figure 2.4b HPHFSS result for transmittance as a function of range within the crystal, f = 10 GHz, n = 1.5, d_{sphere} = 10 mm, 6-layer media.

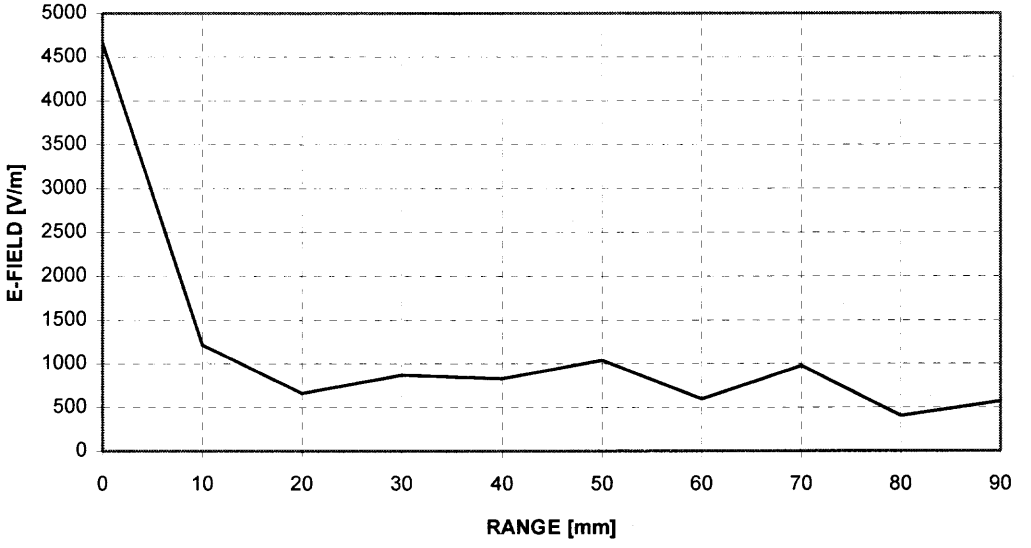

Figure 2.4c HPHFSS result for transmittance as a function of range within the crystal, f = 15 GHz, n = 1.5, d_{sphere} = 10 mm, 6-layer media.

Then the wave quickly loses energy to scattering finally reaching a steady state with periodic variations.

These periodic variations are indicative of focusing and defocusing of the propagating beam. To reinforce this point, the data is normalized and replotted in Figure 2.5a-c. In these plots a "spot size" is shown, defined here as the fractional portion of the structure cross-section that showed a non-zero electric field. The distinction between regions of zero field were very sharp in the simulation, making this comparison convenient compared to a full-width at half maximum, or similar criteria. Notice that the normalized "spot size" can be unity, which generally signifies a relatively uniform field across the structure. Electric field magnitude is normalized by using the maximum value in the respective frequency range (local max). Thus, an electric field maxima combined

with a spot size minima at a particular range signifies an intensity peak. Finally, the data is expressed in terms of intensity in Figure 2.6 for 5, 10 and 15 GHz. The 5 GHz plots show a weak but clear periodicity at approximately a 40 mm range. At 10 GHz the periodicity is approximately 30 mm, and it becomes 20 mm at 15 GHz. At 15 GHz, the effect is markedly weaker. Although both the E-field data and spot size data suggest periodic maxima, or images of the source radiation, but the E-field maxima and spot minima are not always co-located with respect to the range in the media. This may suggest differences in the depth of field of the image or may reflect that the cross-sections chosen to examine the field magnitude may not be exactly on the E-field maxima or spot size minima. In this regard, the accuracy of imaging distance in the simulation is +/- 5 mm.

Two items that the simulation data thus far suggest are:

1) Simulation findings are contrary to the expectation that the self-imaging distance, Ls $\propto d^2/\lambda$. An increase in the self-imaging distance is observed as the wavelength is increased.

2) Subwavelength imaging occurs in the media. Given that at 5 GHz, $\lambda = 60$ mm or $\lambda_n \sim$ 45 mm, (recall that the filling fraction of the simulated structure is low) the Ls $< \lambda_n$.

2.2.2 Variation of Refractive Index of the Spheres

In order to understand the scattering in photonic crystal the index of refraction of the spheres was varied to assess the effect on the self-imaging distance, Ls. The expectation from Rayleigh's development is Ls $\propto d^2/\lambda$. However, in adapting the relationship to the crystalline structure (where there is a crystallographic period, Λ) this relationship must be

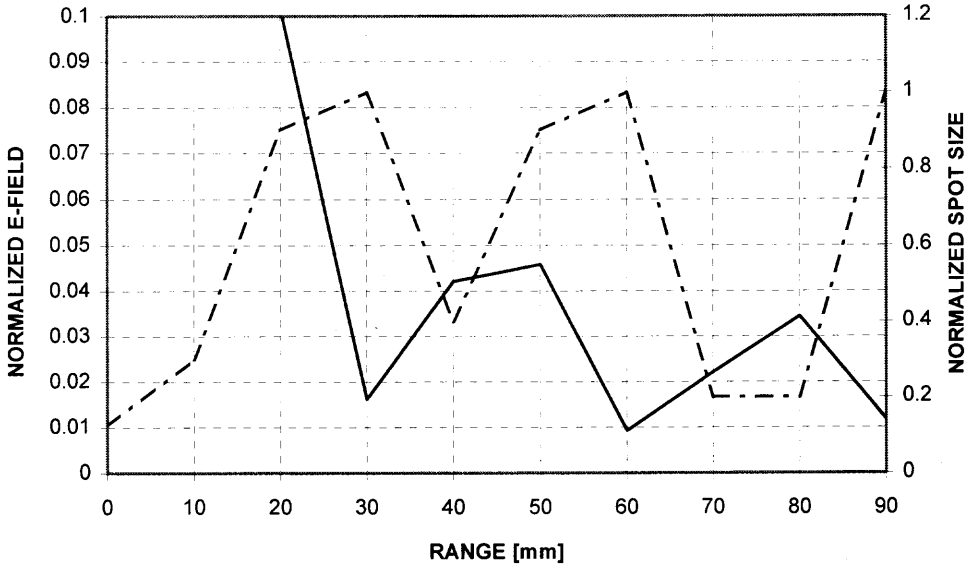

Figure 2.5a Plot of normalized electric field and normalized spot size (dotted line), n = 1.5, f = 5 GHz, d_{sphere} = 10 mm.

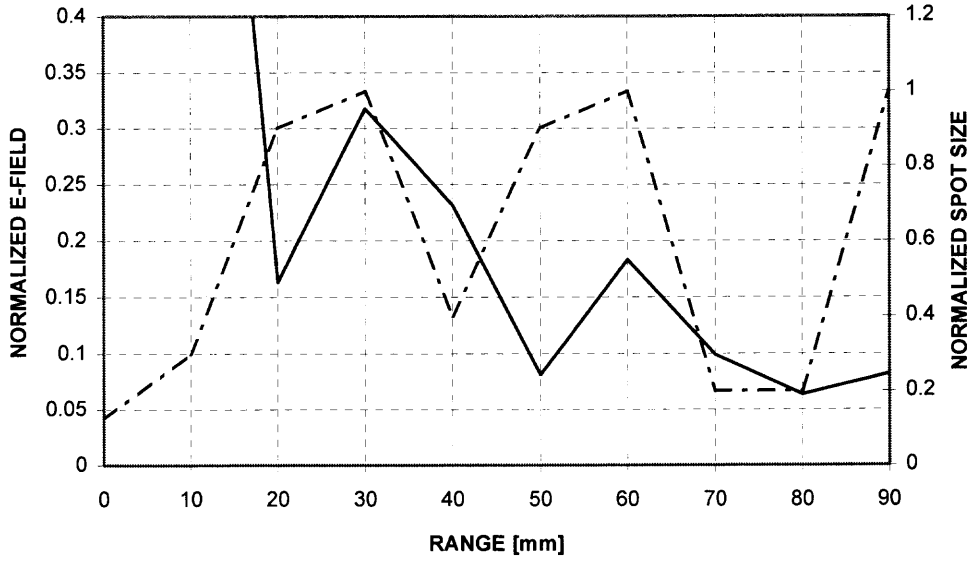

Figure 2.5b Plot of normalized electric field and normalized spot size (dotted line), n = 1.5 f = 10 GHz, d_{sphere} = 10 mm.

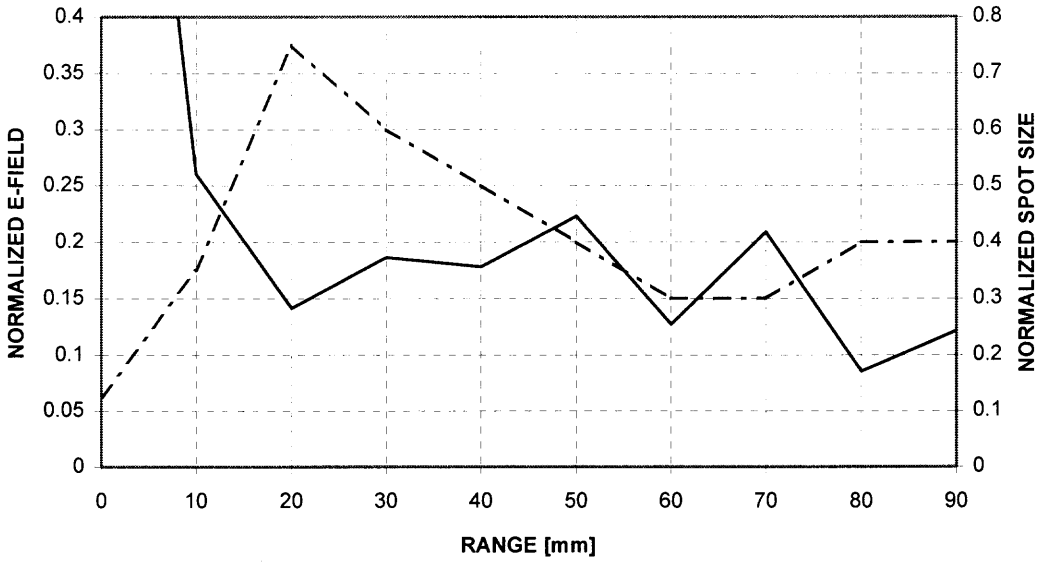

Figure 2.5c Plot of normalized electric field and normalized spot size (dotted line), n_{sphere} = 1.5, f = 15 GHz, d_{sphere} = 10 mm.

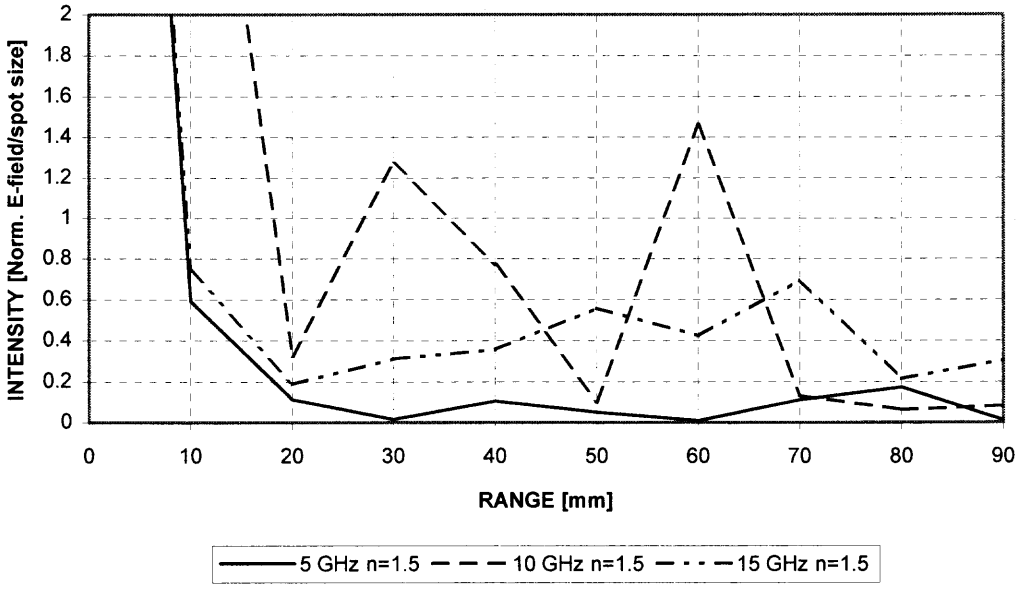

Figure 2.6 Intensity plot (normalized E-field/spot size) for n_{sphere} = 1.5, at 5, 10 and 15 GHz, d_{sphere} = 10 mm.

rewritten as $Ls \propto \Lambda^2/\lambda_{neff}$, where $\lambda_{neff} = \lambda/n_{eff}$. Here the *effective index of refraction*, n_{eff}, which is based on the filling fraction (volumetric fraction) of the dielectric media must be noted. Thus, it is expected the self-imaging distance to increase proportionally to n_{eff}.

Simulation results are plotted in Figures 2.7a-c. At 5 GHz, the increasing n_{sphere}, (consequently increasing n_{eff}) actually leads to a decrease in the self-imaging distance, Ls, from approximately 40-50 mm to 30 mm. E-field peaks are also stronger at $n_{sphere} = 2.5$ than $n_{sphere} = 1.5$. For 10 GHz, the change is marked, but not as clear. A noticeable shift in position of the E-field peak also occurs, however, the magnitude of the peaks are much less at $n_{sphere} = 2.5$ in comparison to $n_{sphere} = 1.5$. Consequently, it is much more difficult to judge the self-imaging distance. For 10 GHz, the self-imaging distance appears to be the same, 30 mm or is possibly indeterminate. The self-imaging range for 15 GHz, $n_{sphere} = 2.5$ is also not clear. It is possible that the self-imaging distance becomes larger than the available range of the experiment. In Figure 2.6, note that the weak E-field maxima at 20 mm intervals (which is cited as the self-imaging distance) becomes a single large intensity maxima at 60 – 70 mm.

An observation worth noting at this juncture is that the 10 – 15 GHz range represents a transition region where the radiation wavelength is becoming comparable to the feature size. At $n_{sphere} = 1.5$, 5 GHz, the wavelength ($\lambda = 60$ mm or $\lambda_{n\ sphere} = 40$ mm or $\lambda_{neff} = 45.5$ mm) is much larger than the feature size d = 10 mm or $\Lambda \sim 8$ mm. At 10 GHz, $\lambda = 30$ mm, $\lambda_{n\ sphere} = 25$ mm and $\lambda_{neff} = 23$ mm using the $n_{sphere} = 1.5$. ($\lambda_{n\ sphere}$ is a less important parameter, since it is the wavelength within the bulk material which is observed here.) As the index of refraction increases, the wavelength in media becomes shorter.

In the particular case of f = 10 GHz, note that the self-imaging distance, Ls, is quite distinctive where n_{sphere} = 1.5 (λ_{neff} = 23 mm) but vanishes, or possibly shifts outside of the observation range where n_{sphere} = 2.5 (λ_{neff} = 15 mm). At 10 GHz, n_{sphere} = 2.5, an E-field maxima is noticed at the x = 20 mm and x = 60 mm ranges citing a possible self-imaging distance of 40 mm, larger that that observed when the $\lambda > \Lambda$. From these results in the $\lambda < \Lambda$ region, it is observed that the Rayleigh relationship of $Ls \propto \Lambda^2/\lambda$ may hold true. A summary of the observations is presented in Table 2.1.

Table 2.1 Simulation Results for Self-Image Formation

f [GHz]	λ (λ_{neff}) [mm]	Ls [mm]	λ/Λ (λ_{neff}/Λ)	n_{sphere} (n_{eff})	REMARKS
5	60.0 (45.5)	40	7.35 (5.58)	1.5 (1.3)	Distinct subwavelength imaging
10	30.0 (22.7)	30	3.67 (2.78)	1.5 (1.3)	
15	20.0 (15.4)	20	2.45 (1.88)	1.5 (1.3)	Small maxima at 20 mm range, larger single maxima at 60 mm. Predicted Ls $\cong$ 30 mm
5	60.0 (30.0)	30	7.35 (3.68)	2.5 (2.0)	
10	30.0 (15.0)	40	3.68 (1.83)	2.5 (2.0)	Predicted Ls $\cong$ 30 mm.
15	20.0 (10.0)	70	2.45 (1.22)	2.5 (2.0)	

However, when λ_{neff} is considered, there is some discrepancy. It is useful to point out again that the Rayleigh approximation was for a thin grating rather than a thick crystal, so a relationship based on λ is valid. However, in the three dimensional crystal described, it is necessary to consider the λ_{neff}.

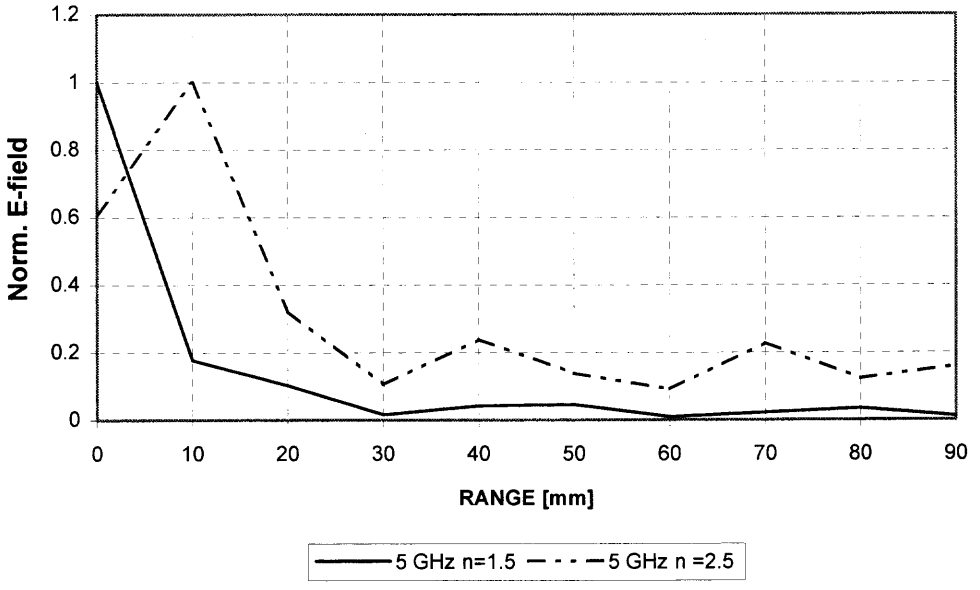

Figure 2.7a Comparison of HPHFSS normalized E-field values for 5 GHz, d_{sphere} = 10 mm, n_{sphere} = 1.5 and n_{sphere} = 2.5 (dashed line).

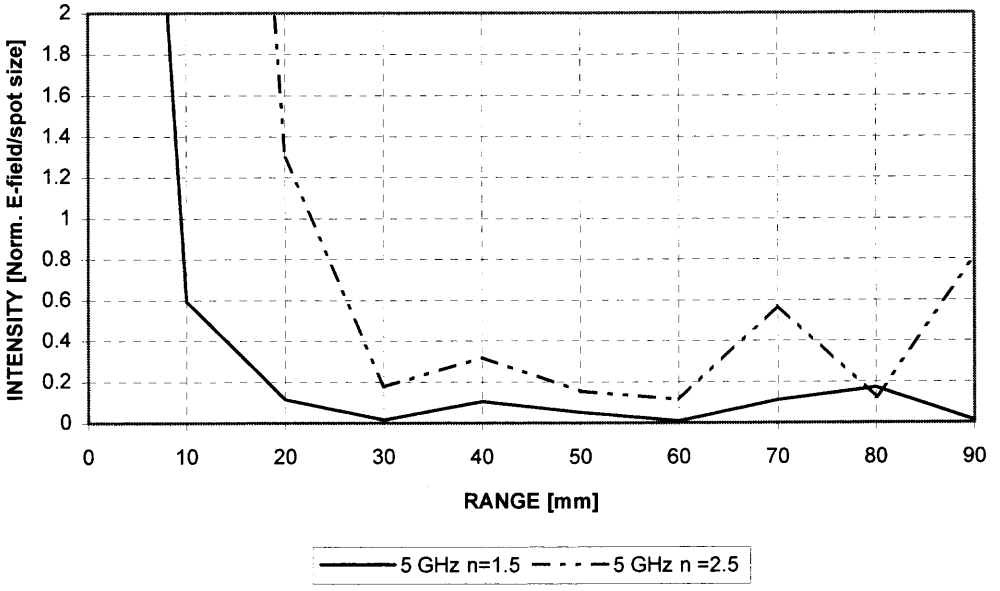

Figure 2.7b Comparison of HPHFSS intensity values for 5 GHz, d_{sphere} = 10 mm, n_{sphere} = 1.5 and n_{sphere} = 2.5 (dashed line).

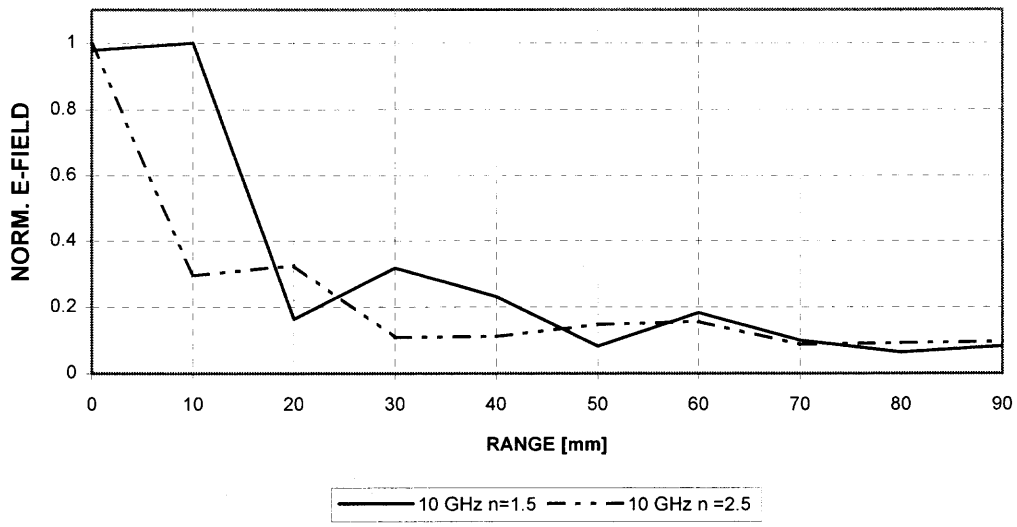

Figure 2.8a Comparison of HPHFSS normalized E-field values for 10 GHz, d_{sphere} = 10 mm, n_{sphere} = 1.5 and n_{sphere} = 2.5 (dashed line).

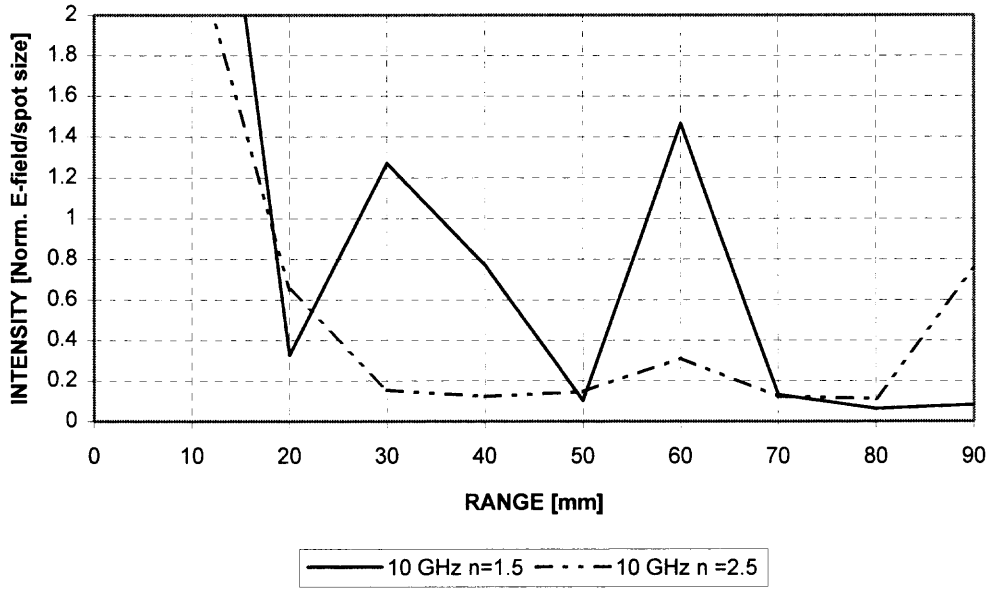

Figure 2.8b Comparison of HPHFSS intensity values for 10 GHz, d_{sphere} = 10 mm, n_{sphere} = 1.5 and n_{sphere} = 2.5 (dashed line).

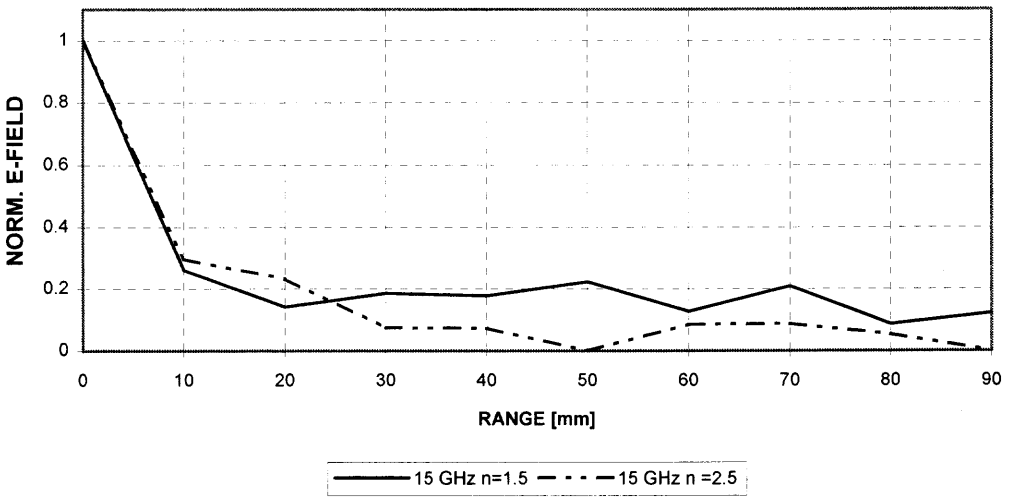

Figure 2.9a Comparison of HPHFSS normalized E-field values for 15 GHz, d_{sphere} = 10 mm, n_{sphere} = 1.5 and n_{sphere} = 2.5 (dashed line).

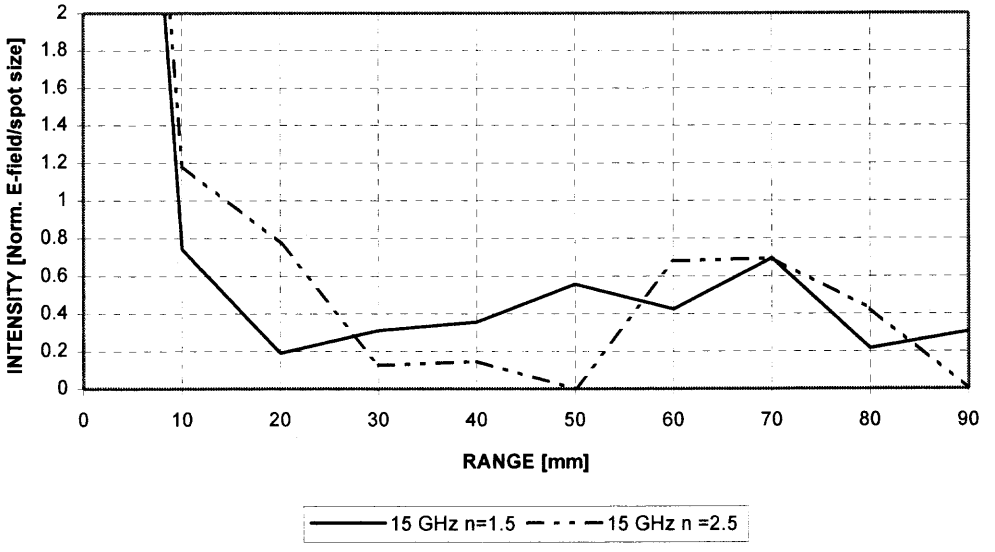

Figure 2.9b Comparison of HPHFSS intensity values for 15 GHz, d_{sphere} = 10 mm, n_{sphere} = 1.5 and n_{sphere} = 2.5 (dashed line).

Consider since the relationship $Ls \propto \Lambda^2/\lambda_{neff} = \Lambda^2 n_{eff}/\lambda$, review of Table 2.1 reveals that the increase in n_{eff} at 5 GHz does not increase the self-imaging distance one would expect from the Rayleigh relationship.

2.3 Summary of Electric Field Magnitude Simulation

The simulation was useful to determine some basic characteristics of the system despite the larger Λ than the close-packed fcc system. Overall findings are:

1) Self-imaging occurs generally as predicted by Rayleigh for $\lambda/\Lambda < 1$.

2) Self-imaging occurs for $\lambda/\Lambda > 1$ but its mechanism might be different than that predicted by Rayleigh.

3) In the subwavelength region ($\lambda/\Lambda > 1$), there is no longer a direct proportionality between the refractive index and the self-imaging distance.

Consequently, an object of the experimental program is to verify these findings overall and extend them, if possible, to the close packed fcc crystal system.

2.4 Variation of Structure Orientation with Respect to Polarization

2.4.1 Introduction

The HPHFSS simulation was used in an attempt to gather information on the behavior of the crystal when its orientation was varied with respect to the polarization of the input beam. The general configuration as depicted in Figure 2.10 was used, where the azimuthal angle, ϕ, is varied with respect to beam polarization, which is in the z-direction. The plane of incidence is the (111) face of the crystal. A two-layer structure was chosen since it matched the self-imaging distances for $n_{sphere} = 1.5$, determined

earlier, so that most of the energy could be collected at a central point eliminating the need to evaluate the entire surface. At the outset, the symmetry of transmission properties is intuitively expected at 60° or 120° intervals when it is rotated about the axis of propagation direction, matching the fcc system crystal symmetry.

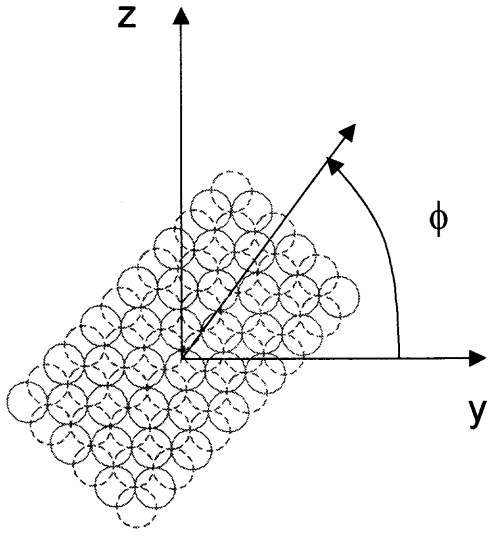

Figure 2.10 Simulation coordinates. A fcc structure comprised of spherical media was rotated with respect to the azimuthal angle, ϕ. Propagation was along the x-axis, into the crystal (111) face.

2.4.2 Construction of the Simulation

The structure was an expanded fcc structure as depicted in Figure 2.11. The starting point for the construction of each simulation was a full waveguide cross-section. Within the boundaries of the simulation space, the spherical media was structured in the fcc configuration and then rotated about the centerline (corresponding to the centerline of the waveguide input) at 15° increments. After rotation, the structure was then sliced into a one-quarter section. As in the previous simulations the inner x-y boundary was a "perfect electric conductor" and the inner x-z boundary was a "perfect magnetic

conductor" to use the method of images for the emulation of the entire waveguide cross- section. The other outer boundaries were made to be "radiation" (nonreflective or perfectly absorptive) boundaries. Figure 2.11 illustrates the result for $\phi = 75°$.

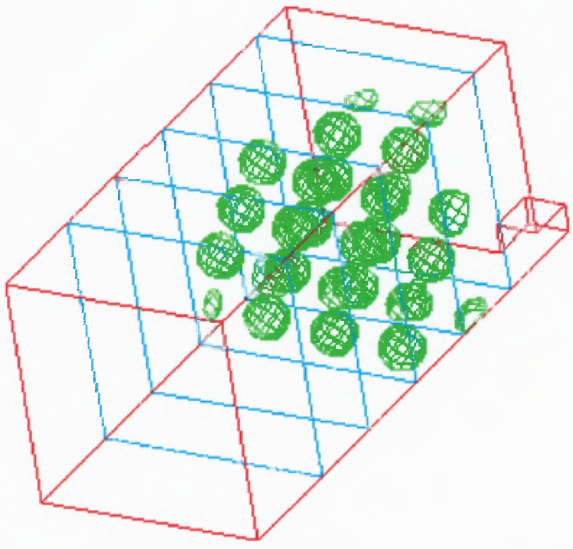

Figure 2.11 Sample HFSS Structure. Media is rotated 75° with respect to beam polarization.

2.5 Simulation Results for Azimuthal Variation

2.5.1 Analysis for 10 mm Diameter Spheres

As the crystal was rotated through $\phi = 0° - 180°$, significant variations of the E-field magnitude were noticed, as illustrated in Figures 2.12a-c. Strong variations in the transmission are noted for each frequency. Small changes were noted at f = 5 GHz, where there can be seen a series of small maxima of approximately 10 V/m in the E-field at intervals of $\phi = 30° - 45°$. This was approximately 20% of the average field value over the entire range of ϕ. Periodicity of transmission at intervals of $\phi = 30°$ is also noted

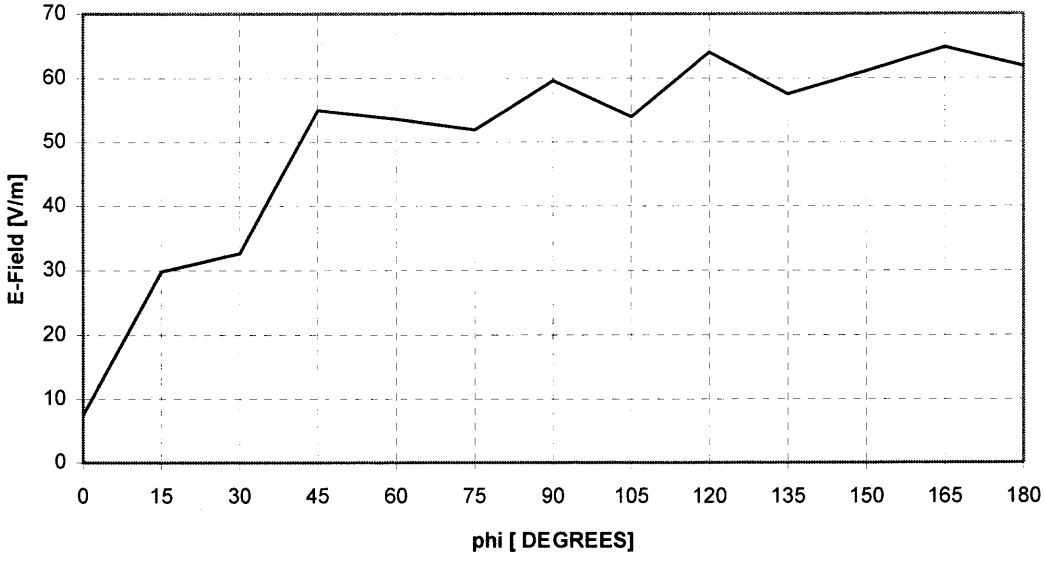

Figure 2.12a E-field with respect to ϕ, f = 5 GHz, d_{sphere} = 10 mm, n = 1.5, 2 layers.

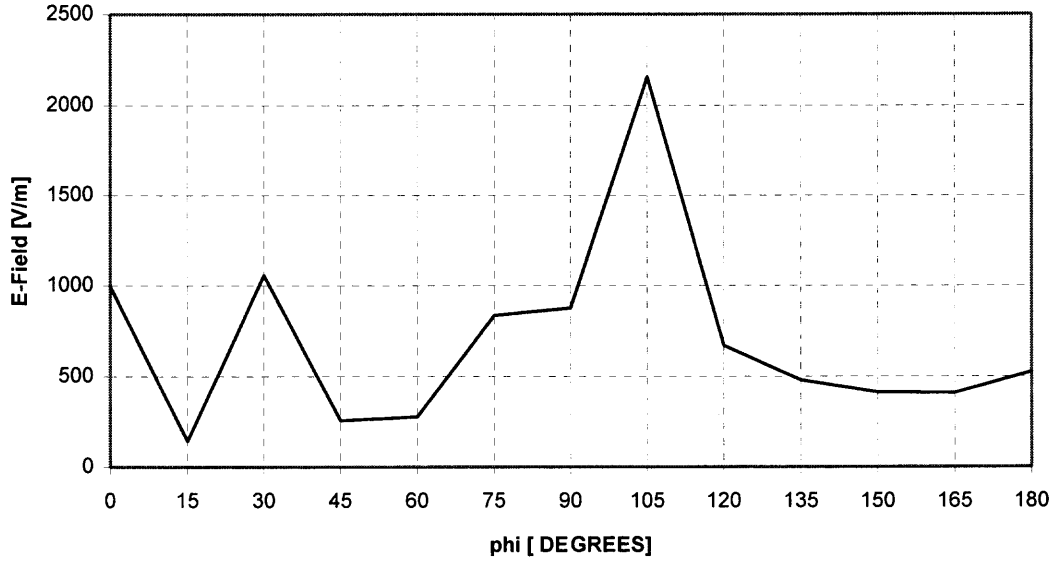

Figure 2.12b E-field with respect to ϕ, f = 10 GHz, d_{sphere} = 10 mm, n = 1.5, 2 layers.

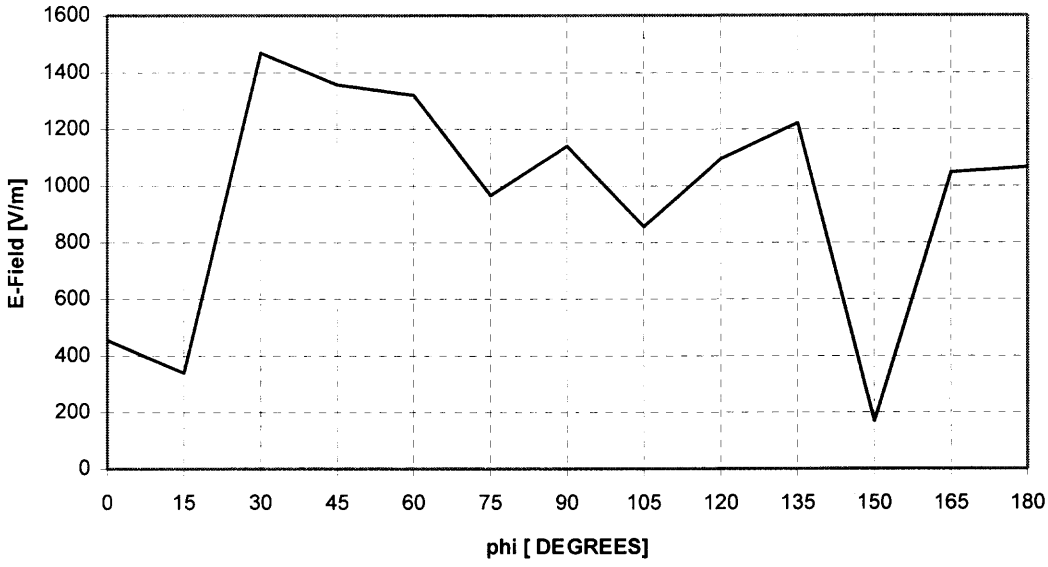

Figure 2.12c E-field with respect to ϕ, f = 15 GHz, d_{sphere} = 10 mm, n = 1.5, 2 layers.

in the data at f = 15 GHz, in addition to two distinct stop bands at ϕ = 15° and 150°. Data for f = 10 GHz are somewhat puzzling, as it shows no distinct periodicity and a single transmission maxima at 105°. As such, it is difficult to draw a conclusion from the 10 GHz result, although scattering may be a dominant mechanism in this case. Since the wavelength of the incident beam is close to the media periodicity (Λ ~ 12 mm to 17 mm depending on orientation with respect to polarization), much of the energy may be strongly scattered and consequently, lost to the observer. Note, that the media period Λ changes while the rotating the crystal and maintaining a fixed polarization direction of the input beam. Interplanar distances change in the z-direction along the beam polarization direction and may consequently enhance or disrupt scattering.

2.5.2 Discussion of the Simulation of the FCC Structure with 10 mm Diameter Spheres

Examination of the fcc system via other simulation techniques by other researchers does not predict azimuthal orientation of the crystal having an effect like this on the transmission[35, 36]. Relatively small periodic maxima in the E-field transmission might be explained by averaging errors or some other artifact in the simulation software. Yet, the large variations as a function of azimuthal angle (20% and greater of the overall scale) cannot be dismissed as artifacts. Typically, other models use effective media concept of a unit cell of the crystal. An effective media model accounts for only layers of the effective permittivity. Such an approach is not sensitive to the local details of the structure. Similarly, other models account for only the irreducible Brillouin zone of the crystal, thus only the section of fcc crystal from 0° - 60° is considered due to the symmetry. The HPHFSS simulation, despite its inherent limitations, performs finite-element boundary computations for the entire structure accounting for those details. Hence, the finite size effects may appear in the HPHFSS simulation. In contrast, the crystal thickness recognized by some other software is semi-infinite making it impossible to detect layer-by-layer variations.

Knowing this, it can be noted that within the crystal there are two major lateral directions related to the polarization sensitivity, these are the <100> and <110> crystal directions. The <100> direction is visualized easily as the direction along an edge of the crystal unit cell, while the <110> direction is a diagonal across the face of the fcc unit cell. In the model used in this simulation, propagation is made along the <111> direction (body diagonal across the crystal unit cell). Since the <100> and <110> crystal directions

possess periodicities that differ by $\sqrt{2}$ one may assume that azimuthal symmetries will have a period of $\Delta\phi = 45°$.

2.5.3 Change of Simulation Scale to Vary λ/Λ

It appears that the ratio λ/Λ plays a significant role in the self-imaging distance. In order to more thoroughly explore the effect of the beam polarization on transmission, the role of the ratio λ/Λ, and to facilitate experimental studies, the scale of the simulation was changed. While the frequency range remained in the 5 – 15 GHz region, the size of spherical media was changed to d = 31 mm and the experiment repeated for both two and four layers. Note that the ratio of $\lambda/\Lambda \approx 2$ is nearly matched by both the simulation results for f = 15 GHz, d = 10 mm and f = 5 GHz, d = 31 mm. Table 2.2 summarizes the λ/Λ ratios used in this simulation.

Table 2.2 λ/d Ratios at Frequencies of Interest

f [GHz]	λ [mm]	λ_{neff} [mm]	λ/Λ, d = 10 mm	λ_{neff}/Λ, d = 10 mm	λ/Λ, d = 31 mm	λ_{neff}/Λ, d = 31 mm
5	60	45.5	7.35	5.58	2.37	1.80
10	30	22.7	3.68	2.78	1.19	0.90
15	20	15.4	2.45	1.88	0.79	0.61

Another viewpoint to assess the self-imaging property of the crystal is to define a quality factor used in holographic (e.g. self-imaging) waveguides[19]. This is given by:

$$Q = 2\pi\lambda(Ls)/(n_{eff}\, d^2) \qquad (2.1)$$

where d is the width of the central guiding channel of the waveguide. The quality factor defines if the hologram is "thin" ($Q < 10$) or "thick" ($Q > 10$). If d is replaced with Λ in equation 2.1, it is possible to estimate the Q factor for these structures. In doing so, the self-images of thin holograms ($Q < 10$) are at 15 GHz, d = 10 mm (which is quite close to

Q = 10) and at 10 GHz and 15 GHz, d = 31 mm. Overall, this distinction reinforces the concept of a transition point as the λ/Λ ratio approaches unity.

2.5.4 Simulation for Sphere Size of d = 31 mm, n = 1.5

Much stronger periodicity is noted for 5 GHz, d_{sphere} = 31 mm than the 5 GHz, d_{sphere} = 10 mm results. Note that the $\lambda_{neff}/\Lambda \approx 2$ for d_{sphere} = 31 mm case. It is appropriate to compare it to the f = 15 GHz, d_{sphere} = 10 mm case based on the λ/Λ ratio. Making this comparison, similarities are found in that four periodic maxima appear at intervals of approximately 30° - 45° in both cases. At 10 GHz, two distinct maxima appear at 45° intervals from each other, but is not periodic through the range of ϕ. At 15 GHz, periodicity at 45° intervals appears to return.

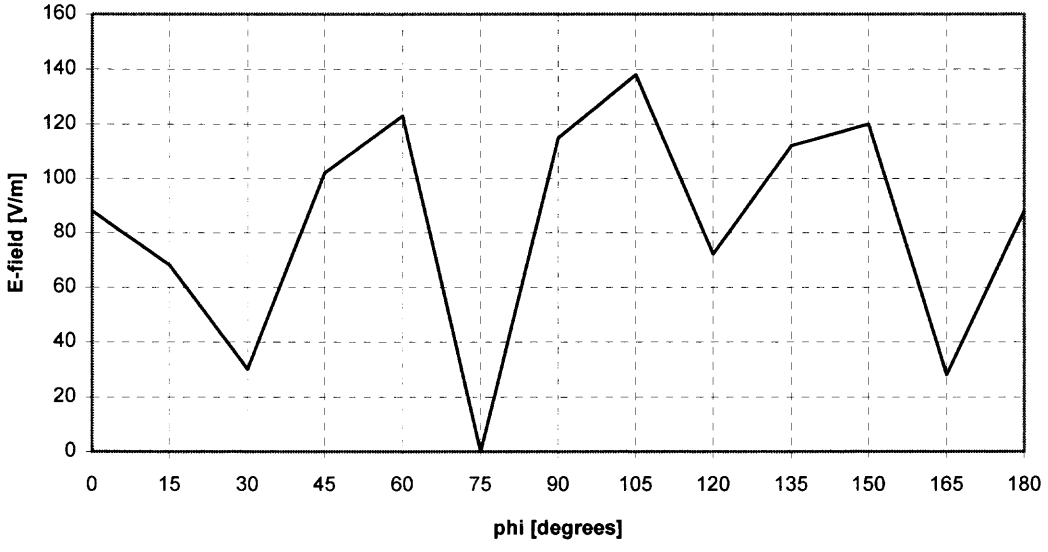

Figure 2.13a E-field magnitude vs. ϕ, d_{sphere} = 31 mm, f = 5 GHz, n = 1.5, 2 layers.

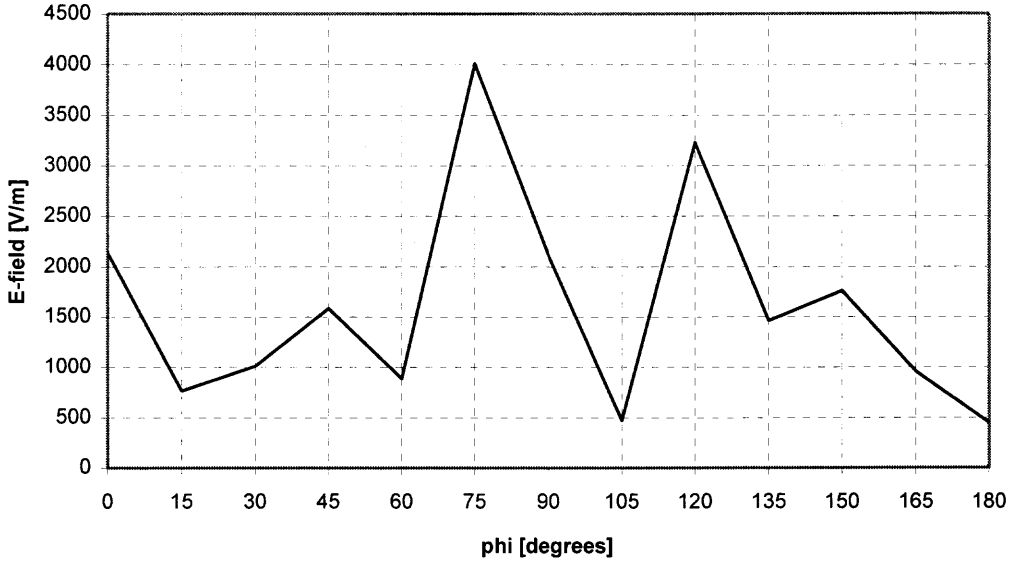

Figure 2.13b E-field magnitude vs. ϕ, d_{sphere} = 31 mm, f = 10 GHz, n = 1.5, 2 layers.

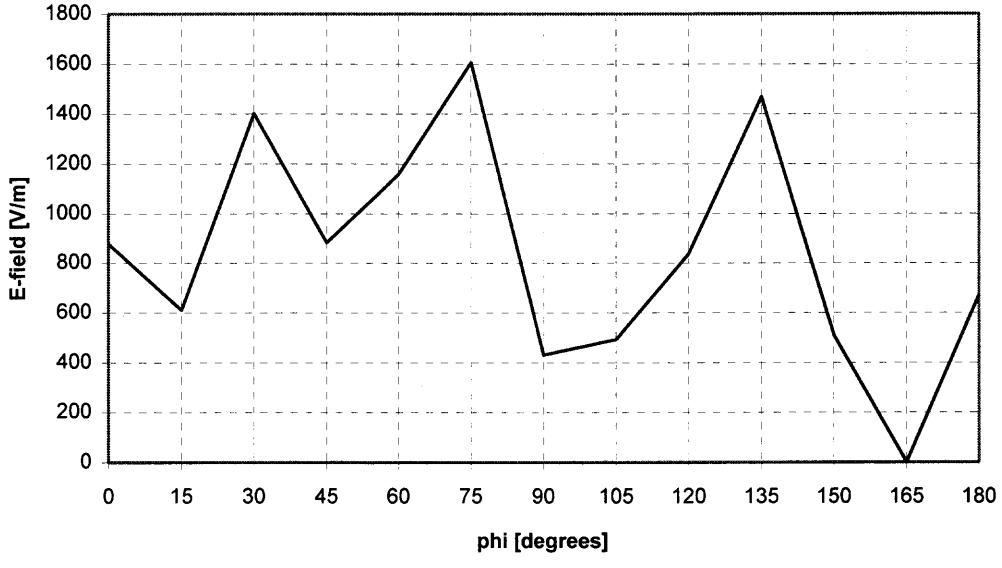

Figure 2.13c E-field magnitude vs. ϕ, d_{sphere} = 31 mm, f = 15 GHz, n = 1.5, 2 layers.

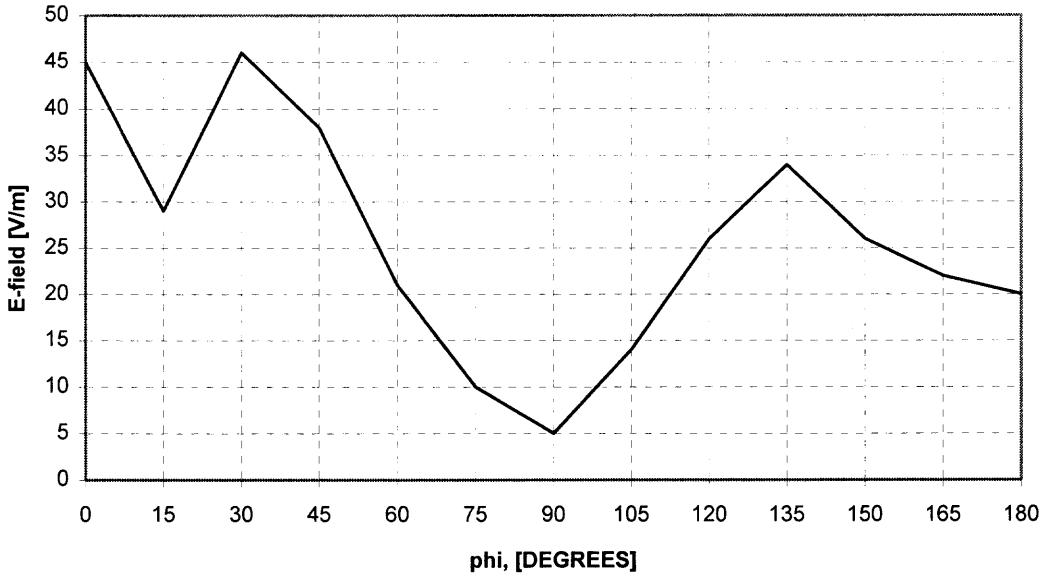

Figure 2.14a E-field magnitude with respect to ϕ, d_{sphere} = 31 mm, n = 1.5, f = 5 GHz, 4 layers.

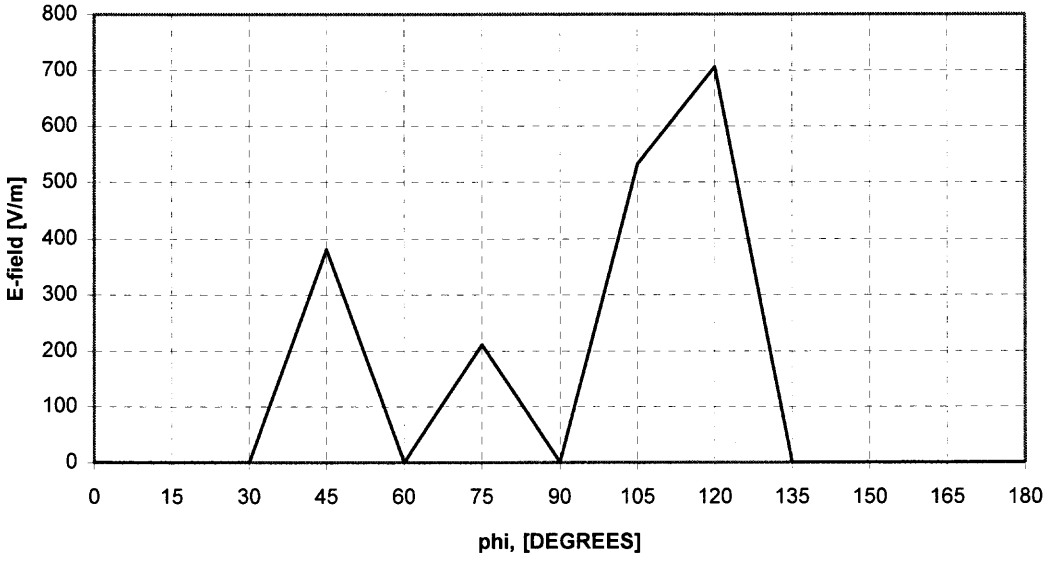

Figure 2.14b E-field magnitude with respect to ϕ, d_{sphere} = 31 mm, n = 1.5, f = 10 GHz, 4 layers.

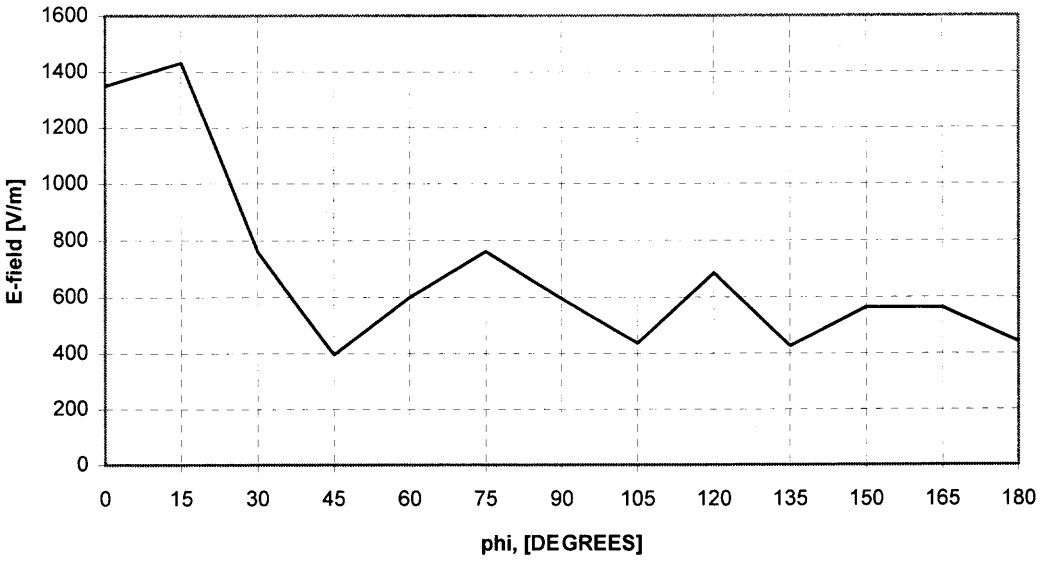

Figure 2.14c E-field magnitude with respect to ϕ, d_{sphere} = 31 mm, n = 1.5, f = 15 GHz, 4 layers.

The last three plots in the series (Figure 2.14a-c) are results for simulation of d_{sphere} = 31 mm structures 4 layers thick. Curiously, the periodic behavior of the 5 GHz, 2-layer result (30° – 45°) disappears and is replaced with what appears to be a 90° periodicity, with the stronger stop band (minima) at 90°. Isolated pass bands at 45°, 75° and 120° are reinforced at the 4-layer 10 GHz result, with the remaining angles at zero transmission. Arguably, scattering may dominate since $\lambda/\Lambda \sim 1$. The simulation result for d_{sphere} = 31 mm, f = 15 GHz is unique in that it is the only case where the media cease to be subwavelength features. Here there is a periodicity within the 45° - 60° range.

2.5.5 Analysis of Results d = 31 mm, n = 1.5, Two and Four Layers

If any periodicity occurs, it seems to have an interval of ϕ = 45° with one case of ϕ = 90° appearing in the 5 GHz case as the layers increase from two to four. At face value, there seems otherwise to be general consistency with the d_{sphere} = 10 mm results. Weakest case

for periodic behavior with respect to ϕ seems to be $\lambda/\Lambda \sim 1$, where scattering is expected. Periodic behavior with respect to ϕ is also observed in the single case where $\lambda/\Lambda < 1$.

2.6 Overall Assessment of Simulation Results

Conduct of the simulation met with limited success. Imaging phenomena was predicted, not only in accordance with classical (Rayleigh) expectation but also subwavelength imaging where $\lambda/\Lambda > 1$ in the fcc crystal system.

It was determined that variation of the transmission properties may exist with respect to the azimuthal orientation of the fcc crystal structure. The azimuthal periodicity appears to have a 45° rotational symmetry, which is correlated to the <100> and <110> crystal directions. Note that the close packed fcc crystal has a rotational 60° symmetry.

Overall, several novel facts were gained from this simulation series:

1) For small crystals (total cross-section on the order of a few wavelengths), transmissivity with respect to the azimuthal orientation of the crystal does not appear to depend on crystal rotational symmetry.

2) Current simulations do not accurately account for the polarization state of the transmitted beam in these cases.

3) Increase of crystal thickness changes the propagation qualities as a function of azimuthal angle. In the case of d_{sphere} = 31 mm, f = 5 GHz, the observed periodicity changed from $\phi = 45°$ to $\phi = 90°$, as the number of layers increased from 2 to 4. This implies that new stop or pass bands were created at different ϕ, which was not previously observed.

Simulations are somewhat limited, as was pointed out, thus the next step in characterizing fcc crystal systems as photonic crystal or optical components is to resort to an experimental campaign.

CHAPTER 3

EXPERIMENTAL EXAMINATION OF PROPAGATION IN ARTIFICIAL OPAL FCC STRUCTURE

3.1 Introduction

A series of experiments to determine the nature of the beam propagation in the crystal media was devised[37]. Close control of the crystal structure is required. For this reason the series of experiments were performed in the microwave regime. Free-space wavelengths range between 20 and 60 millimeters. Therefore the feature size of the spheres is macroscopic and can be easily manipulated into near-perfect crystal forms. In contrast, construction of artificial opaline structures on the order of optical wavelengths is much more difficult and less precise. It is difficult to control or determine the number of layers in an optical artificial opaline structure as well as the presence of an increased rate of defects. For the determination of the self-imaging distance, a crystal somewhat devoid of defects is important, since defect modes can make a significant difference in radiation transmission in the crystal.

3.2 Experimental Setup

Transmitted power in the y-z plane was measured for each successive layer of dielectric media at the crystal face. A continuous wave signal source (Hewlett-Packard 8673E signal generator) was fed through a standard gain horn (MicroTech HWR112) on the transmit side. To acquire the signal, spectrum analyzer (Hewlett-Packard 8563E) was used with an identical standard gain horn antenna. The second standard gain horn can be

moved in the y-z plane for each media layer to measure the power distribution over the y-z surface (Figure 3.1). In this fashion, field maps for each crystal plane was constructed. The resolution of the field map was limited by the physical size of the gain horn, however. For a typical structure, a field map is comprised of nine rectangular sectors on the crystal face and a center value measurement. For determination of the self-imaging distance, the transmitted power at y = z = 0 is of primary interest anyway. The spot size could not be acquired with any reasonable accuracy due to this limitation.

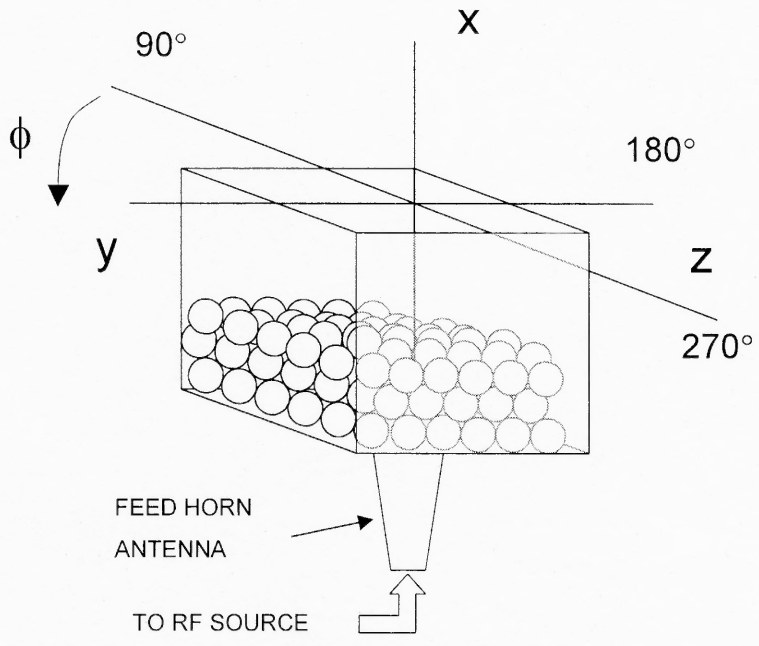

Figure 3.1 Configuration of experimental setup for field mapping at the crystal face. The antenna for signal acquisition is (omitted here) was moved in the y-z plane to map the transmitted signal at the crystal face.

Dielectric spheres were stacked in a microwave-transparent box to achieve the opaline structure illustrated in Figure 3.1. Although optical opaline has a face-centered cubic (fcc) structure, realization of other crystal structures such as simple cubic, body-centered cubic (bcc) and hexagonal close-packed (hcp) were possible (in fact, hcp and fcc are indistinguishable for the first two layers of media). For this series of experiments,

two media sizes were used, 10 mm and 31 mm with an index of refraction n_{sphere} = 1.5, 2.25 and 2.5 for the 10 mm spheres and n_{sphere} = 1.5 for the 31 mm media. All values of n are determined in the 5 - 18 GHz frequency range.

3.3 Experimental Results

3.3.1 Contrast Variation - Comparison of Ls for n_{sphere} = 1.5, 2.25 and 2.5

Figures 3.2 through 3.4 detail the results of the experiment for media with n_{sphere} = 1.5, 2.25 and 2.5. Note that the measurements are not normalized and that different frequency ranges are encountered due to varied efficiencies over the rated range of the standard gain horn antennas. Recall that the effective refractive index[35, 37] is:

$$(n_{eff})^2=F(n_{01})^2+(1-F)(n_{02})^2 \quad (3.1)$$

Here n_{01}, n_{02} are the refractive indices of the corresponding silica or polypropylene spheres and air, respectively. The filling factor is F = 0.74, for an fcc close-packed structure and may be smaller for a loosely packed structure. It was determined that n_{eff} = 1.37 for the polypropylene close-packed experimental configuration of n_{sphere} = 1.5 with an approximate F = 0.70. Similarly, the silica structure n_{eff} = 2.16 and for ceramic n_{eff} = 1.96. The relationship between the pitch and the sphere's diameter is Λ = 0.816d for a close-packed structure. The experimental structure closely replicates this and was quite defect-free, with some exception at the structure edges.

Strong imaging is noted at low frequencies, evidenced by the recurring peaks at 5 GHz for all media. As the frequency is progressively increased, the differences between minima and maxima decreased.

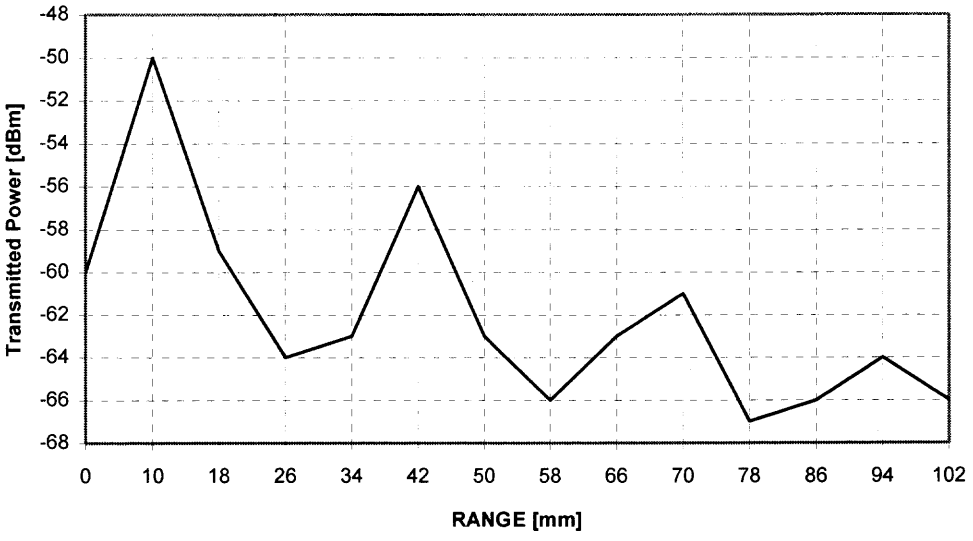

Figure 3.2a Power versus range in media, polypropylene spheres, n_{sphere} = 1.5, f = 5 GHz, 0 – 13 layers of fcc crystal.

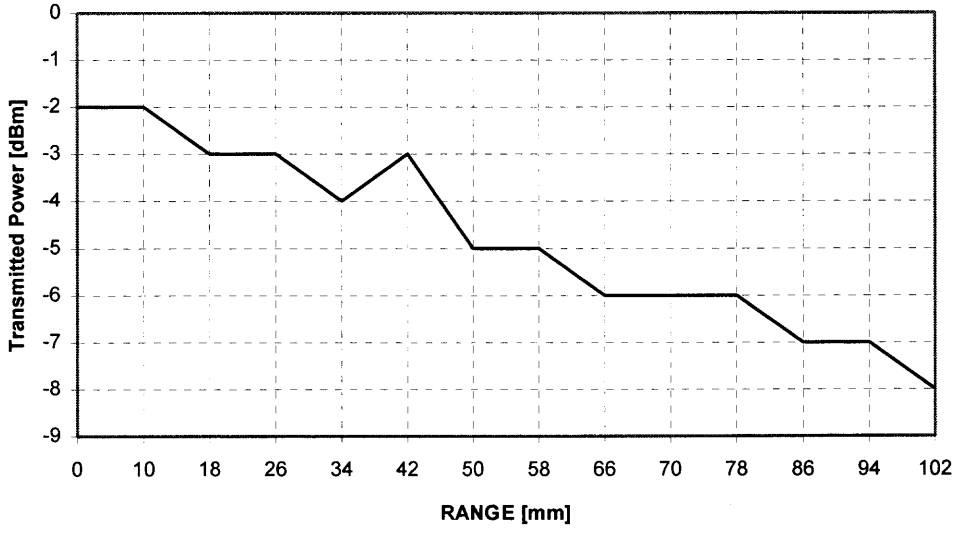

Figure 3.2b Power versus range in media, polypropylene spheres, n_{sphere} = 1.5, f = 10 GHz, 0 – 13 layers of fcc crystal.

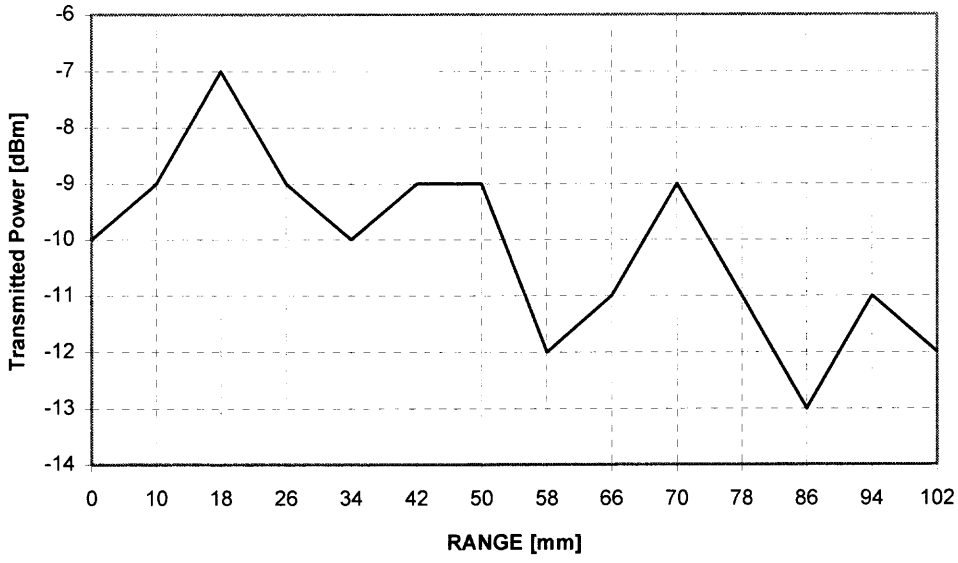

Figure 3.2c Power versus range in media, polypropylene spheres, $n_{sphere} = 1.5$, f = 12 GHz, 0 – 13 layers of fcc crystal.

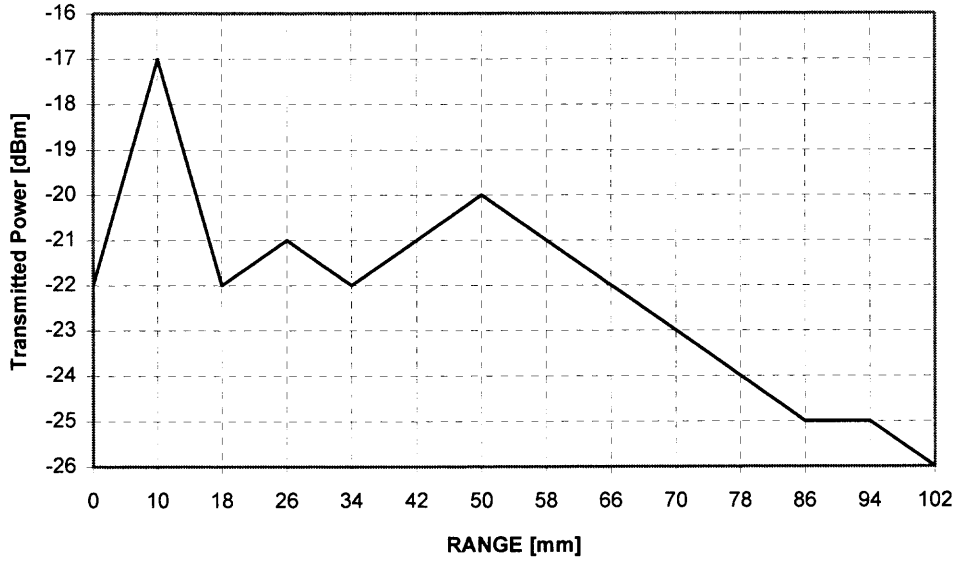

Figure 3.2d Power versus range in media, polypropylene spheres, $n_{sphere} = 1.5$, f = 15 GHz, 0 – 13 layers of fcc crystal.

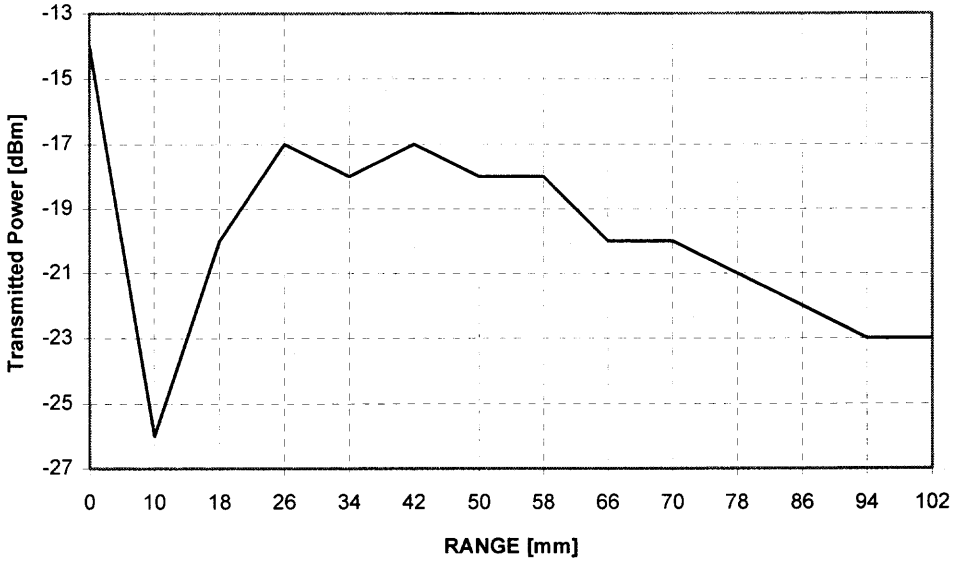

Figure 3.2e Power versus range in media, polypropylene spheres, $n_{sphere} = 1.5$, f = 17 GHz, 0 – 13 layers of fcc crystal.

For example, the polypropylene media ($n_{sohere} = 1.5$, $n_{eff} = 1.37$) at 10 GHz (Figure 3.2b) shows an excursion of less than 1 dBm, after accounting for the downward trend of the power with increasing media layers. It is expected that this loss is due to scattering since it appears as linear with the crystal layers and the media is purely dielectric. Recent simulation work (with two-dimensional structures) also predicts significant out-of-plane scattering, which occurs mostly within the first ten periods in a photonic crystal structure[38]. This scattering loss in the polypropylene is similar for any frequency, a peak-to-peak loss of approximately 4 - 6 dBm in the first 40 mm or so of media. At the lower frequencies, an important feature was noticed. The self-imaging distance is on the order of, or less than the wavelength of the radiation in the media[37]. The results for 5 GHz are in Table 3.1. In fact, the classical picture of the self-imaging distance does not hold, since the wavelength is larger than the crystallographic pitch Λ.

For example, the inverse trend of the self-imaging distance with respect to increasing n is opposite to what one might expect from the classical result (Equation 1.7).

Table 3.1 5 GHz results for contrast variation

Material	f [GHz]	n_{eff}	Average Ls [mm] (1)	λ_n [mm]
Polypropylene	5	1.37	29.3	43.8
Ceramic	5	1.96	19.2	30.6
Silica	5	2.16	18.0	27.1
NOTES: 1) Ls measurements are +/- 4 mm – closer tolerance is not possible since only integral multiples of crystal layers are used.				

3.3.2 Frequency Variation

Examination of the experimental results clearly indicates that strong self-imaging occurs at longer wavelengths (lower frequencies). The worst case of imaging at 5 GHz is the ceramic media result. This may result from the comparatively non-uniform ceramic media. Compared to the high quality polypropylene media, the manufacture of the ceramic media was not to the same tolerances. Generally, the imaging can be correlated to the value of λ/Λ. In the $n_{sphere} = 1.5$ case ($n_{eff} = 1.37$), strong imaging was observed at f = 5 GHz and f = 12 GHz. At f = 10 GHz, a series of small maxima were detected at a period of 16 – 24 mm. For the most part, the magnitudes at 10 GHz are only on the order of 1/3 dBm, which is close to the resolution limit of the acquisition equipment. At 12 GHz, however, strong imaging returns where $\lambda_{neff}/\Lambda \sim 2.2$. As $\lambda_{neff}/\Lambda < 1$, the period of the self imaging range becomes indeterminate and even somewhat erratic.

In the silica ($n_{sphere} = 2.5$) spheres, the weakening of the imaging effect is noticeable yet maxima are somewhat distinct through 15 GHz. At higher frequencies,

smaller peaks are encountered while the overall power loss becomes greater most likely due to scattering of energy out of the crystal structure or perhaps 15 GHz approaches the photonic band gap of this fcc structure, frustrating transmission through the crystal. An important observation from Table 3.2 is that as the λ_{neff}/Λ ratio becomes smaller, the inverse proportionality between wavelength and the self-imaging distance holds true.

Table 3.2 Effect of frequency variation on self-imaging distance, n = 2.5

f [GHz]	λ [mm]	λ/Λ	λ_{neff} [mm]	λ_{neff}/Λ	Average Ls [mm] (1)	Remarks
5	60.00	7.35	27.80	3.41	18.0	Loss: 9 dBm
10	30.00	3.68	13.90	1.70	not evident	Loss: 7 dBm
12	25.00	3.06	11.60	1.42	32.0	Loss: 9 dBm
15	20.00	2.45	9.30	1.13	36.1	Loss: 24 dBm
18	16.67	2.04	7.72	0.94	40.0	Loss: 58 dBm
NOTES: 1) Ls measurements are between maxima exceeding 2 dBm from a straight-line extrapolation of the loss.						

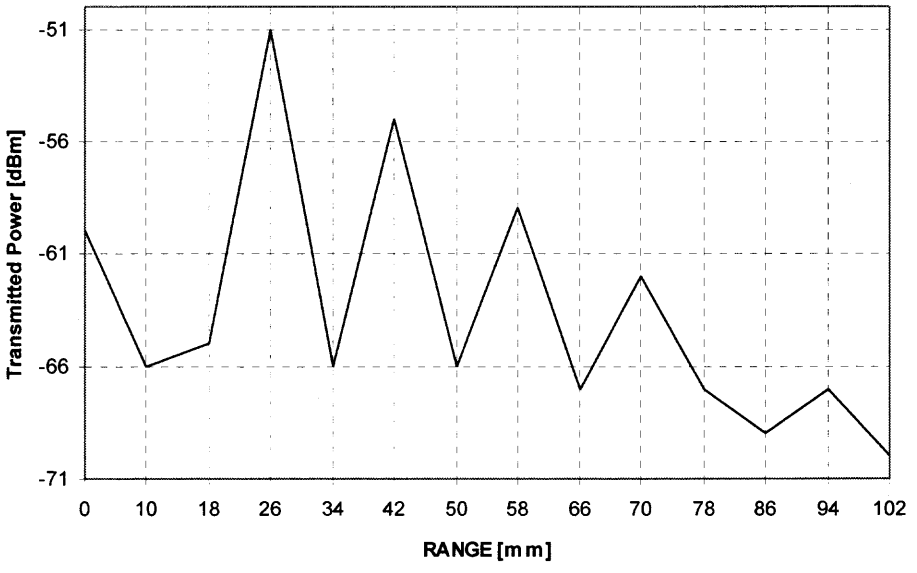

Figure 3.3a Power versus range in media, silica spheres, n_{sphere} = 2.5, f = 5 GHz, d_{sphere} = 10 mm, 0 – 13 layers of fcc crystal.

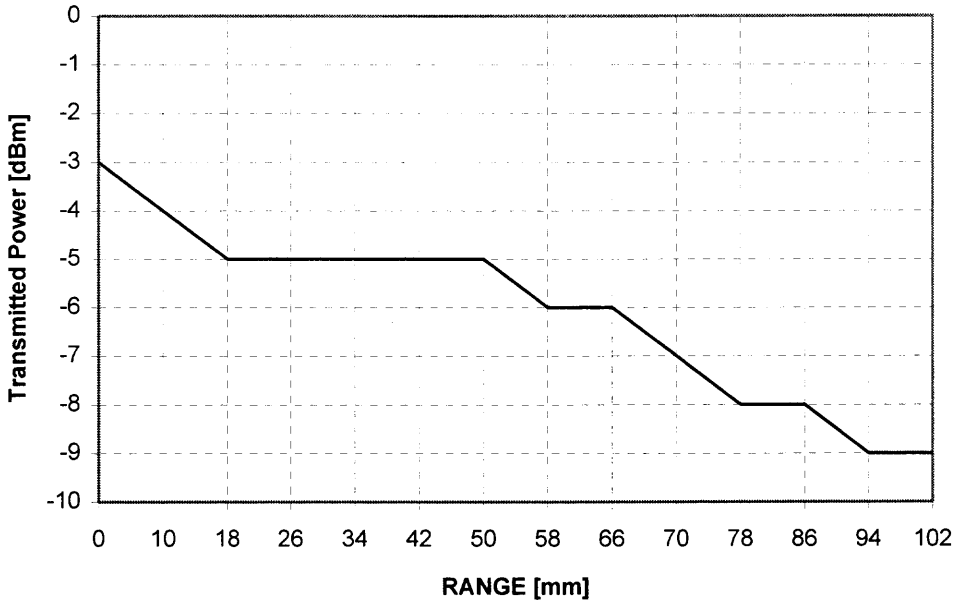

Figure 3.3b Power versus range in media, silica spheres, $n_{sphere} = 2.5$, f = 10 GHz, $d_{sphere} = 10$ mm, 0 – 13 layers of fcc crystal.

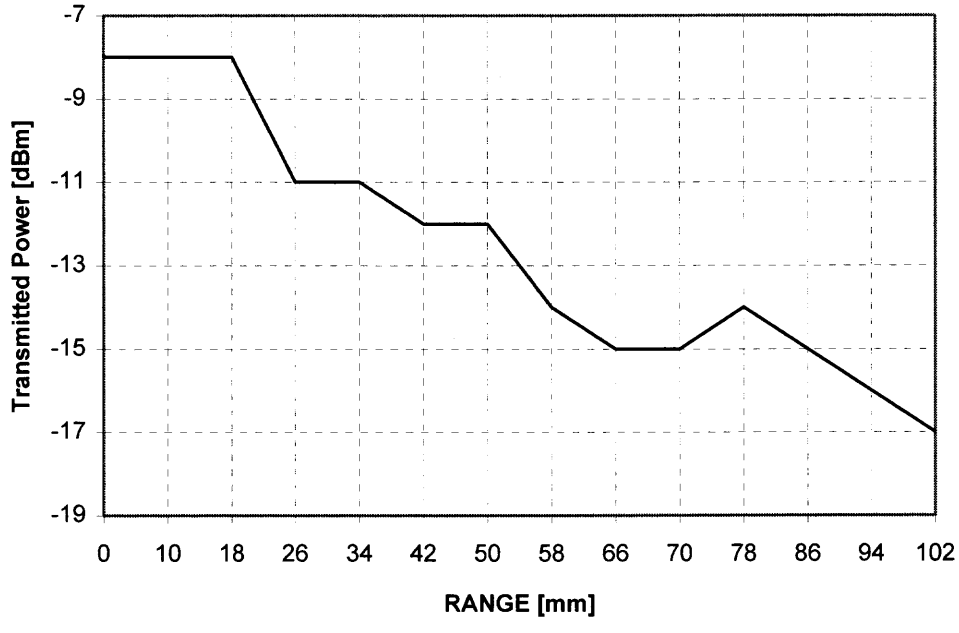

Figure 3.3c Power versus range in media, silica spheres, $n_{sphere} = 2.5$, f = 12 GHz, $d_{sphere} = 10$ mm, 0 – 13 layers of fcc crystal.

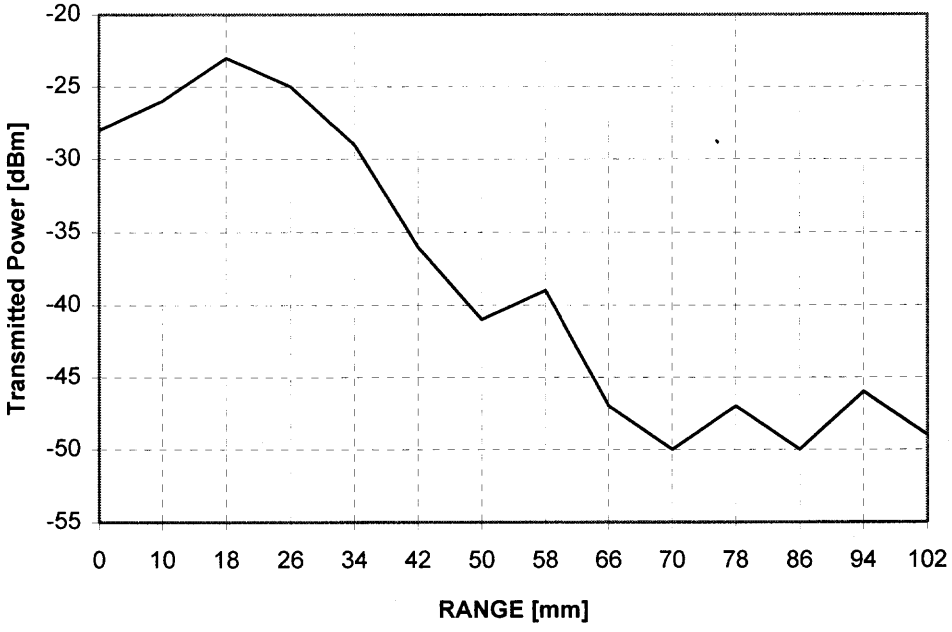

Figure 3.3d Power versus range in media, silica spheres, n_{sphere} = 2.5, f = 15 GHz, d_{sphere} = 10 mm, 0 – 13 layers of fcc crystal.

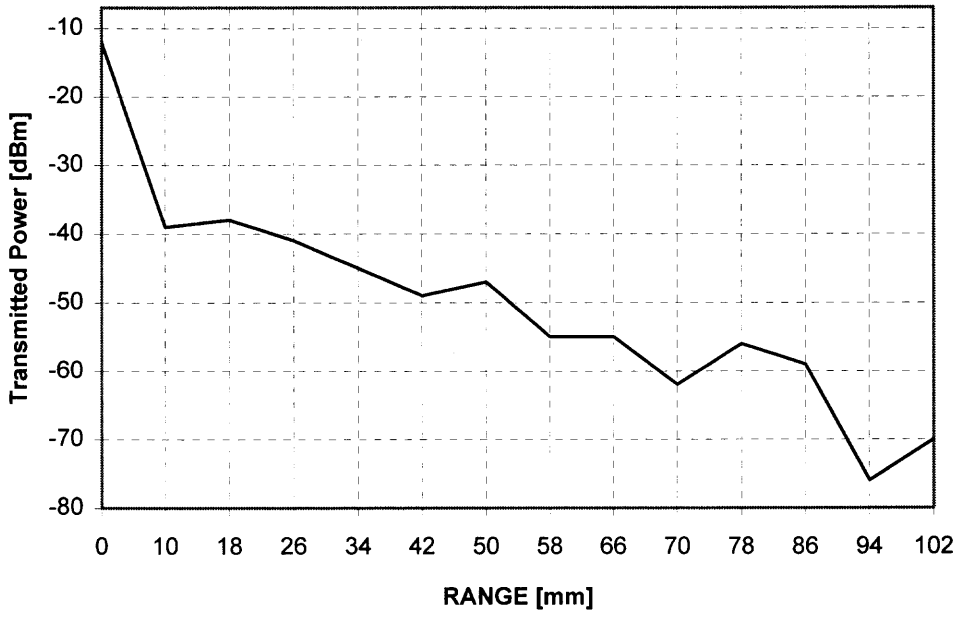

Figure 3.3e Power versus range in media, silica spheres, n_{sphere} = 2.5, f = 18 GHz, d_{sphere} = 10 mm, 0 – 13 layers of fcc crystal.

3.4 Variation of Period, comparison of d_{sphere} = 10 mm and 31 mm

To compare the experimental result to the classical relationship, the experiment was repeated with an fcc crystal comprised of polypropylene (n_{sphere} = 1.5) spheres of d = 31 mm. Figure 3.5a-e illustrates the results. The n_{sphere} = 1.5 and n_{eff} = 1.37, since the filling fraction is identical to the d = 10 mm experiment. Note that there is no strong recurring maxima until f = 15 GHz although at f = 10 and 12 GHz, maxima are beginning to form. At f = 15 GHz, the ratio of $\lambda_{neff}/\Lambda = 0.58$ with d_{sphere} = 31 mm, therefore, one may think that a comparison to the classical self-imaging relationship given by Rayleigh may be attempted. However, recall the quality factor used in holographic (e.g. self-imaging) waveguides[19]. This is given by:

$$Q = 2\pi\lambda\,(Ls)/(n_{eff}\,d^2) \tag{3.2}$$

where d is the width of the central guiding channel of the waveguide. The quality factor defines if the hologram is thin (Q < 10) or thick (Q > 10). Computing the quality, Q, for the structures with the d_{sphere} = 31 mm structures where the $\lambda_{neff}/\Lambda < 1$ reveals that for 10 and 15 GHz self-images (holograms) remain in the thin regime with Q < 10.

Attempting Rayleigh's computation:

$$z = \frac{\lambda}{1 - \sqrt{\left(1 - \frac{\lambda^2}{\Lambda^2}\right)}} \tag{3.3}$$

where the value for the crystallographic pitch, Λ is substituted for d. Substituting the value of λ_{neff} = 14.6 mm and Λ = 25.2 mm into this equation results in z = 78.9 mm. Examining Figure 3.5e, there is a recurring maxima at a range of z = 74 mm in the first five layers, but then a strong recurring image appears at intervals of 50 mm. (Note that

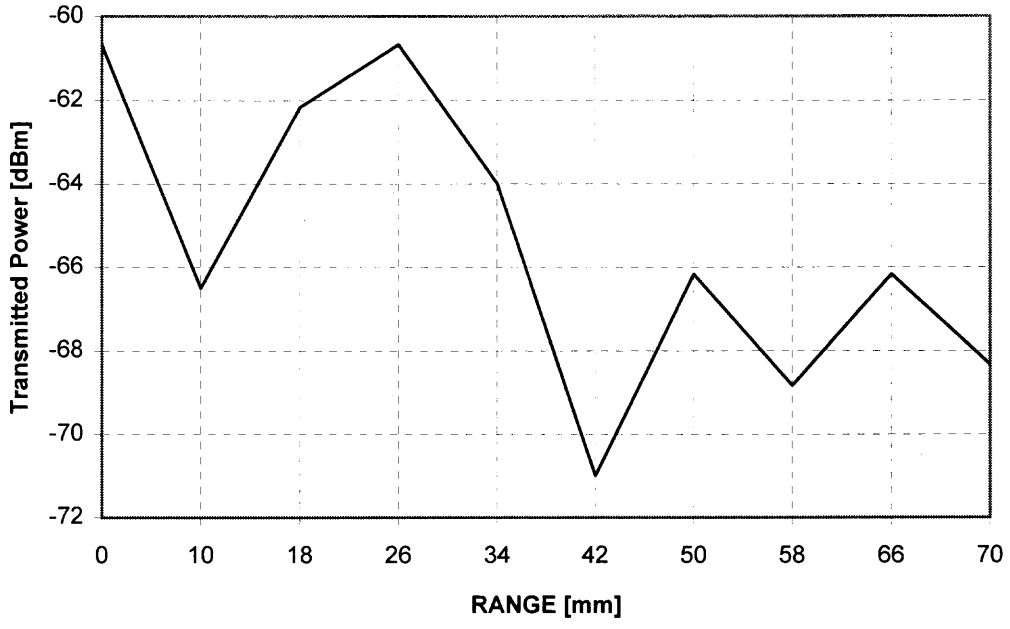

Figure 3.4a Power versus range in media, ceramic spheres, $n_{sphere} = 2.25$, f = 5 GHz, $d_{sphere} = 10$ mm, 0 – 9 layers of fcc crystal.

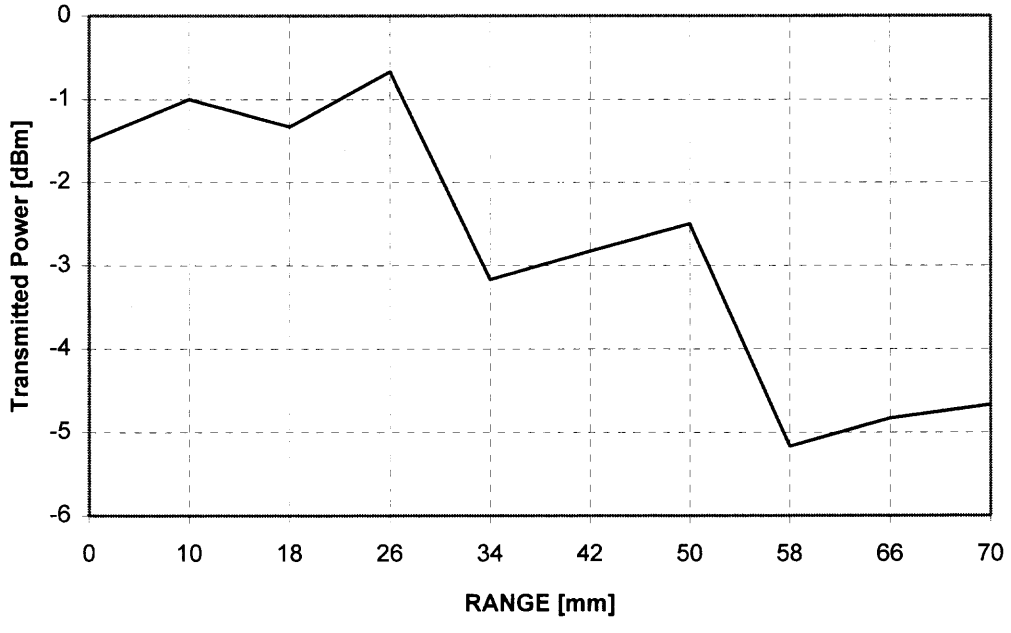

Figure 3.4b Power versus range in media, ceramic spheres, $n_{sphere} = 2.25$, f = 10 GHz, $d_{sphere} = 10$ mm, 0 – 9 layers of fcc crystal.

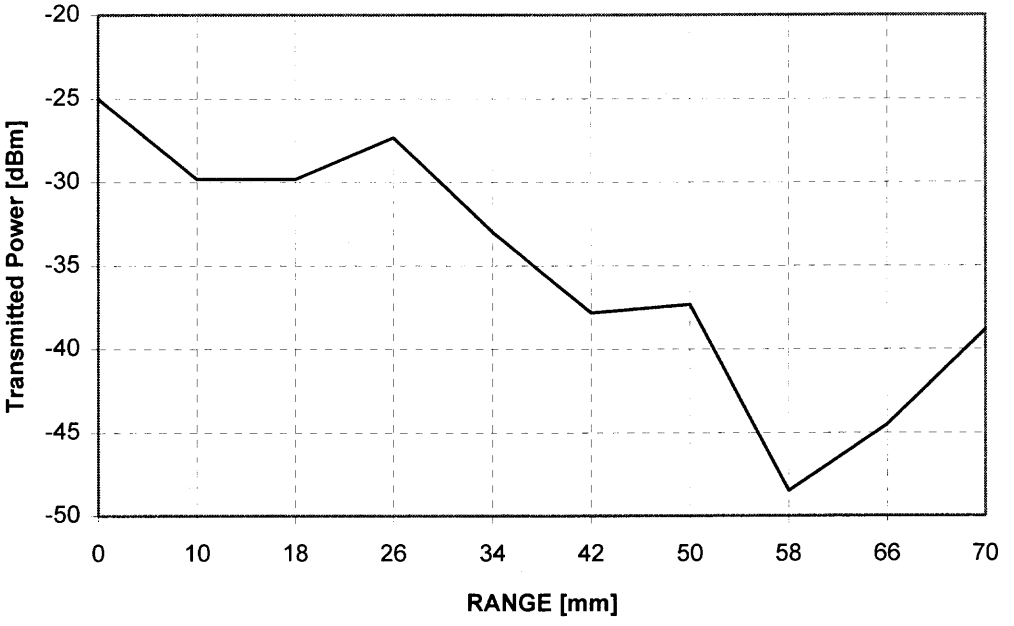

Figure 3.4c Power versus range in media, ceramic spheres, $n_{sphere} = 2.25$, f = 15 GHz, $d_{sphere} = 10$ mm, 0 – 9 layers of fcc crystal.

the first imaging planes are not as strong as that observed in the $d_{sphere} = 10$ mm, f= 5 GHz case.) There is some agreement with the Rayleigh relationship, considering that it is an approximation. Moreover, it is an approximation that becomes less accurate as the value of λ approaches the value of Λ.

Another comparison that can be made is to the Latimer and Crouse relation for the self-imaging distance given by:

$$\frac{1}{R_1} + \frac{1}{R_2} = \frac{1}{nT} \tag{3.3}$$

where the variables are based on the multiple slit diffraction model already discussed. The primary approximation to apply this model to the experiment is that the "diffraction grating" is not a two-dimensional plate, rather, it comprises the ranges from source to

diffraction plane. If the gross approximation to consider the crystal as a "lumped" element is made, and let q = 1 to 5, which can be the maximum number of diffraction orders given the physical size of the crystal using λ_{neff}, the result is $z \approx 100$ mm in the relatively crude approximation, depending on the Bragg diffraction order used. The 100 mm result is interesting since it's an integral multiple of the experimental observation where Ls = 50 mm at greater ranges in the $d_{sphere} = 31$ mm crystal at 15 GHz. Despite its lack of sophistication, the approximation of the Latimer – Crouse self-imaging relationship yields some confidence that the three dimensional photonic crystal may behave within the predictions of diffraction theory as $\lambda << \Lambda$. Attempting extension of Latimer-Crouse self-imaging relationships to three-dimensional systems may have some merit. More sophisticated techniques are needed as $\lambda > \Lambda$, however.

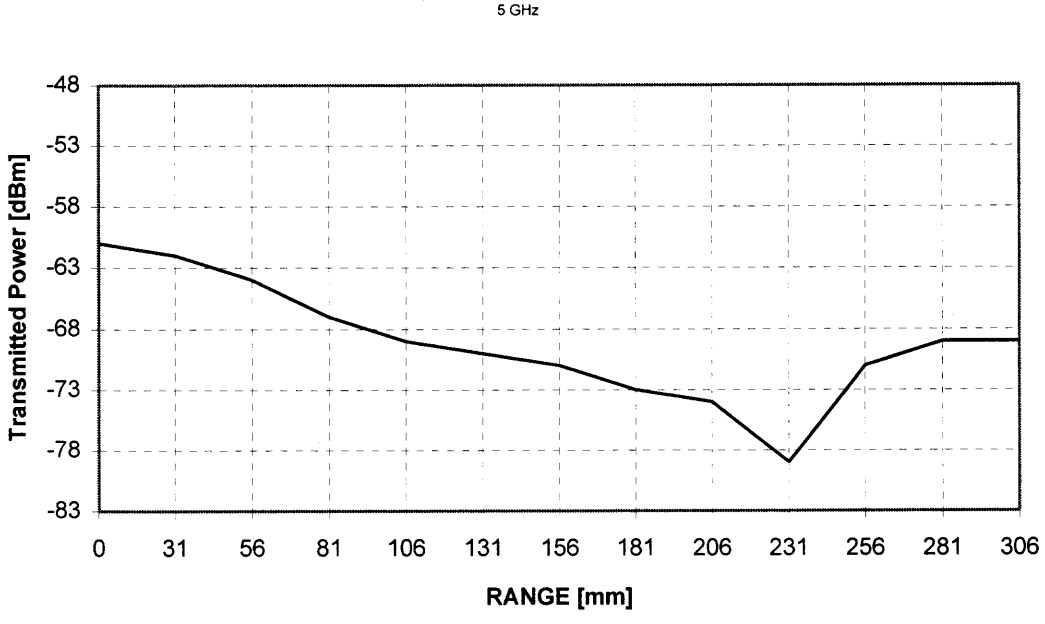

Figure 3.5a Power vs. range in polypropylene crystal, $d_{sphere} = 31$ mm, f = 5 GHz, $n_{sphere} = 1.5$.

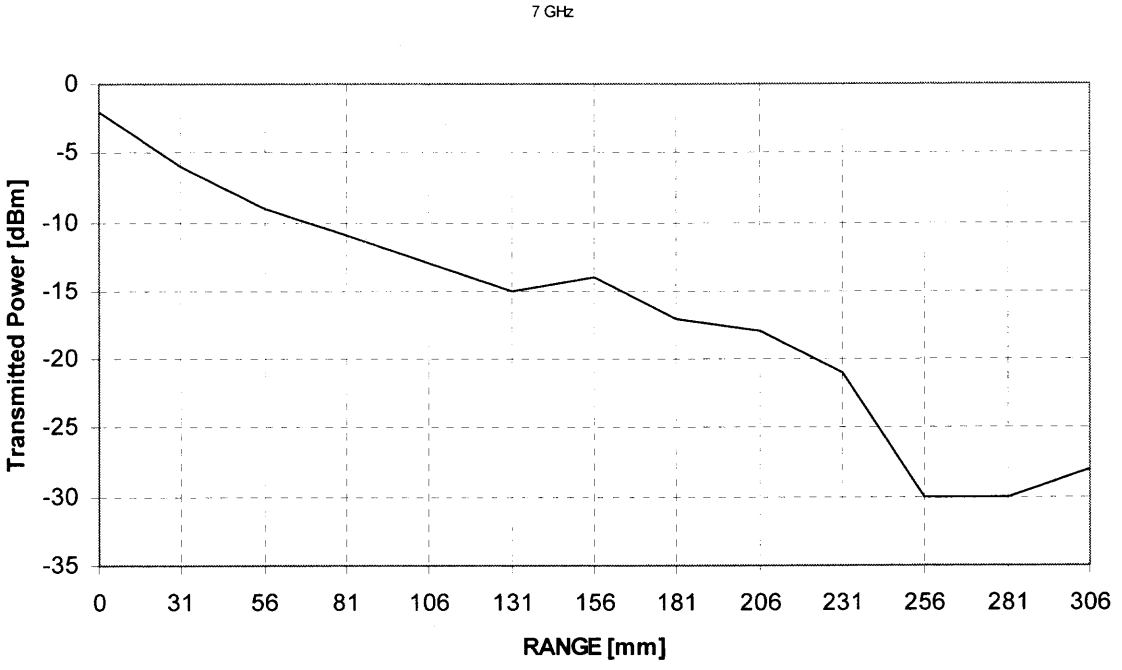

Figure 3.5b Power vs. range in polypropylene crystal, d_{sphere} = 31 mm, f = 7 GHz, n_{sphere} = 1.5.

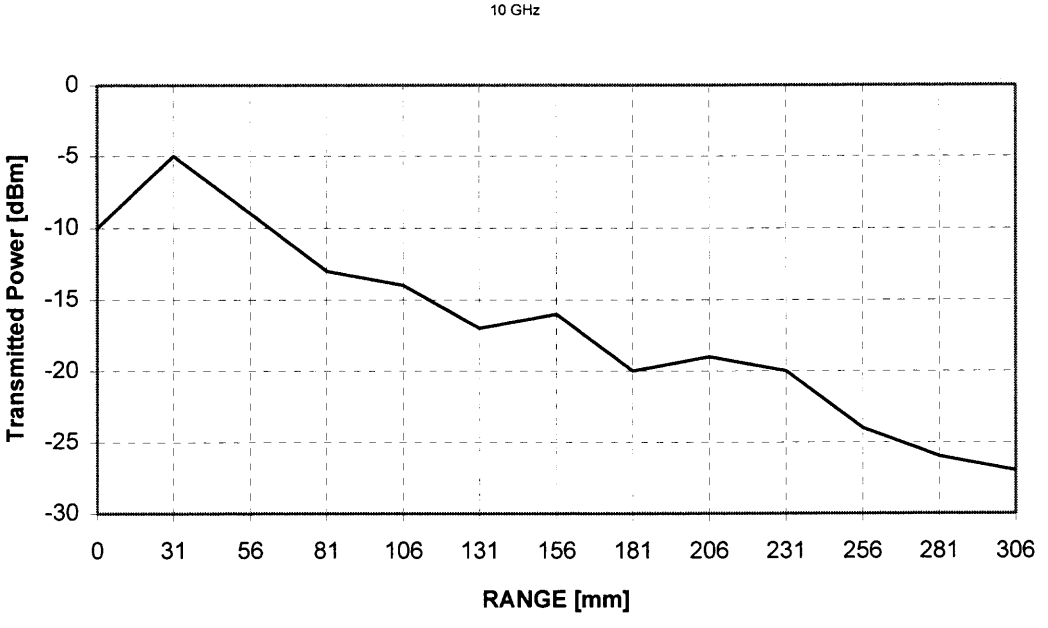

Figure 3.5c Power vs. range in polypropylene crystal, d_{sphere} = 31 mm, f = 10 GHz, n_{sphere} = 1.5.

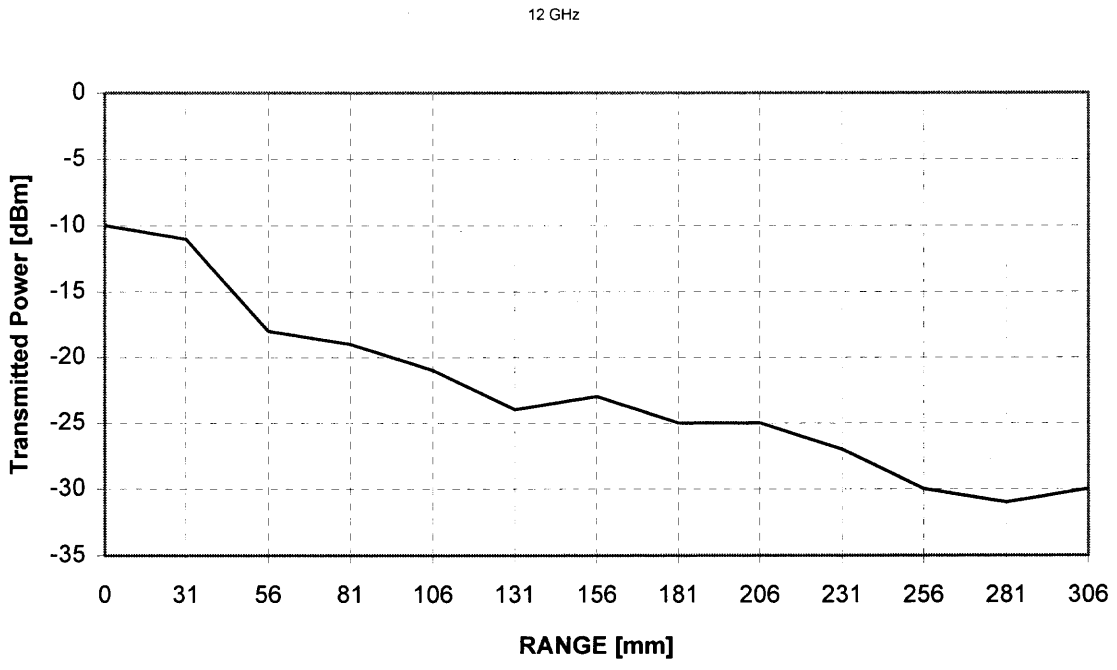

Figure 3.5d Power vs. range in polypropylene crystal, d_{sphere} = 31 mm, f = 12 GHz, n_{sphere} = 1.5.

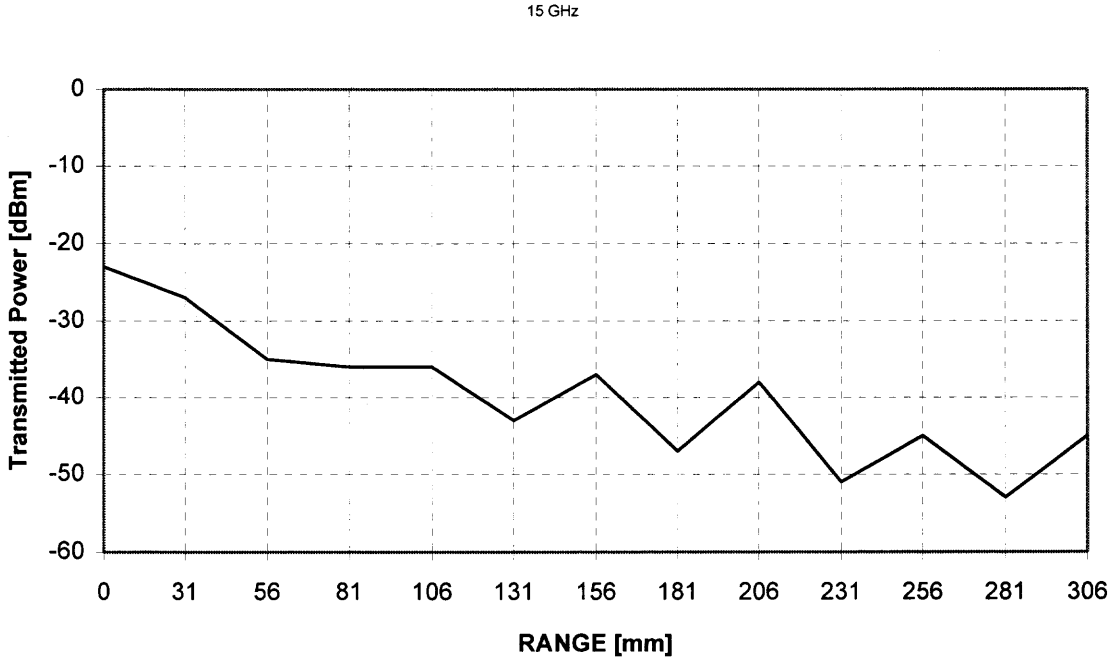

Figure 3.5e Power vs. range in polypropylene crystal, d_{sphere} = 31 mm, f = 15 GHz, n_{sphere} = 1.5.

3.5 Comparison to Simulations

At the outset, a direct comparison to simulation is not possible due to the differences and limitations of the simulated structures, as discussed. However, trends can be compared. In doing so, the cases of large refractive index contrast and small contrast were used. For both experimental data and simulation, Ls (the self-imaging distance) decreases as the refractive index is increased in the case of $\lambda/\Lambda > 1$ (subwavelength media). Self-imaging was most evident in the $\lambda/\Lambda > 1$ region. Increasing the frequency (decreasing wavelength) seemed to generally decrease Ls, as would be expected from the classical theory. Simulation and experiment generally agree on this although Ls is not evident in some of the simulation and experimental trials. Table 3.3 enumerates the self-image formation results for simulation and experiment.

Table 3.3 Simulation and experimental results for self-image formation

f [GHz]	λ [mm]	n_{sphere}	Simulated Ls [mm]	Experimental Ls [mm]
5	60.0	1.5	40	29.3
10	30.0	1.5	30	not evident
15	20.0	1.5	20	42.0
5	60.0	2.5	30	18.0
10	30.0	2.5	40	not evident
15	20.0	2.5	70	36.1

As one can see, the trends are the same but the values do not precisely match. The simulation appears more accurate at lower frequency (5 GHz), since both simulation and experiment show approximately a 10 mm change in the self-image position. At

higher frequency (15 GHz) there is a larger disparity between simulation and experiment. This may be caused by the wavelength size compared to the size of the finite element mesh.

3.6 Experimental Conclusions

Several conclusions can be drawn from these experiments. Subwavelength ($\lambda/\Lambda > 1$) imaging is verified. In addition, short (subwavelength) imaging ranges are observed, where the images form at intervals less than the wavelength of the incident beam.

Contrast variation in the subwavelength ($\lambda/\Lambda > 1$) imaging regime does not behave as one would expect from classical predictions. While there should be a direct proportionality, experimentally the self-imaging distance, Ls, decreases as refractive index, n, increases. Again, this is proven out by experiment and simulation. Some similarity is noted with this case and self-imaging chirped holographic waveguides[19], although in this case there is a periodicity in the direction of propagation and the refractive index contrast is much larger. Evidence suggests also that the direct proportionality between n and Ls may return to the fcc crystal system as $\lambda/\Lambda < 1$.

A possible mechanism for subwavelength imaging and imaging at subwavelength ranges is the phenomena of ultrarefraction (also called superprism), discussed in the review of photonic crystals. To better characterize these effects, other experiments on the three-dimensional fcc photonic crystals were performed.

CHAPTER 4

AZIMUTHAL MORPHOLOGY AFFECTING TRANSMISSION THROUGH FCC CRYSTAL

4.1 Introduction and Experimental Setup

HPHFSS Simulations demonstrate transmission variation with change of the azimuthal orientation of the crystal. The survey of the literature has also revealed that numerical methods suggest ultrarefractive properties are modified by azimuthal orientation as well[33]. Overall, the effect of the azimuthal orientation with respect to beam polarization on wave propagation through the fcc photonic crystal is not well known. Thus, the next experimental series endeavors to characterize the dependency of the azimuthal orientation of the crystal on transmission.

Dielectric spheres of diameter d_{sphere} = 10 mm and d_{sphere} = 31.25 mm with refractive indices of n_{sphere} = 1.5, n_{sphere} = 2.25 and n_{sphere} = 2.5, were stacked in a face centered cubic structure similar to the method described earlier. The crystal was articulated to rotate through an azimuthal angle of ϕ = 0° - 360° with respect to beam polarization at 15° increments. Experiments were repeated for a range of 0° <θ < 25° with the coordinates specified in Figure 4.1. The beam was propagating along the x-direction. The spheres were placed in a box with inner dimensions, y = 135 mm and z = 181 mm with air cladding. Recall the effective refractive index of a close-packed array of spheres is given by $(n_{eff})^2=F(n_{01})^2+(1-F)(n_{02})^2$. Here n_{01}, n_{02} are the refractive indices of the corresponding spheres and air, respectively. Also recall the relationship between the pitch and the sphere's diameter is $\Lambda = 0.816d$ for a closely packed fcc structure.

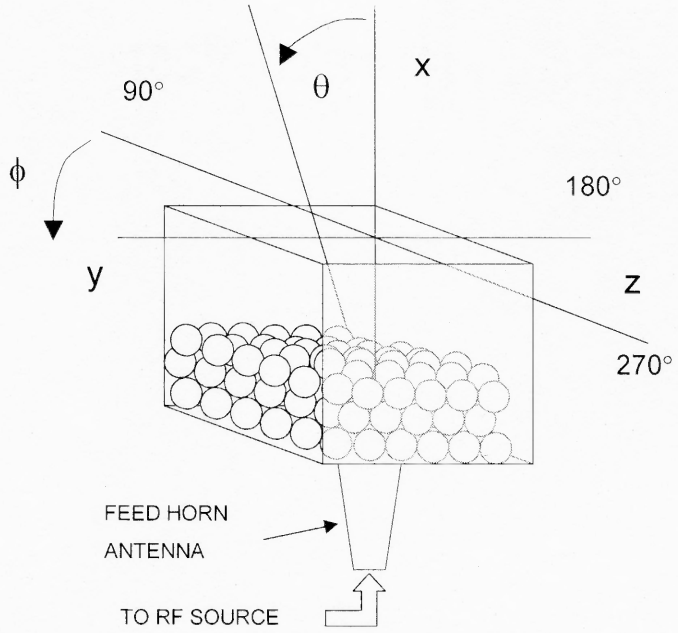

Figure 4.1 Experimental setup for azimuthal angle variation. The crystal is rotated with respect to the y-axis which is the polarization direction for the input beam.

The filling factor is $F = 0.74$, for an fcc close-packed structure and may be smaller for a loosely packed structure sometimes used in the simulations. Values for n_{eff} are presented in the Table 4.1. For the experimental structure used, the fill factor was $F = 0.70$ due to minor irregularities in the crystal.

Table 4.1 Values n_{sphere} and n_{eff}

n_{sphere}	n_{eff}
1.500	1.369
2.250	1.961
2.500	2.162

Measurement of the transmitted energy was performed in the near-field since this would emulate the conditions of the simulation and is the most useful case for coupling of devices in microelectronic applications. Power was measured at x ≈ Ls, the self-

imaging distance, to maximize the radiation collection for signal acquisition. Instrumentation used was a HP 8673E signal generator and a MicroTech HWR112 standard gain horn on the transmit side, as in the previous experiment. To acquire the signal, a HP 8563E spectrum analyzer was used with an identical standard gain horn. A photograph of the structure (polypropylene spheres, d = 10 mm) is at Figure 4.2.

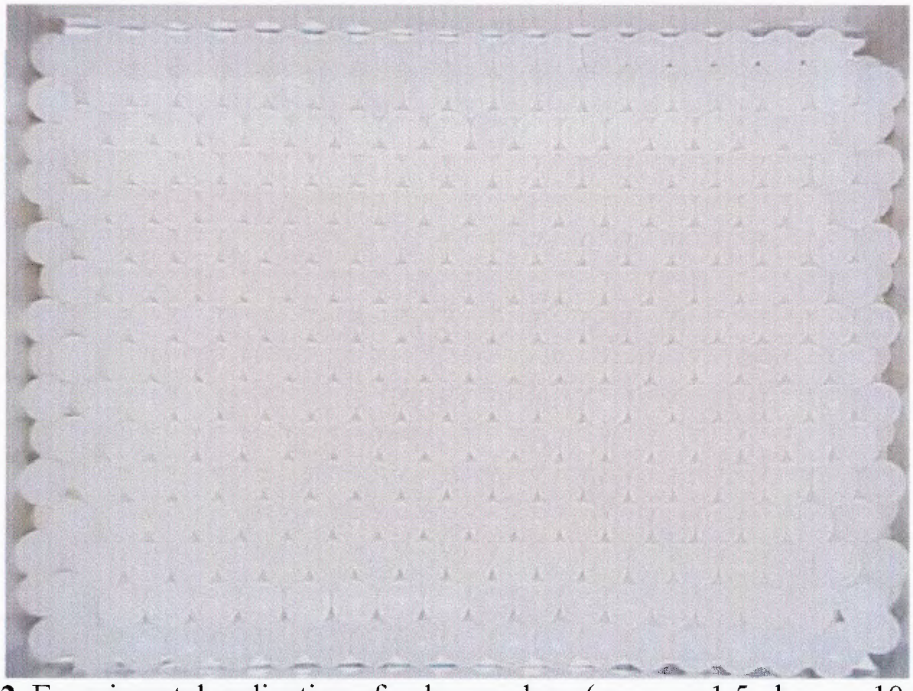

Figure 4.2 Experimental realization of polypropylene (n_{sphere} = 1.5, d_{sphere} = 10 mm) fcc structure. Total dimension of the structure is y = 135 mm and z = 181 mm.

4.2 Experimental Results for Variation of Azimuthal Orientation

Initial trials were performed with two layers of d_{sphere} = 10 mm polypropylene (n_{sphere} = 1.5) media. A very flat response (+/- 0.2 dBm, generally) was noted throughout the range of ϕ. Since the two-layer crystal is very thin compared to the wavelength, the number of layers was increased to four, these results are illustrated in Figure 4.3a-c. Again a flat

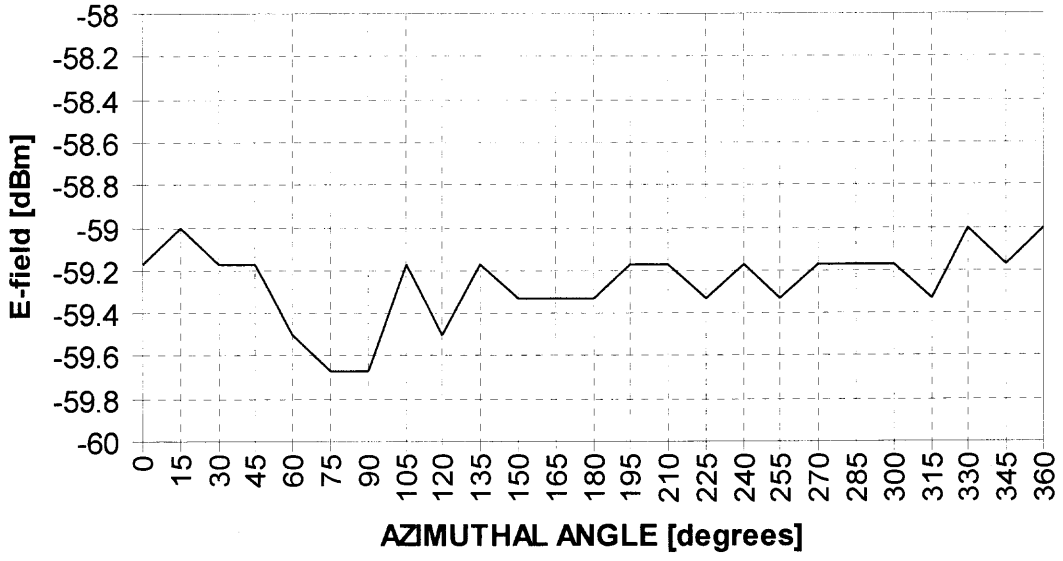

Figure 4.3a Transmitted power variation vs. azimuthal angle, d_{sphere} = 10 mm, n_{sphere} = 1.5, 4 layers, 5 GHz. Note range of the vertical axis is 2 dBm.

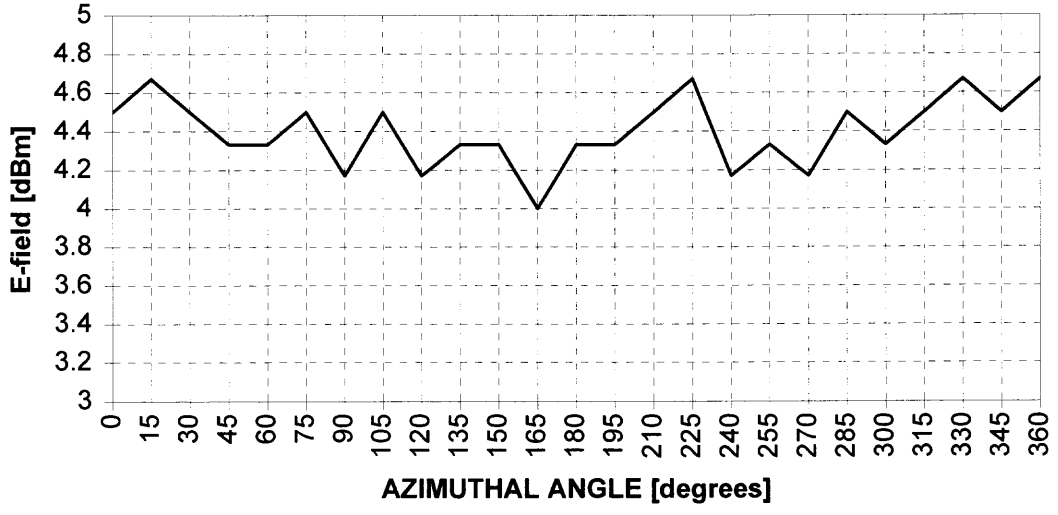

Figure 4.3b Transmitted power variation vs. azimuthal angle, d_{sphere} = 10 mm, n_{sphere} = 1.5, 4 layers, 10 GHz. Note range of the vertical axis is 2 dBm.

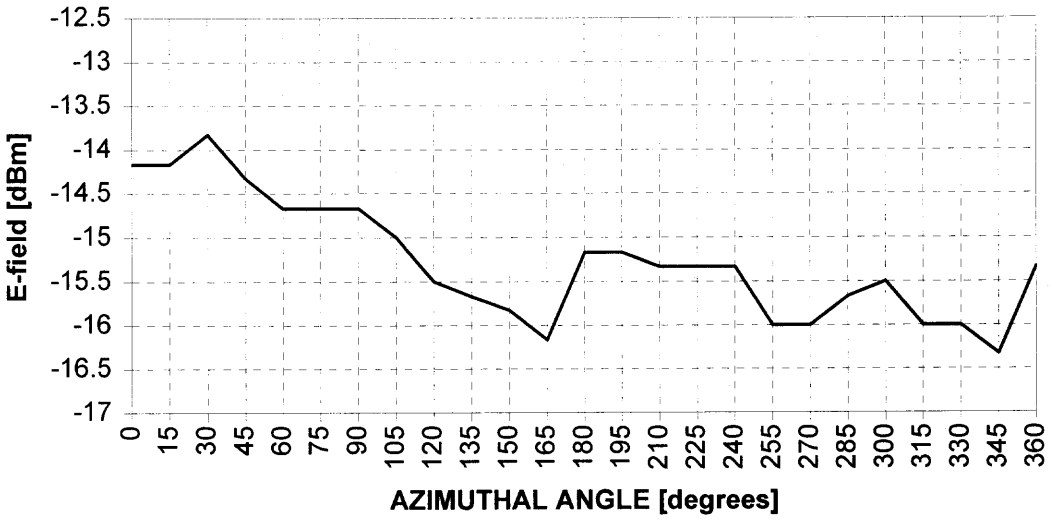

Figure 4.3c Transmitted power variation vs. azimuthal angle, d_{sphere} = 10 mm, n_{sphere} = 1.5, 4 layers, 15 GHz. Note range of the vertical axis is 4.5 dBm.

response is noted for the f = 5 and 10 GHz trials. The resolution of the detection apparatus was 0.17 dBm, therefore it can be concluded that this variation is negligible. Note that at 15 GHz some variation becomes evident, but it is only on the order of 1 dBm. There appears to be little or no periodicity to the transmission pattern at 15 GHz.

It appears from this result that subwavelength features do not affect the transmission as a function of polarization. Note that at 5 GHz, $\lambda_{neff}/\Lambda \approx 5.4$ and at 10 GHz, $\lambda_{neff}/\Lambda \approx 2.7$. However at 15 GHz, $\lambda_{neff}/\Lambda \approx 1.8$ and at this point, more significant transmission variations (approximately 1 dBm) are encountered. In order to investigate this trend, it is necessary to change the scale of the experiment. For the next series of trials d_{sphere} = 31 mm media is used.

4.2.1 Change of Experimental Scale to Vary λ/Λ

Once the scale change is effected, $\lambda_{neff}/\Lambda \approx 1.74$, 0.87 and 0.59 for f = 5, 10 and 15 GHz, respectively. Examining these results (Figure 4.4a-c) at 5 GHz there is a 90° periodicity evident with maxima at 30°, 120° (although truncated), 210° and approximately 300° (actually 315°). As the frequency is increased, further lowering the λ_{neff}/Λ ratio, the maxima do not exhibit a specific periodicity at 10 GHz and then combine at 15 GHz into two maxima centered on approximately 75° and 255°, 180° apart. Note that the power excursion is on the order of 5 dBm, much greater than data at lower frequency.

Recalling the two major lateral directions related to the polarization sensitivity (the <100> and <110> crystal directions) and that they possess periodicities that differ by $\sqrt{2}$, one may assume that azimuthal symmetries may have a period of $\Delta\phi = 45°$. (The series of <100> and <110> crystal directions are 45° and 90° from each other.)

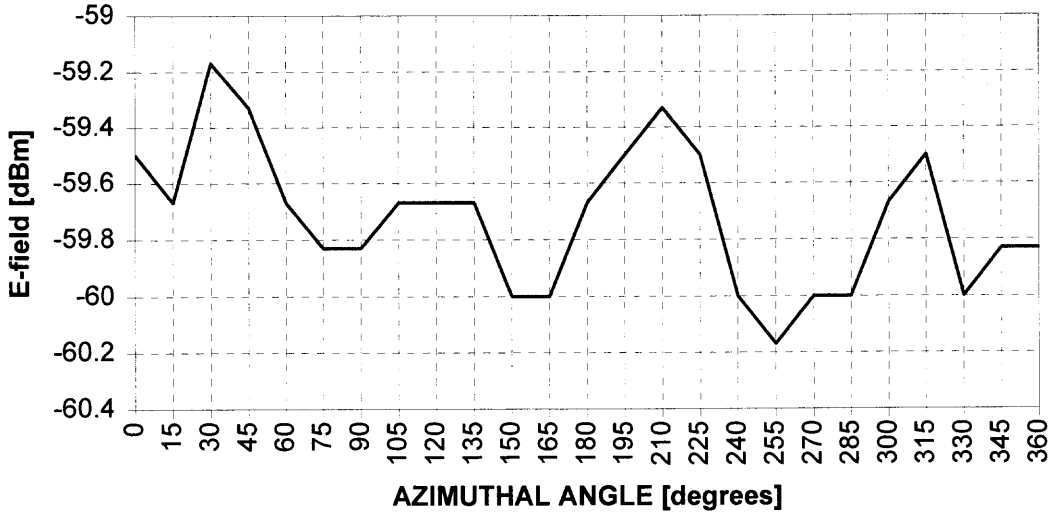

Figure 4.4a Transmitted power variation vs. azimuthal angle, d_{sphere} = 31 mm, n_{sphere} = 1.5, 2 layers, 5 GHz. Note range of the vertical axis is 1.4 dBm.

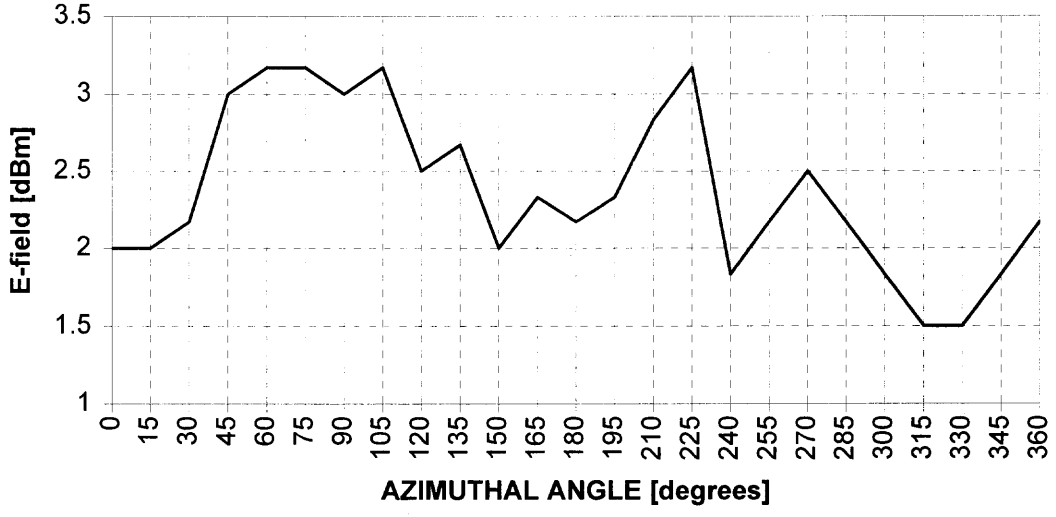

Figure 4.4b Transmitted power variation vs. azimuthal angle, d_{sphere} = 31 mm, n_{sphere} = 1.5, 2 layers, 10 GHz. Note range of vertical axis is 2.5 dBm.

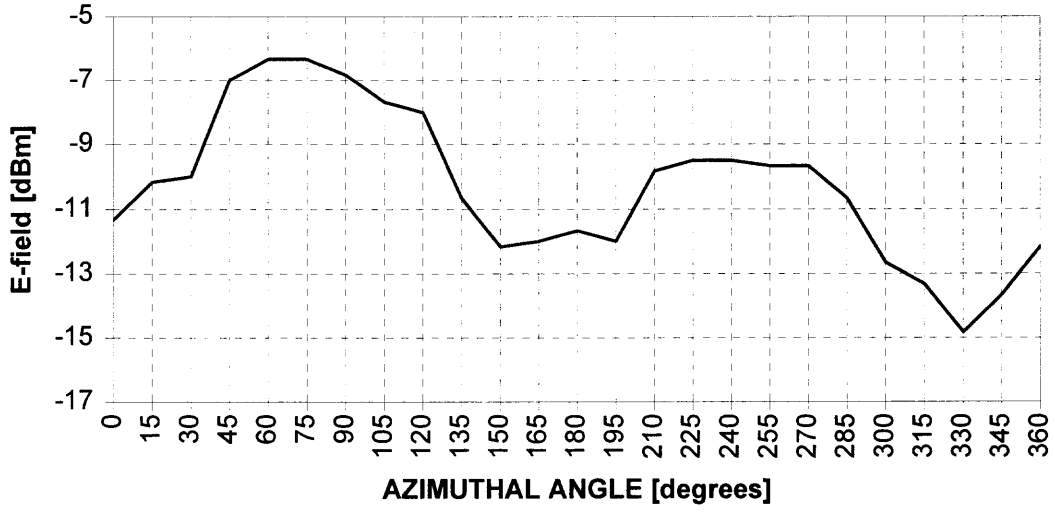

Figure 4.4c Transmitted power variation vs. azimuthal angle, d_{sphere} = 31 mm, n_{sphere} = 1.5, 2 layers, 15 GHz. Note range of the vertical axis is 12 dBm.

Therefore, it is easily expected that periodic transmission variations could occur at some multiple of 45°. Reflection or interference from the crystal "box" is ruled out, since the identical box did not affect the transmission properties of the d_{sphere} = 10 mm trials. Since increasing thickness had the effect of making the transmitted power variations more pronounced on the d_{sphere} = 10 mm trials, the number of layers in this crystal system was increased to four and the experiment repeated. Generally, these effect of increasing the number of layers in the d_{sphere} = 31 mm experiment, illustrated by Figure 4.5a-c, is similar to the d_{sphere} = 10 mm results. At 5 GHz, there are irregular maxima that have an excursion of +/- 1 dBm, however at 10 GHz it is evident that grouping is occurring into two distinct maxima. At 15 GHz, this grouping is complete and the two maxima, centered at approximately 75° to 90° and 240° to 255°, return. Excursion of the transmission is also much greater, on the order of 10 dBm.

4.2.2 Analysis of Variation of Azimuthal Angle

Despite the formation of self-imaging in the fcc crystal system when the media is much smaller than the wavelength, the crystal appears rotationally homogeneous in this region where $\lambda_{neff}/\Lambda > 1$. As λ_{neff}/Λ approaches unity, the transmission begins to exhibit dependence upon the azimuthal angle but no periodicity is yet apparent. At 10 GHz the excursion of the transmitted power is greater for four layers. This is sensible from the viewpoint that scattering may be a dominant mechanism as λ_{neff}/Λ approaches unity.

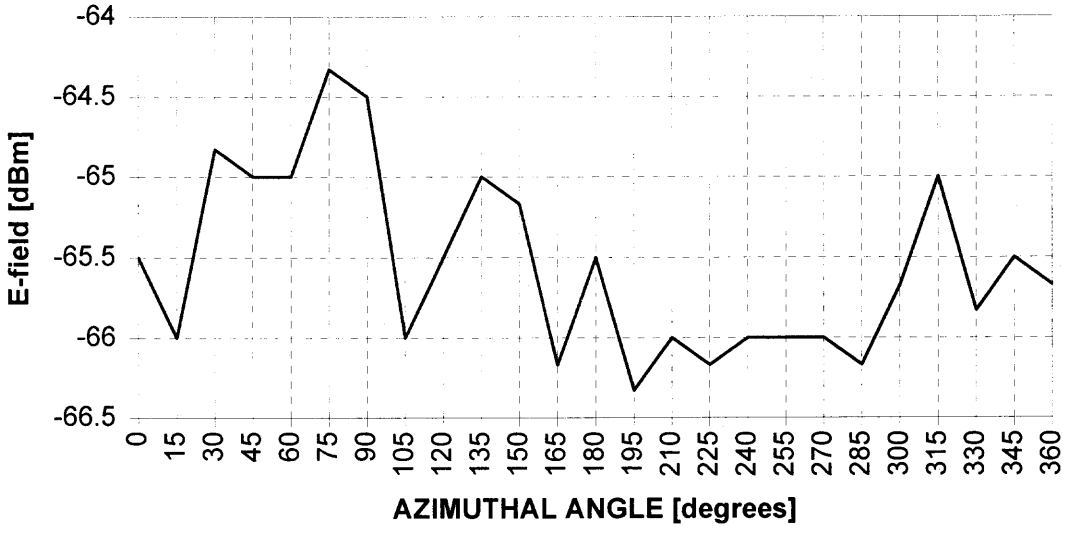

Figure 4.5a Transmitted power variation vs. azimuthal angle, d_{sphere} = 31 mm, n_{sphere} = 1.5, 4 layers, 5 GHz. Note range of the vertical axis is 2.5 dBm.

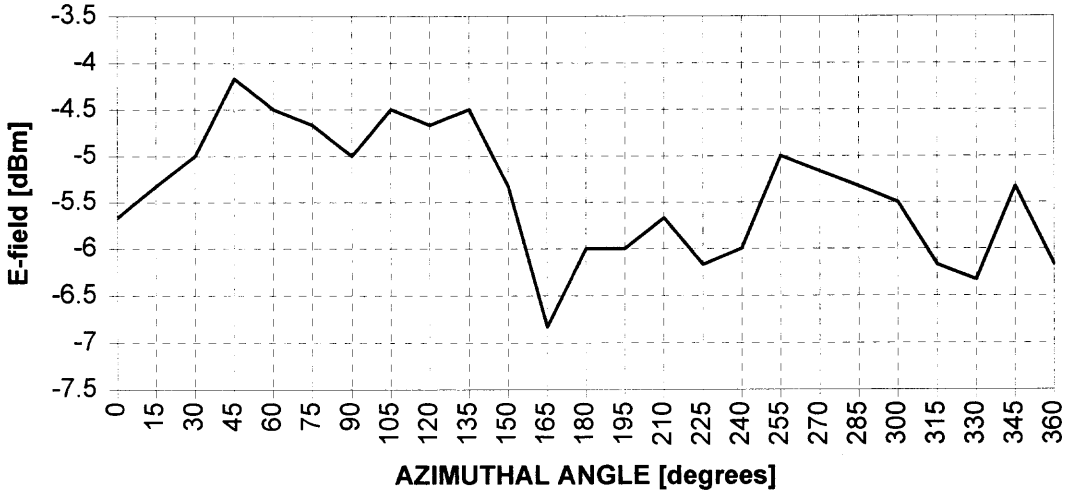

Figure 4.5b Transmitted power variation vs. azimuthal angle, d_{sphere} = 31 mm, n_{sphere} = 1.5, 4 layers, 10 GHz. Note range of the vertical axis is 4.0 dBm.

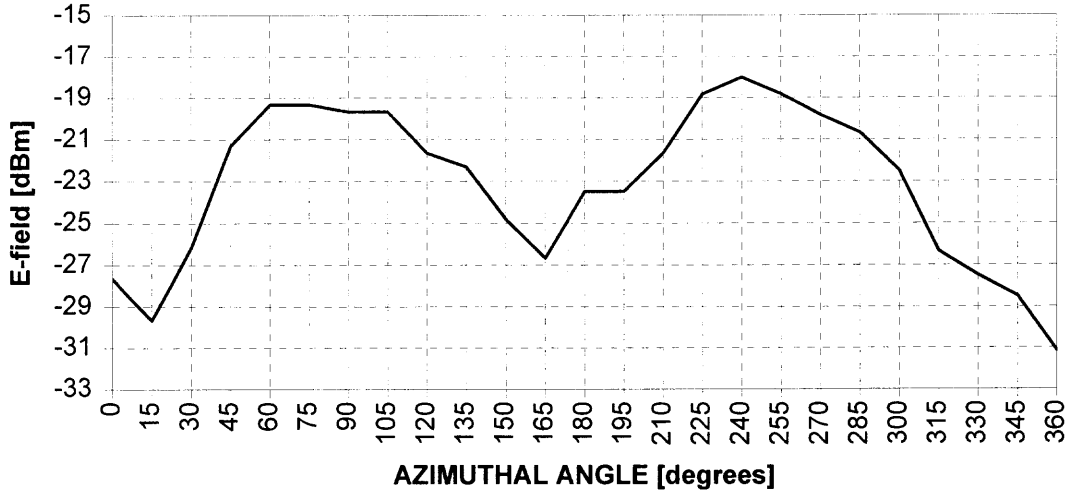

Figure 4.5c Transmitted power variation vs. azimuthal angle, d_{sphere} = 31 mm, n_{sphere} = 1.5, 4 layers, 15 GHz. Note range of the vertical axis is 18 dBm.

4.2.3 Comparison to Simulations

The simulations generally predict larger power variations at the two-layer 5 and 10 GHz results. This can be explained by the larger Λ of the simulation compared to the close-packed structure. When the simulation is rotated there can be azimuthal angles where there are gaps in the dielectric media in line with the polarization direction of the wave, similar to a grating. This cannot happen in close-packed crystal. Gaps may be especially prominent for the two-layer case. In simulation, the peak-to-peak transmitted power variation is significantly less for the four-layer results than the two-layer results. In the four-layer case, there are generally fewer gaps. In contrast, the transmitted power trend in the experiment indicates transmission variation enhancement as the number of layers increases. Also recall that the effective wavelengths λ_{neff} are larger in simulation due to the low packing density (or filling fraction) of the crystal. Comparing the two and four

layer simulation results for 10 and 15 GHz results in similarity to the experimental results. The response across the range of ϕ (which is only 180° for simulations) is flatter at 4 layers and at 15 GHz, the plot transitions from several maxima to a single dominant maxima at $\phi = 0°$ with a series of smaller periodic maxima across the remaining range of ϕ. Qualitatively, at least, the simulations predict the combining of field maxima as the number of layers increase when $\lambda_{neff}/\Lambda \approx 0.5$. Without the ability to simulate a close-packed structure, simulating the effect of azimuthal crystal rotation on the transmitted power is somewhat inaccurate.

4.3 Examination of Polarization Mixing in the Close-Packed fcc Structure

Reflection polarization mixing is reported on finite two-dimensional photonic crystal waveguides[39] as a function of azimuthal angle, ϕ. In this effort, transmission measurements were made of two-dimensional, low filling fraction (22% and 30%) photonic crystals with λ_{neff}/Λ ranging from two to five. In this case, simulations and numerical methods also failed to characterize the true polarization state of the output and reflected beams, that is, locating polarization-mixed modes for the two-dimensional case. Characterization of the polarization mixing quality in photonic crystals is useful so that specific birefringent symmetries to control mode energies and mode polarization can be realized. The experimental apparatus used in the experiments presented here is ideally suited for the detection of polarization mixing. Only a small modification of the apparatus is required: the receiving antenna is fixed at 90° with respect to the transmitting antenna while the crystal is rotated about its z-axis. In so doing, it is possible to detect

transmission polarized perpendicular to the transmitter as opposed to the previous results which detect transmission in the parallel direction.

The results, (Figures 4.6a-c) suggest a small birefringent effect with respect to azimuthal angle, ϕ. This is particularly true at 5 GHz since the detected power of the perpendicular polarized modes is not far below the parallel polarized modes, as they do with an increase in frequency[32]. Further evidence for this is established by the loss of transmitted power in the perpendicular polarized modes as the frequency increases. Examining the experimental results, the loss of power in the perpendicular modes occurs at 10 GHz and continues in the 15 GHz results.

4.4 Conclusions

The experimental results reveal several interesting observations of the effect of azimuthal morphology changes in the fcc crystal on transmissivity. These variations appear to be based on the location of crystallographic planes rather than the rotational symmetry of the fcc crystal. The effect appears to be more pronounced at lower λ_{neff}/Λ ratios. Despite the fact that power variation is much greater when the number of crystal layers are increased, qualitatively the transmission is similar for changes in the number of layers of crystal media. Since the effect is predominant where $\lambda_{neff} < \Lambda$, it is possible that the self-imaging distance may occur within a layer and consequently be lost to the observer. Although it is possible to make these observations from the information gained, it is difficult to draw more concrete conclusions.

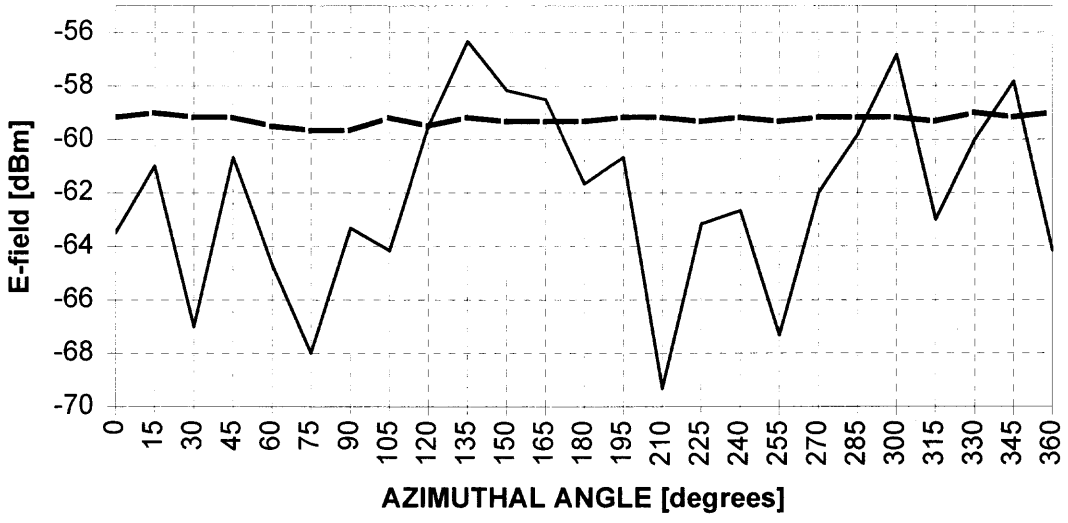

Figure 4.6a Transmitted power variation vs. azimuthal angle, d_{sphere} = 10 mm, n_{sphere} = 1.5, 4 layers, 5 GHz, vertical polarization (dashed) and perpendicular polarization (solid line).

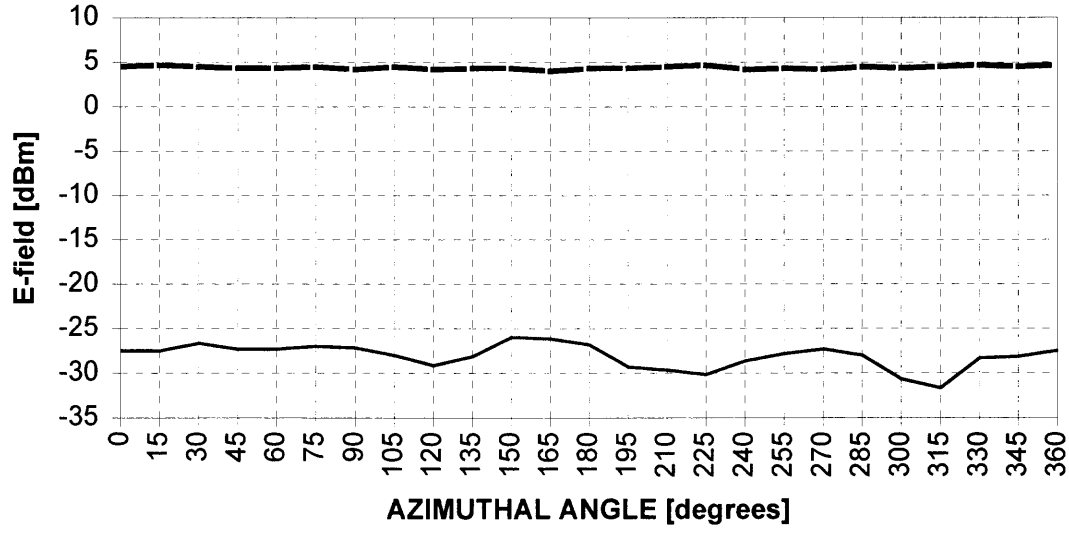

Figure 4.6b Transmitted power variation vs. azimuthal angle, d_{sphere} = 10 mm, n_{sphere} = 1.5, 4 layers, 10 GHz, vertical polarization (dashed) and perpendicular polarization (solid line).

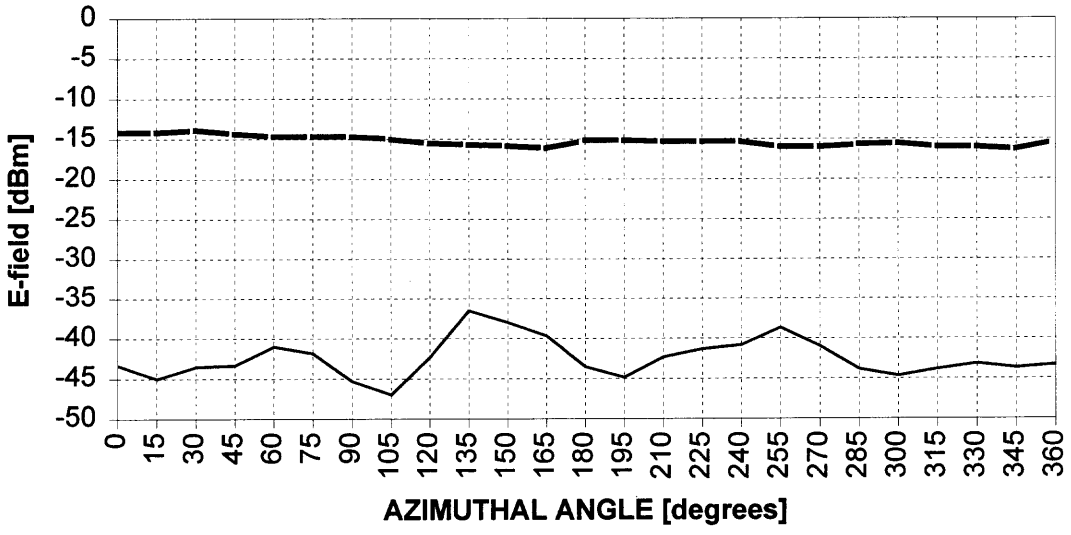

Figure 4.6c Transmitted power variation vs. azimuthal angle, d = 10 mm, n = 1.5, 4 layers, 15 GHz, vertical polarization (dashed) and perpendicular polarization (solid line).

Overall, simulations provided qualitative insight into the nature of the phenomena. The simulation results agree qualitatively with the experimental results but do not yield a precise match to the experiments. Typically, the simulations yielded larger power variations than the corresponding experimental values, however, the location of power maxima or, minima did not match the experiment. This was attributed to the conditions forced by the computational limitations of the simulation. Simulation were successful in producing *the number* of maxima, which only in some cases, were correlated with the exact experimental azimuthal angles, ϕ. While the finite element approach was found to be somewhat successful in determining the self-imaging distances[37], it was unsuccessful in determining the true polarization state of the output wave.

To gain more information about this effect, the crystal morphology dependency on transmission is explored by combining modification of the incident angle with azimuthal variation.

CHAPTER 5

VARIATION OF INCIDENT AND AZIMUTHAL MORPHOLOGY

5.1 Introduction and Experimental Setup

This segment of the experimental program is important, since the beam transmission was varied through different Brillouin zone directions, which may affect the pass band of the radiation. Recalling the band diagrams for the photonic crystal, note that the slope of the band may change as the variation is implemented. Numerical simulation predicted transmittance variation as a function of the incident beam angle as well as ultrarefractive effects[31]. In addition, nonlinear experiments exhibited the role of 'magic angles'. At these angles, the transverse component of the wavevector is prohibited from propagation and nonlinear characteristics are substantially amplified[40]. Thus, the purpose in this portion of the experimental program is to reveal the role of wave polarization around these angles by varying the azimuthal orientation of the crystal and incident angles.

Wave propagation in photonic crystals is rather complex [41]. Most of recent efforts were spent in identifying the band-gap properties of the structure. Yet recent efforts are recognizing the possible usefulness of photonic crystals as optical components operating in frequency regions near the band gap[42]. To this end, with nonlinear properties in mind, one would like to assess the amplitude and phase of the electromagnetic field at every point within the photonic crystal. This task is not simple since the propagation properties are comprised of local modes (intra-modes) within the high-dielectric features in addition to propagating modes (inter-modes). As a consequence, the experiment is limited to a study of transmission variations. The crystallographic planes that interact with the beam

are also affected. Up to this point in the experimental program, the plane of interface is the (111) plane. As the incident angle is varied from $\theta = 0°$ to 25°, different crystallographic planes become the incident plane, changing the interplanar spacing and consequently modifying the propagation of modes with a particular wavevector, k. For example, the (221) plane is the incident plane at approximately 16° and (321) at 22°.

In this experiment, the incident and azimuthal angles of the beam are varied, as illustrated in Figure 5.1. All other components of the experimental setup remain as in the previous experiments. Transmission variations at self-imaging distances are examined since it provides, among other things, a natural means to collect the entire radiation

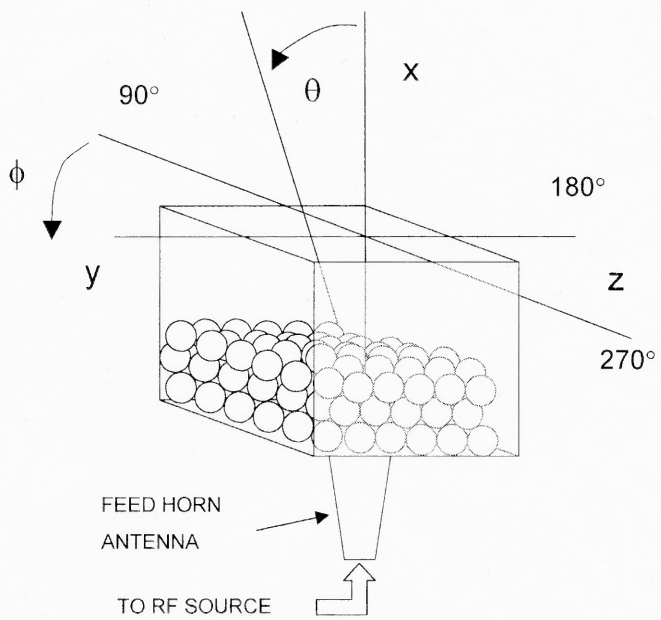

Figure 5.1 Illustration of experiment. Incident angle, θ, is varied from 0 to 25 degrees while ϕ is varied from 0 to 360 degrees. θ remains in the x-y plane as the crystal is rotated.

output. As a first step, the polarization dependence of multi-mode beam propagation was studied where the propagating wavelength is smaller, comparable to, and larger than the

corresponding scattering feature size. As before, photonic crystals used in the experiments were scaled up into the microwave spectrum to emulate artificial opal in the other spectral regions and in particular, the optical spectrum. To verify the scaling validity microwave experiments are correlated to optical experiments on a corresponding artificial opal.

5.2 Results

The experimental results are plotted in Figures 5.2a-c to illustrate the effect of changing the incident angle, θ, through the entire range of the azimuthal angle, ϕ, at a particular frequency. At 5 GHz there is some additional loss as θ increases, but the overall shape of the curve over the range of ϕ does not vary greatly. The additional loss may be explained by the increase of media thickness through which the beam has to pass as θ increases. At 10 GHz, as $\lambda_{neff}/\Lambda < 1$, the qualitative nature of the curves change considerably. As θ is increased from 0° to 10°, loss is incurred as previously however, as θ is increased from 10° to 15°, the original waveshape is restored and the transmission peak at $\phi = 210°$ is actually a few dBm higher, suggesting an imaging effect. Continuing to increase θ from 15° to 20° results in a change in from transmission maxima to a minima at $\phi = 180°$-210°. Finally at $\theta = 25°$, the original waveshape, with a transmission maxima at ϕ = 180°-210° is restored. As the frequency is increased to 15 GHz continuing the trend of decreasing λ_{neff}/Λ, the characteristic double maxima at 90° and 180° becomes progressively weaker and is ultimately lost at $\theta = 20°$. Further increase to $\theta = 25°$ results in a flatter transmission profile over the range of ϕ, with minor maxima at 0° and 180°. Again, this is an "inverse" effect than that observed at 10 GHz. Note that

all of the results beyond the initial $\theta = 0°$ incident angle is essentially without change in loss.

Two generalized conclusions can be drawn from the experimental data:

1) $\lambda_{neff}/\Lambda = 1$ appears to be a transition point for the nature of the effect of θ variation.

2) $\theta = 10°$ and $20°$ appears to mark other transition points for the effect of θ variation on transmission of the beam through the media.

To further explore and better illustrate the dependence of the transmission on θ, ϕ and f, the following contour plots (Figures 5.2a-c) show the transmitted power at the center of the structure for a four layer close-packed fcc (or hcp) structure, at frequencies *f* = 5, 10 and 15 GHz, respectively. The structure remains as spheres of d = 31 mm, $n_{sphere} = 1.5$.

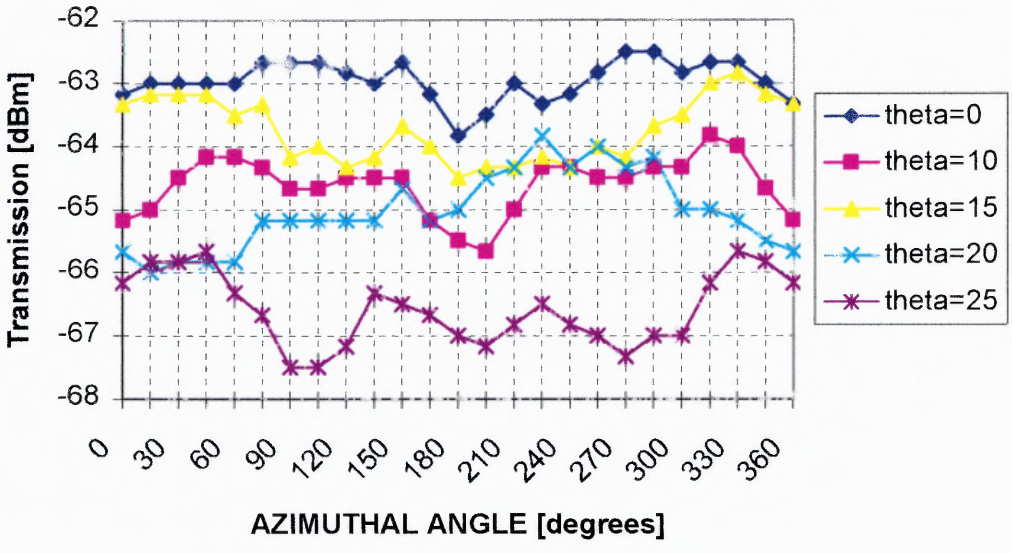

Figure 5.2a Transmission through four-layer fcc crystal as a function of ϕ, θ, 5 GHz, $d_{sphere} = 31$ mm, $n_{sphere} = 1.5$.

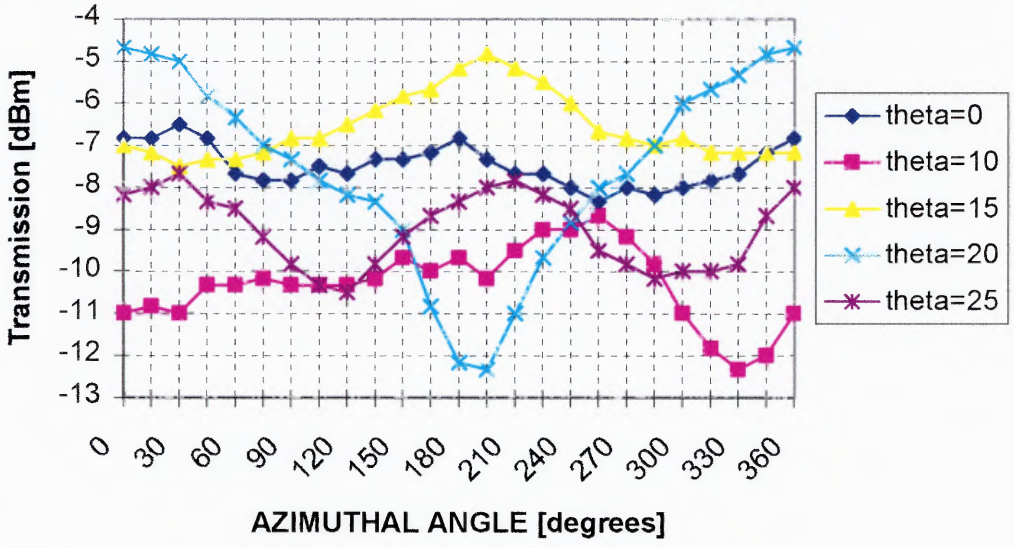

Figure 5.2b Transmission through four-layer fcc crystal as a function of ϕ, θ, 10 GHz, $d_{sphere} = 31$ mm, $n_{sphere} = 1.5$.

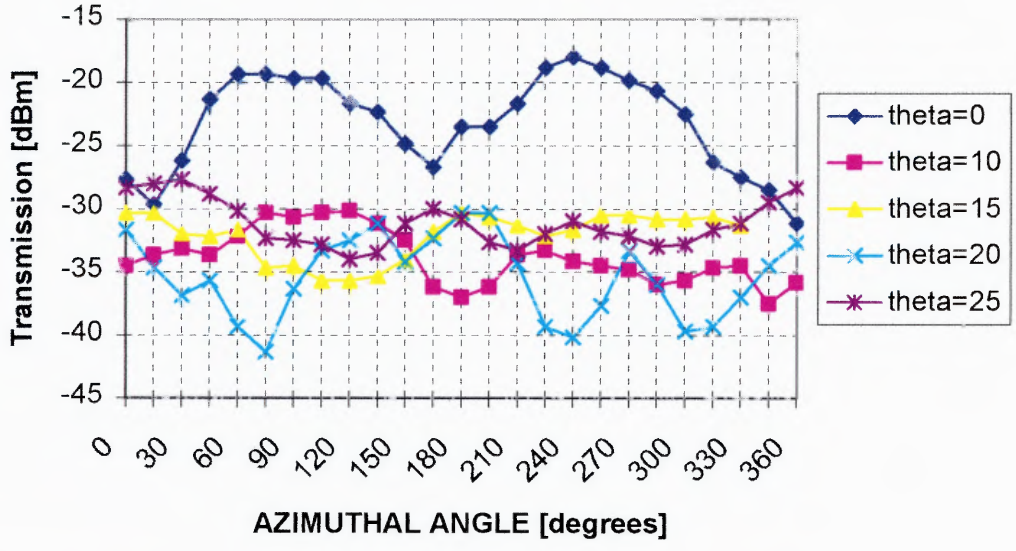

Figure 5.2c Transmission through four-layer fcc crystal as a function of ϕ, θ, 15 GHz, $d_{sphere} = 31$ mm, $n_{sphere} = 1.5$.

Depiction of the information in three-dimensions better guides the eye in visualization of the effects changing the variable θ, ϕ and f. Using a two-layer structure, the transmitted intensity is mapped in Figures 5.3a-c, in dBm, at the self-focusing point (y = z = 0) as a function of incident angle, θ and azimuthal angle, ϕ, at a given frequency. In Figures 5.4a-c the transmitted intensity is plotted in dBm, as a function of frequency through a range of the azimuthal angles, ϕ, at a given incident angle, θ. The values in these plots were adjusted to account for changes in detection and reception efficiencies over the frequency range of interest.

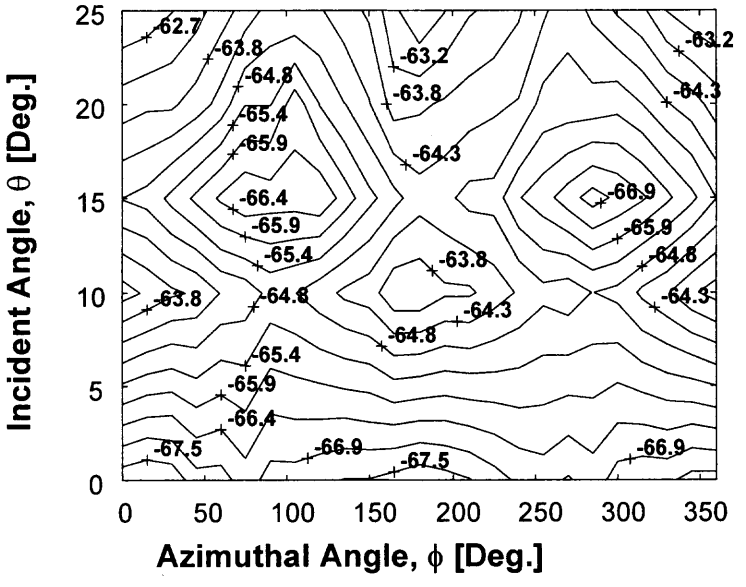

Figure 5.3a Contour plot of transmitted intensity [dBm] at the self-imaging point as a function of incident and azimuthal angles at f = 5 GHz.

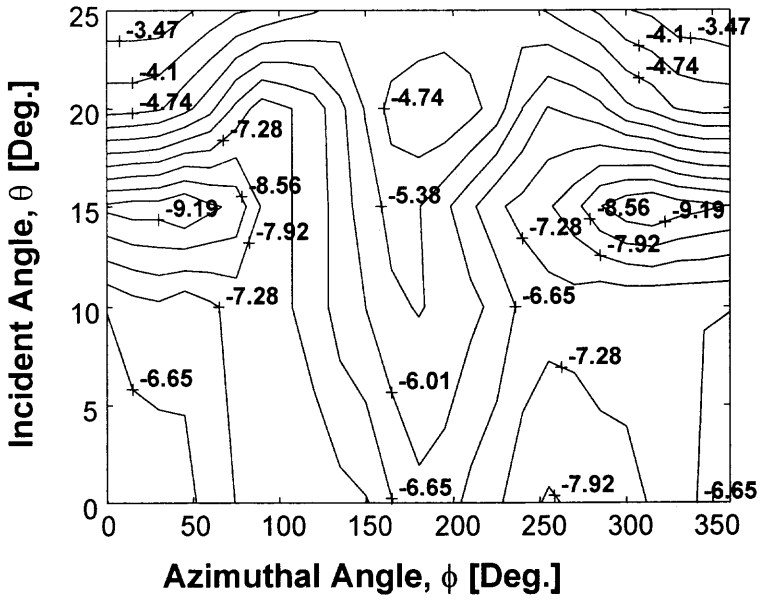

Figure 5.3b Contour plot of transmitted intensity [dBm] at the self-imaging point as a function of incident and azimuthal angles at $f = 10$ GHz.

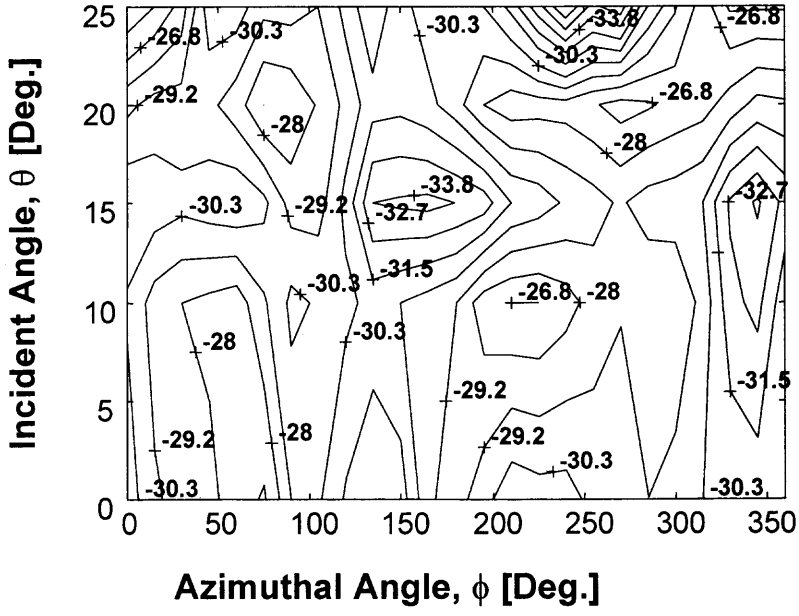

Figure 5.3c Contour plot of transmitted intensity [dBm] at the self-imaging point as a function of incident and azimuthal angles at $f = 15$ GHz.

5.3 Discussion of Results

Propagation in photonic crystals may be described by a combination of local and extended mode analysis. As was demonstrated, many simulation programs fail to give adequate results. For that reason, a systematic mapping of the transmission through the photonic crystal was undertaken.

The transmission through the cubic, close-packed structure is governed by the four-fold symmetry when the direction of propagation is made along the <111> direction and the radiation is integrated. In addition, the structure has two major directions for which the propagating beam is transversely prohibited: these are the <100> and <110> directions. The results show that the number of excited modes depends on the incident angle, θ, azimuthal angle, ϕ, and the numerical aperture of the incident beam. Yet, one should expect that the number of transmission maxima as a function of azimuthal angle, ϕ, doubles when the incident angle is close to the transverse confining situation.

Such behavior is indeed demonstrated in all measurements. The positions of these maxima vary as a function of the incident angle and frequency. Transmission variation at points of rapid phase shift has been simulated for thin two-dimensional sub-wavelength photonic crystal[31]. From these studies, ultrarefractive behavior was predicted with effects ranging from transmitted power variation, a transmission analogy to Goos-Hanschen shift, beam widening and beam splitting. Unfortunately, there is no equivalent rigorous numerical technique for three-dimensional crystals. Yet, these experimental results demonstrate analogous behavior in the three-dimensional case. Large transmission variations in the vicinity of rapid phase shifts are correlated with transverse confinement of the wave propagation. These transverse confinements imply the

existence of 'magic angles', for which the transverse component of the wavevector is prohibited from propagation. This means, $k_x = k_0 n_{eff} \sin(\theta) = q\pi/\Lambda$, with q = 1/2,1,2,3..., where Λ is the structure pitch and n_{eff} = 1.369. For example, at f = 10 GHz, one magic angle is calculated at $\theta = 21^\circ$ and $\theta = 10^\circ$, for Λ = 31 mm, q = 1 and q = 1/2, respectively. Another angle exists for $\sqrt{2}\Lambda_0$: this occurs at $\theta = 14.5^\circ$ for q = 1. Changes in the nature of the beam transmitted through the crystal are observed at, or near these angles. Figure 5.3b exhibits a transition to a single peak at $\theta = 10^\circ$ and 25° from two peaks at $\theta = 0^\circ$ and $\theta = 20^\circ$. For example, these changes are observed for $\phi = 0^\circ$ and $10^\circ < \theta < 25^\circ$ in Figure 5.3b. The effect of change in the number of peaks is more pronounced for the optical data (Figure 5.6): there, the $\Delta\phi = 45^\circ$ interval is replaced by $\Delta\phi = 90^\circ$ through the 'magic angle' of $\theta = 18^\circ$ (q=1/2).

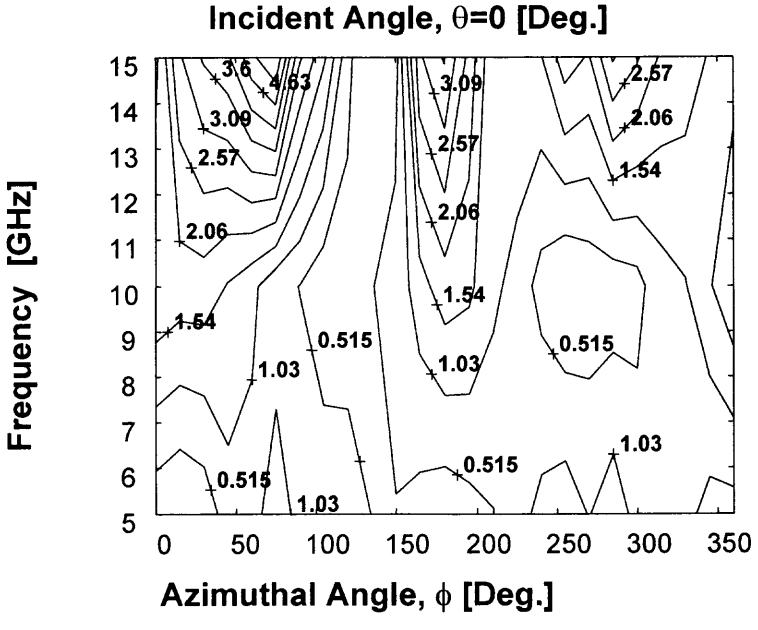

Figure 5.4a Contour plots of transmitted intensity variations [dBm] as a function of radiation frequency and azimuthal angles at an incident angle of $\theta = 0$ degrees.

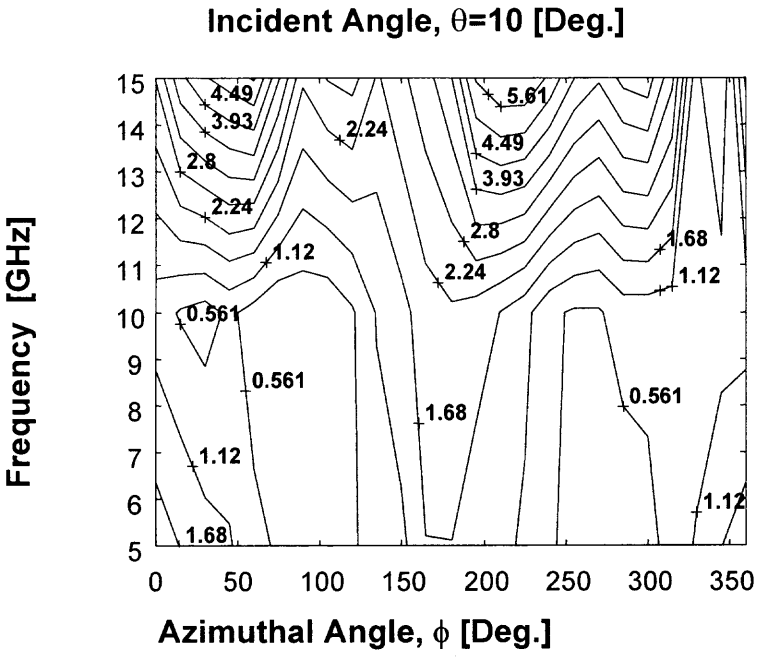

Figure 5.4b Contour plots of transmitted intensity variations [dBm] as a function of radiation frequency and azimuthal angles at an incident angle of $\theta = 10$ degrees.

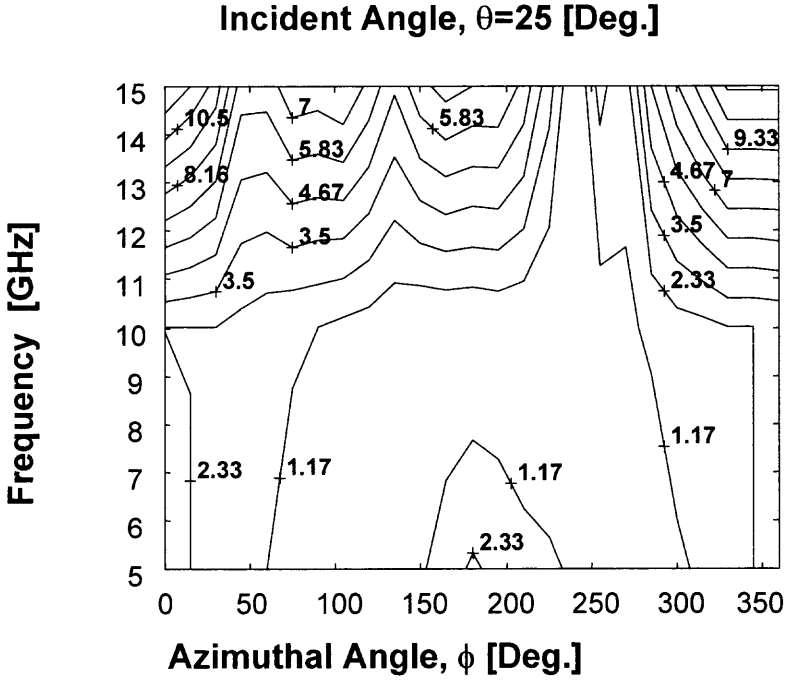

Figure 5.4c Contour plots of transmitted intensity variations [dBm] as a function of radiation frequency and azimuthal angles at an incident angle of $\theta = 25$ degrees.

The change in peak characteristics is also pronounced as the radiation wavelength becomes comparable to sphere's size. This corresponds to a frequency of approximately 9.7 GHz. For example, in Figure 5.4b, note the change in number of peaks and their characteristics close to the magic angle of $\theta=10^{o}$ as the frequency is scanned from f = 5 to f = 15 GHz. At the $\phi = 0$ axis, the power decreases from 2.00 dBm to 0.83 dBm from 5 to 10 GHz and then increases to 2.83 dBm at 15 GHz. (The power values are adjusted for changes in signal sensitivity over the frequency range in order to make a valid comparison). This is also true for f~10 GHz near the other 'magic angle' of $\theta = 22^{o}$ (Figure 5.4c at $\theta = 25^{o}$). These changes are more pronounced in Figure 5.5 at $\theta = 10^{o}$, where the arrows point to the position of the peaks with $\Delta\phi=90^{o}$ interval.

By comparison, the overall transmission was decreased at the 'magic' angles where more peaks appear. This is true for both optical and microwave experiments. Note that the optical sample was twenty wavelengths thick compared to the corresponding 2.5 wavelengths thick microwave sample. Crystal imperfections and therefore, couplings between polarization modes may explain the additional peaks in the optical experiments.

In Figure 5.5 the transmission variations at 10 GHz across four layers of sample is revisited for $\theta = 0^{o}$, 10^{o} and 15^{o}, respectively. The angle $\theta = 10^{o}$ is close to the predicted 'magic angle'. The doubling or even quadrupling of number of transmission peaks is evident.

A similar experiment was conducted using laser radiation[32] of $\lambda = 0.532$ microns and an artificial opal structure with sphere diameter of d = 0.300 microns (Figure 5.6). The effective index of refraction of the structure was, $n_{eff} = 1.35$. In these experiments,

the opaline structure contained 40 layers. Both angles of incidence and azimuth were varied. Figure 5.6 illustrates intensity data taken at two degree intervals while rotating the structure from $\phi = -50$ through $\phi = +50$ degrees at angles of incidence varying from 16° to 20°. The periodic intensity variations may be observed at approximately $\Delta\phi = 45^{\circ}$ intervals at the 'magic angle of $\theta = 18^{\circ}$. The situations change just below or above this angle.

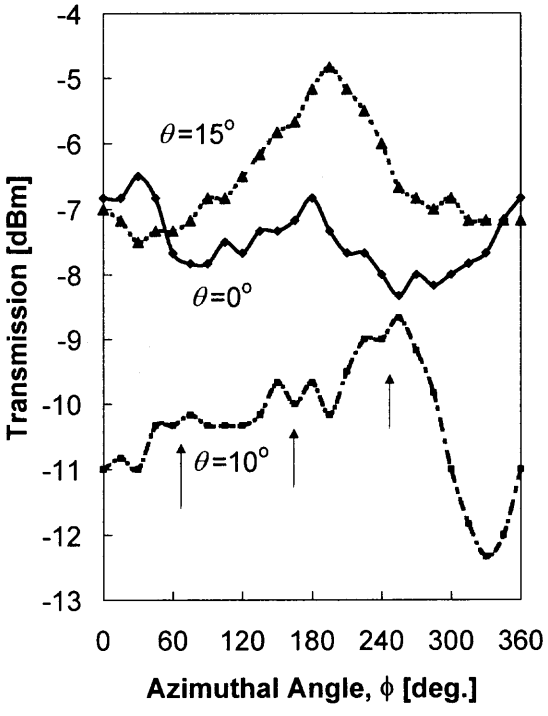

Figure 5.5 Transmission through 4-layer fcc crystal as a function of ϕ, θ, $d_{sphere} = 31$ mm, 10 GHz, revisited. Emphasis is placed on the position of the peaks, denoted by arrows. (a) Incident angle, $\theta = 0$ degrees. (b) Incident angle, $\theta = 10$ degrees (close to the 'magic' angle). (c) Incident angle, $\theta = 15$ degrees.

5.4 Correlation to Simulations

It was concluded in simulations provided qualitative insight into the nature of azimuthal angle (ϕ) variation. In that effort, simulation results agree qualitatively with the

experimental results but do not yield a precise match to the experiments. Due to the conditions forced by the computational limitations, it appeared that simulation of incident angle variation would be too far removed from the physical reality of the system under study and would not reveal any new facts. Worse, since the features modified are critical parameters for the formulation of the photonic band gap, it was thought the approximations may even provide misleading data. Although simulation has some use in determining the self-imaging distances[37] it is clear that it did not determine the true polarization state of the output wave[32]. Consequently, simulations were abandoned for this portion of the study.

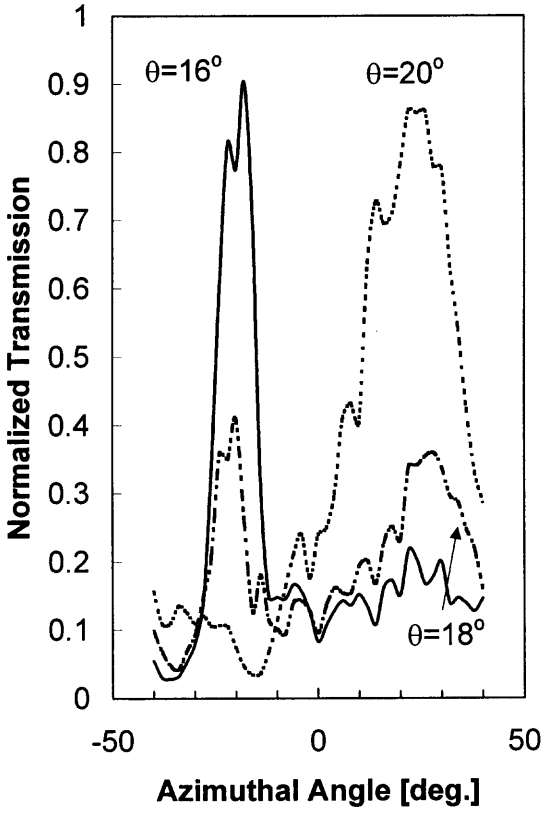

Figure 5.6 Experimental results for artificial opal, $\lambda = 0.532$ μm, $d = 0.300$ μm. The structure consists of 40 layers with an approximate total thickness of 10 μm. The data is normalized to a reference signal.

5.5 Conclusions

In summary, it is demonstrated that the transmitted intensity variations occur at regular intervals depending on the spatial orientation of the fcc crystal structure with respect to the polarization of the input beam. These variations can be correlated with the crystallographic symmetry in addition to transverse Bragg confinements. Due to the complicated nature to the propagation through the media, it is difficult to formulate numerical or simulation models to accurately predict the precise behavior. Better simulation tools are needed to grasp the full notion of these three-dimensional structures. These findings provide insight to wave propagation in three-dimensional photonic crystals and specifically in the optical regime, since it is demonstrated that the results are scalable.

CHAPTER 6

HYBRID METAL – DIELECTRIC PHOTONIC CRYSTALS

6.1 Introduction

One can easily see that the dielectric contrast is a key design parameter in photonic crystal fabrication. In most photonic crystals, the variation of dielectric contrast is actually accomplished by increasing the air space between the dielectric media or increasing the dielectric thickness between air spaces in negative contrast crystals. In this phase, a radically different approach is tried. A hybrid metal-dielectric crystal is constructed to alter the dielectric contrast of the media (in all three dimensions) as well as the effective overall dielectric constant of the media.

Usually, the addition of metal elements into a waveguide would be expected to incur losses that may be unacceptable to performance. Recent work, however, suggests that this may not be the case. In recent work by Ebbesen, a hexagonal array of subwavelength circular apertures is claimed to have greater than unity transmission efficiency[7]. While there is some dispute about this claim, the observations were in opposition to the expected transmission efficiency $t \propto d/\lambda^4$, where d is the aperture radius. Thus, according to Ebbesen, the intensity of the transmission would be expected to fall off as $I \propto \lambda^{-1}$ with range from the aperture array.

In the experimental results demonstrated thus far, there is an analogous behavior with subwavelength imaging and transmission through crystal. Consequently it is assumed that analogous behavior is possible in photonic crystal with metal elements. Several effects are possible. Assume that the overall dielectric contrast of the system

may be locally increased between crystal planes. On the other hand, the effective medium viewpoint will lower the overall medium contrast between the bulk crystal and air due to the addition of the metal elements into that crystal plane. From the viewpoint of grating theory, electromagnetic surface waves (surface plasmons) will be excited in the metal components, consequently affecting transmission. This must occur through coupling of the surface plasmon modes with the propagating modes of the transmitted beam. Thus a discussion of surface plasmons is in order in preparation for the next series of experiments, where analogous behavior is explored in the context of the fcc crystal system.

6.2 Surface Plasmons

Surface plasmons, or electromagnetic surface waves, can occur at the interface of a homogeneous dielectric and a periodic dielectric or at a dielectric-metal interface. In the first case, these wave modes are evanescent Bloch waves of the periodic medium, as discussed earlier. In the second, an important distinction to observe is that the transition is from a medium of positive to negative dielectric. In the context of the dielectric-metal interface, surface charges are induced in a conductor. Oscillations of the surface charges are excited in the conductor interface when the correct conditions are present. If the system under study is similar to a grating, electron momentum and the incident photons have to match with matching grating conditions for the excitation of surface plasmons. In the context of the experimental coordinate system used here, this relationship is expressed by[7]:

$$k_{sp} = k_y \pm nG_y \pm mG_z \tag{6.1}$$

where: k_{sp} is the surface plasmon wavevector: $k_y = (2\pi/\lambda) \sin \theta$, or the component of the incident beam wavevector in the plane of the media, where $\theta = 0$ is defined as normal to the plane of the media, $G_y = G_z = 2\pi/\Lambda$, the media (or grating) momentum wavevectors for a square array, where Λ is the crystallographic period or pitch and *n, m* denote integers. Ebbesen acknowledges that this effect is sensitive to polarization[7], which will be explored to some degree in this experiment. Another dependency noted in the Ebbesen experiments is the depth of the apertures in the conductor. In the context of the experimental three-dimensional analogy, this is represented by the periodic layering of conductive spheres in the fcc crystal matrix.

With this knowledge of surface plasmons, assume that the effect of the dielectric-metal media on a penetrating beam will be similar to that already seen with pure dielectric. However, it is expected that the metal components will enhance some of the effects already observed through enhancement of the formation of surface plasmons.

6.3 Experimental Setup

This experiment comprises two phases, an examination of the self-imaging distance as a function of range in the crystal and a view of how polarization affects the transmission, also as a function of range. An fcc crystal, of d_{sphere} = 10 mm polypropylene and steel spheres was assembled. The dimensions were scaled to be comparable to the wavelength of microwave radiation in the f = 5 - 15 GHz range. Minority steel spheres were placed in a next-nearest-neighbor distribution in all three dimensions within the crystal. The crystals were thin compared to the wavelength of the incident beam, not more than 10 layers of spheres, which ranges between approximately 1 to 5 wavelengths. A

microwave beam was directed through the crystal central axis of the (111) crystal face with the polarization oriented along the y-axis, as in the previous experiments. The crystal was successively built up, layer by layer, and subjected to a measurement of the transmission through the crystal at the center of the output plane through azimuthal rotation of $\phi = 0° - 360°$. Two dielectric medias were used, polypropylene ($n_{sphere} = 1.5$) and Al_2O_3 ceramic. The Al_2O_3 ceramic had a refractive index of $n_{sphere} = 2.25$, based on density[43] of the Al_2O_3 media. Consequently, it is possible to compare results with two media with significant contrast. To begin, the self-imaging qualities of the hybrid crystal are assessed. Experimental results are plotted in Figures 6.2a-c.

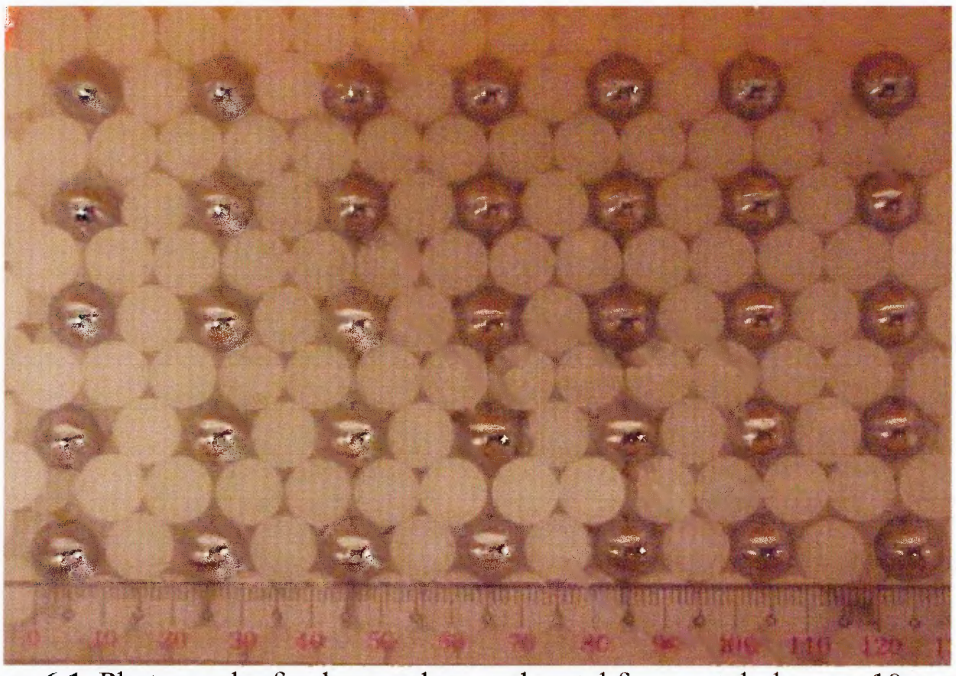

Figure 6.1 Photograph of polypropylene and metal fcc crystal, $d_{sphere} = 10$ mm. Scale on bottom of photograph is in millimeters. Beam propagation was out of the page, relative to the figure.

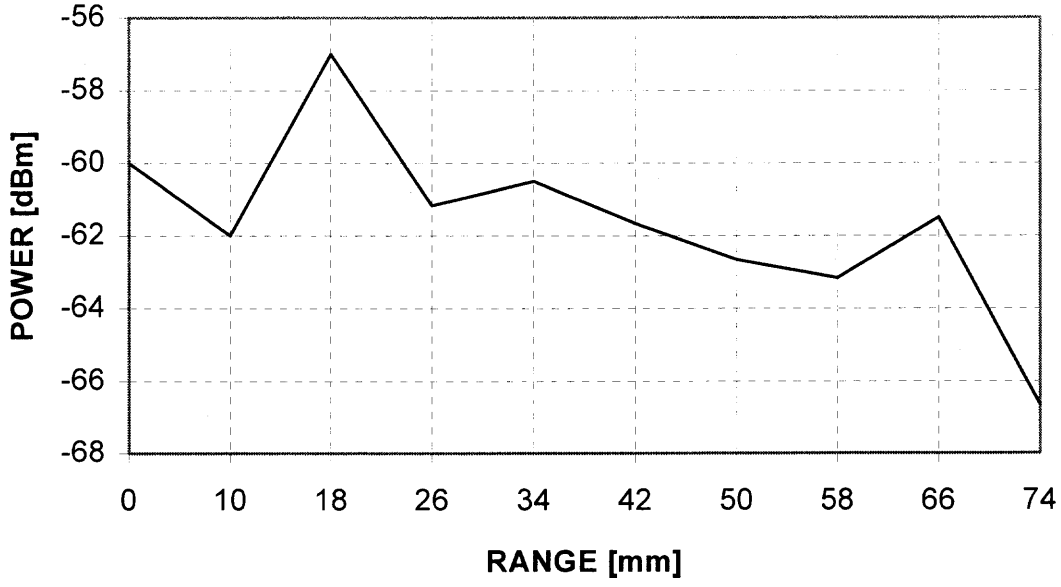

Figure 6.2a Polypropylene and metal media, d_{sphere} = 10mm, f = 5 GHz.

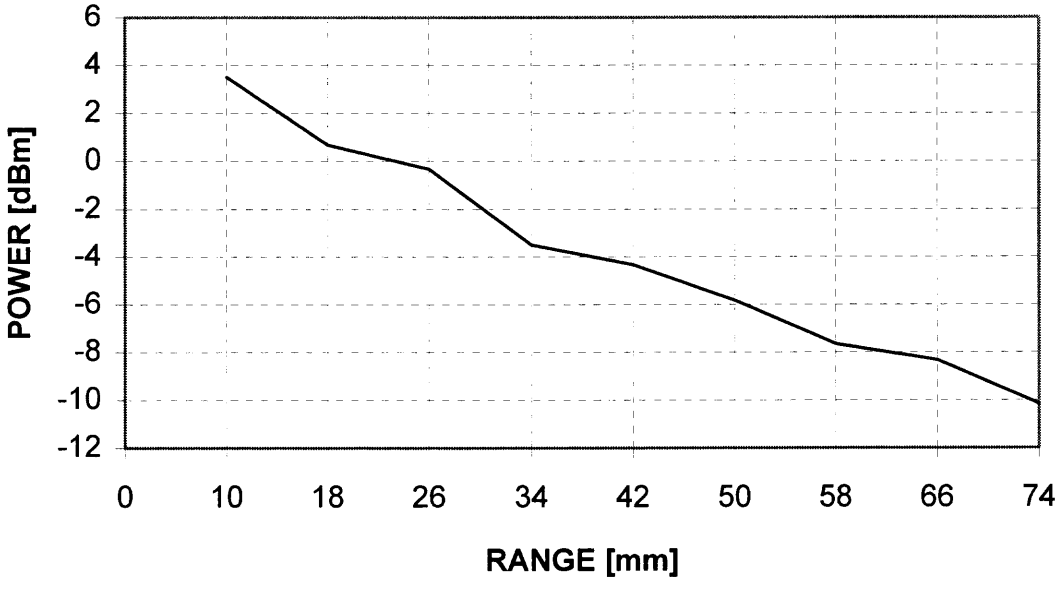

Figure 6.2b Polypropylene and metal media, d_{sphere} = 10mm, f = 10 GHz.

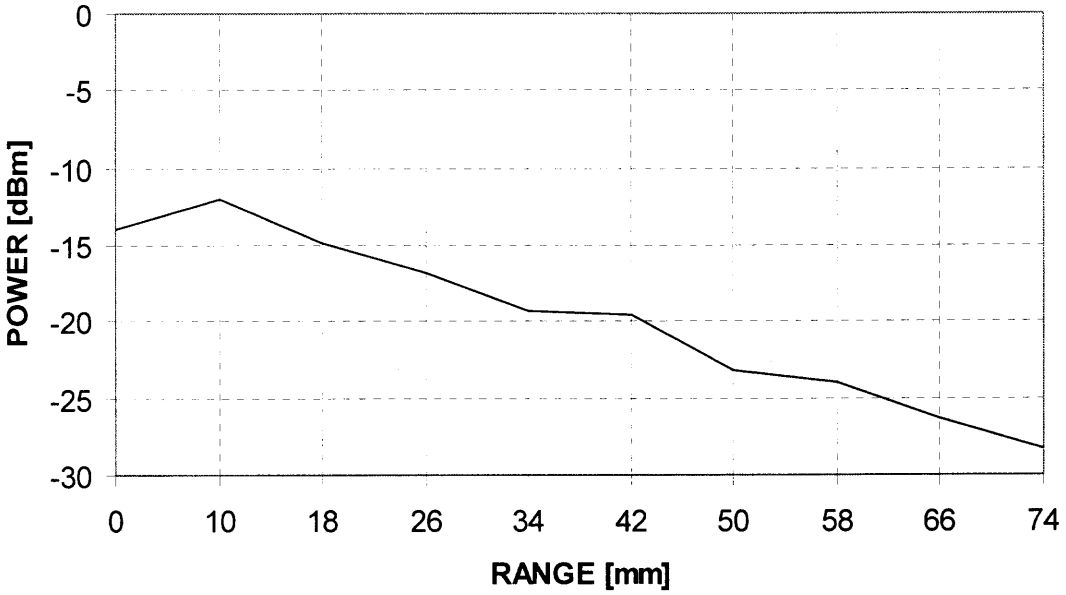

Figure 6.2c Polypropylene and metal media, d_{sphere} = 10mm, f = 15 GHz.

6.4 Results

The dielectric-metal hybrids demonstrate self-imaging qualities not unlike the pure dielectric case. Strong imaging is noted at 5 GHz and less so at the higher frequencies. This is consistent with the pure dielectric case. Changing the dielectric contrast has a greater effect than in the pure dielectric case, however. In the polypropylene-metal crystal, the imaging distance is 48 mm as demonstrated in Figure 6.2a. Yet, with the change in dielectric contrast in ceramic-metal crystal, the imaging distance changes to between 16-24 mm as illustrated in Figure 6.4a. A series of small maxima between 0.5 and 1.0 dBm is noted at 10 GHz and 15 GHz in the polypropylene-metal hybrid, illustrated in Figures 6.2b and 6.2c. The same series of maxima is present at 10 GHz in the ceramic-metal crystal. However, the waveform changes radically at 15 GHz (Figure

6.4b and 6.4c). Here there is a broad maxima at approximately 44 mm from the initial peak.

Since the strongest imaging is demonstrated at 5 GHz, there results can be examined more closely and compared to the pure dielectric cases. Note that the only change to the crystal is the introduction of metal, the crystal period, feature size, etc., remains the same. Figures 6.5 and 6.6 show that introduction of metal into the crystal changes the self-imaging period with dependency on the dielectric contrast. In the polypropylene-metal case the self-imaging distance is approximately 1.5 times that of the pure polypropylene crystal, as illustrated in Figure 6.5. The peaks are also less distinct in the polypropylene-metal case. Despite this, the interpeak loss is almost identical, which is a somewhat surprising result. Introduction of metal elements introduces a complex component into the effective dielectric constant and into the effective refractive index of the media.

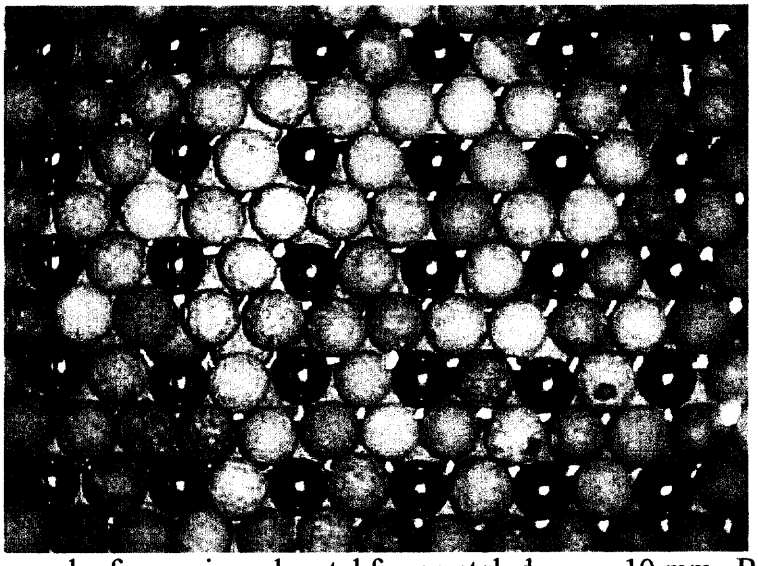

Figure 6.3 Photograph of ceramic and metal fcc crystal, d_{sphere} = 10 mm. Beam propagation was out of the page, relative to the figure.

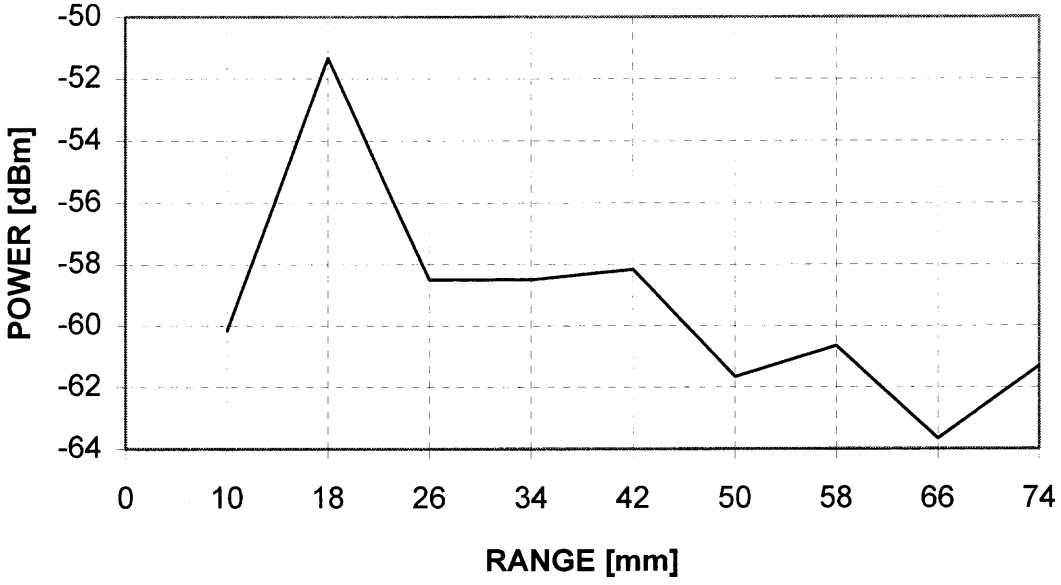

Figure 6.4a Ceramic and metal media, d_{sphere} = 10mm, f = 5 GHz.

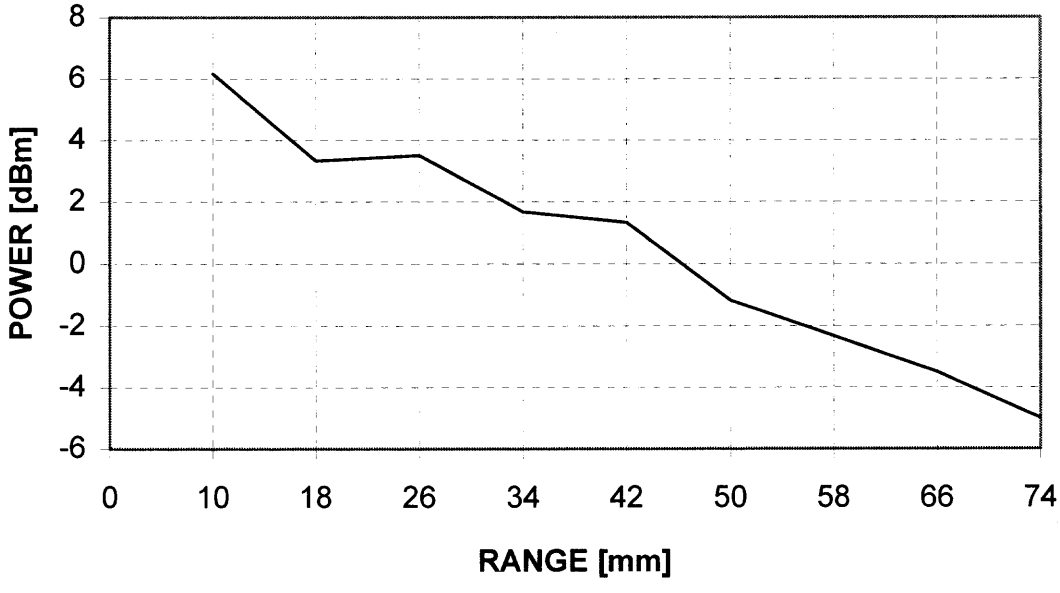

Figure 6.4b Ceramic and metal media, d_{sphere} = 10mm, f = 10 GHz.

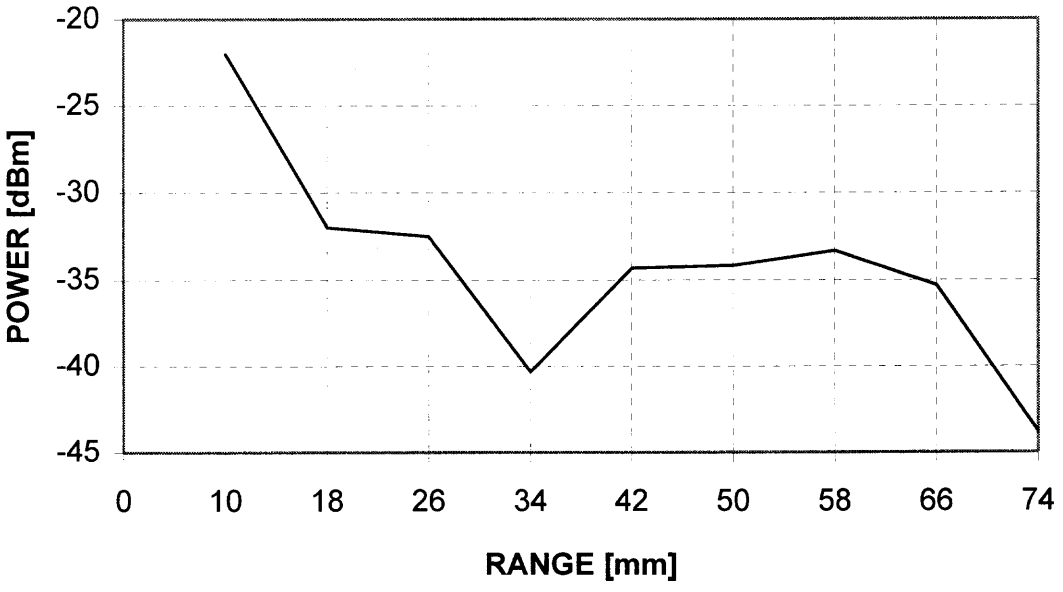

Figure 6.4c Ceramic and metal media, d_{sphere} = 10mm, f = 15 GHz.

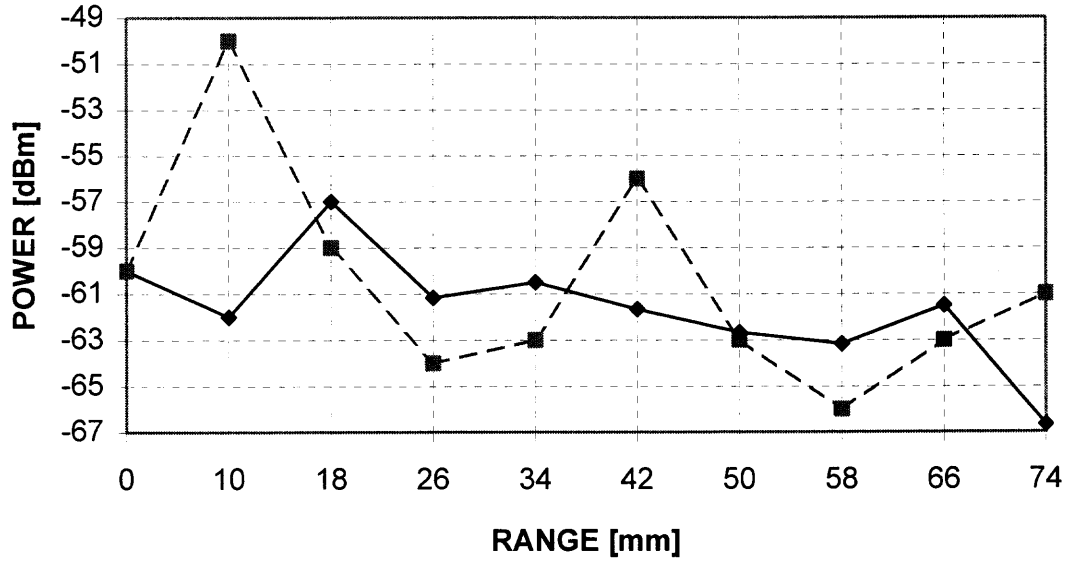

Figure 6.5 Polypropylene media (dashed line) compared to polypropylene /metal hybrid, d_{sphere} = 10mm, f = 5 GHz.

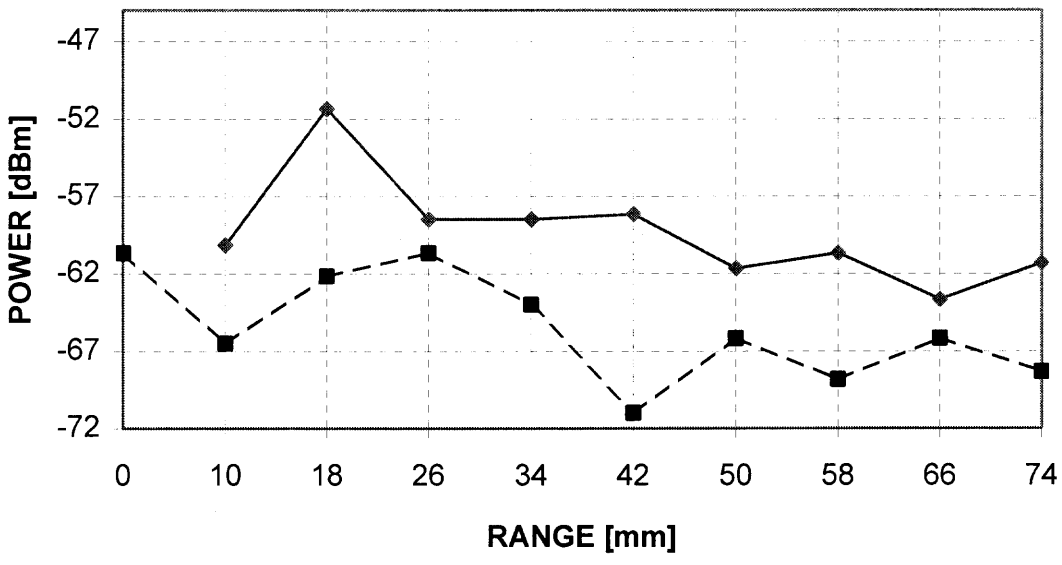

Figure 6.6 Ceramic media (dashed line) compared to ceramic/metal hybrid, d_{sphere} = 10mm, f = 5 GHz.

Thus, greater attenuation is expected than in the pure dielectric case, which is not demonstrated by these results. Figure 6.6, which illustrates the ceramic-metal crystal at 5 GHz, also demonstrates a low interpeak loss. Note that the self-imaging distance does not change significantly between the metal-ceramic case and pure ceramic crystals. Yet, the nature of waveform is different, the formation of an initial image at less range in the metal-ceramic case is observed. The peak width of this image is narrowed also. From these observations, it can be concluded that reduced dielectric contrast between the metal elements and dielectric media appears to promote the subwavelength self-imaging effect.

6.5 Discussion of Self-Imaging Observations

Analogous behavior is demonstrated between the periodic array of subwavelength apertures in metal film and metal-dielectric three-dimensional photonic crystal. As

Ebbesen notes, the mechanics of surface plasmon coupling between the front and back of the array of apertures is not well understood[7], yet it is a more complicated problem in the 3-dimensional crystals. Despite this, the effect of surface plasmons on the throughput is suspected due to the low interpeak transmission loss.

Yet, it is clear that greater than unity transmission efficiency (which is manifest in the self-imaging maxima) is possible in pure dielectric case thus the surface plasmon effect cannot be the sole contributor. One theory involves the contribution of the effect of negative permittivity. As Enoch points out, in the region approaching and in the photonic band gap, the permittivity approaches zero ultimately becoming a real negative number[31]. Consequently, the index of refraction becomes complex. This is a primary contributor to the ultrarefractivity phenomena. Thus, it can be postulated that addition of metal elements affects self-imaging through this mechanism. As observed in the first self-imaging experiments, reduction of the dielectric-air contrast resulted in a longer self-imaging period. Addition of the negative permittivity features (metal) to the crystal increased the self-imaging period here for low contrast material (polypropylene). In the ceramic case, there was little change in the imaging distance. Expected contributing factors for this were the higher permittivity material and the relatively low density of metal elements. With the contribution of the higher permittivity material, the effective index of the bulk crystal did not change greatly. However, the local, e.g., planar, index changed enough to affect the shape and nature of the waveform.

If tailoring of the fcc crystal is possible to introduce contrasting dielectric and conductive elements, it can be concluded that it is possible to control the transmissivity of the crystal, as demonstrated by these experiments. Although construction of the

macroscopic crystal is relatively simple, it is not yet possible to construct these crystals at optical wavelengths. However, the construction of hybrid-metal photonic crystals may be a field for exploration through various microfabrication techniques. There is no reason to believe that scaling this type of hybrid metal-dielectric crystal to optical wavelengths would not produce the same general results.

6.6 Variation of the Azimuthal Morphology

It is expected that transmissivity of the hybrid metal-dielectric crystal to be affected by polarization, possibly more than the pure dielectric case. It was demonstrated earlier that pure dielectric crystal is also affected by polarization in varying degrees, depending on the ratio λ/Λ. The expectation is that the crystallographic pitch, Λ, will change with the rotation of the crystal for a given polarization state. For the generally square array of metal features embedded in the fcc crystal as illustrated in Figures 6.1 and 6.3, one would expect a 90° polarization periodicity at angles of 0°, 90°, 180°, 270° or offset by 45° at 45°, 135°, 225° and 315°. In the context of surface plasmons, the media momentum wavevectors, $G_y = G_z = 2\pi/\Lambda$, change as Λ varies with respect to polarization with this periodicity also. In this experiment, the crystal depicted in Figure 6.1 was rotated $\phi = 0°$ to 360° using a procedure consistent with the previous azimuthal rotation experiment.

6.7 Results of Azimuthal Morphology Variation

Radiation transmitted through the crystal at 5 GHz has little dependence upon the azimuthal orientation for fewer layers, however, a consistent 90° symmetry becomes quite apparent at six layers evident in Figure 6.7a. At nine layers, it has a greater overall

transmissivity through the crystal. Figure 6.7b shows the transmission power variation for each layer of media. At layers six, seven and nine, the power diverges the most, however, it is only a 1-2 dBm variation. At 5 GHz the filtering effect of azimuthal orientation is weak. Examining Figures 6.8a and 6.8b (10 GHz), significant variation is noted, again with $\phi = 90°$ periodicity, beginning at layer three. As the number of layers increases, the effect is progressively stronger. The quality of the plot also changes, the symmetrical periodic behavior achieved at layer six is lost at layer nine. The minima in layer six are at approximately 90° and 270°, at layer 9 the 270° minima is lost. Figure 6.8b depicts a steady loss as the number of layers increases but greater deviation, up to 4 dBm, is noted. Steady loss with increasing layers is consistent with the self-imaging behavior observed. When the experiment is repeated at 15 GHz, the filtering effect of azimuthal angle variation is most pronounced with a minima that near 180°. Increasing the number of layers increases the prominence of this feature (Figure 6.9a-b).

6.8 Discussion

Like the pure dielectric crystal, the azimuthal variation of the dielectric-metal crystal increases with the addition of media thickness. Note that the effect is more pronounced in the metal media results for a few hybrid crystal layers, which have transmission variations greater than values obtained for the pure dielectric case, illustrated in Figure 6.10 for the 15 GHz, four-layer case. A hybrid crystal transmission difference of approximately 5-6 dBm as opposed to 1-2 dBm in the pure dielectric crystal. Note also the beginning formation of minima at an approximately interval of $\phi = 90°$ (the 90° and

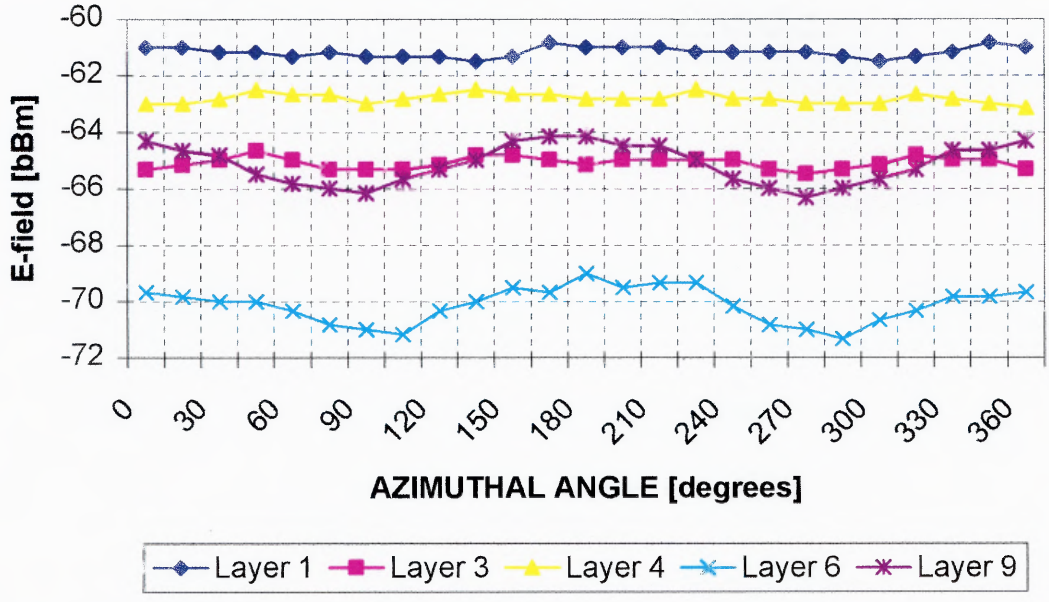

Figure 6.7a Multilayer transmission with respect to azimuthal angle, polypropylene and metal fcc crystal, d = 10, f = 5 GHz.

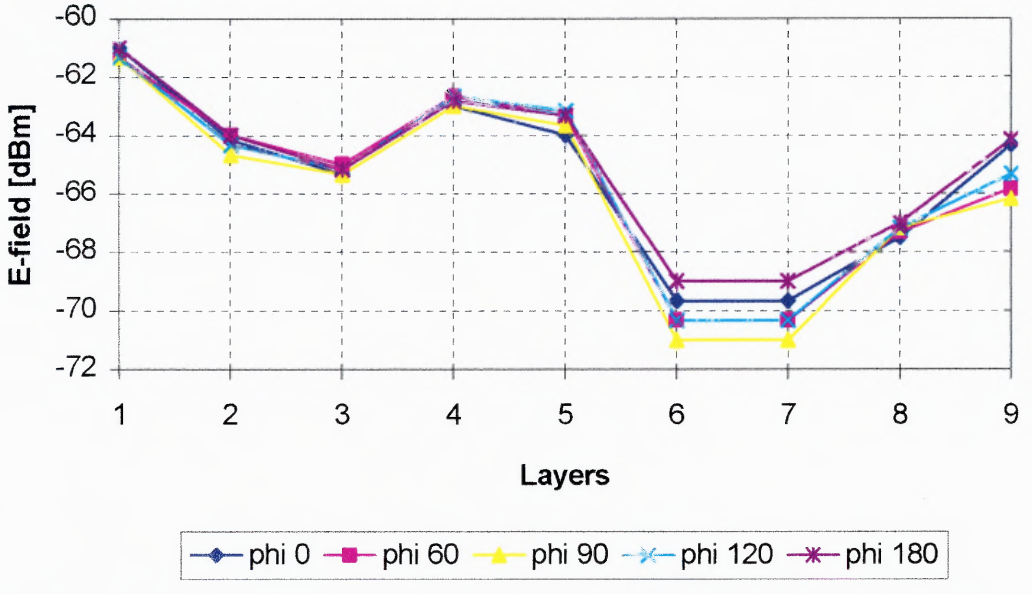

Figure 6.7b Transmission variation as a function of crystal layers, for selected azimuthal angles. Sample is polypropylene-metal, d = 10 mm, f = 5 GHz.

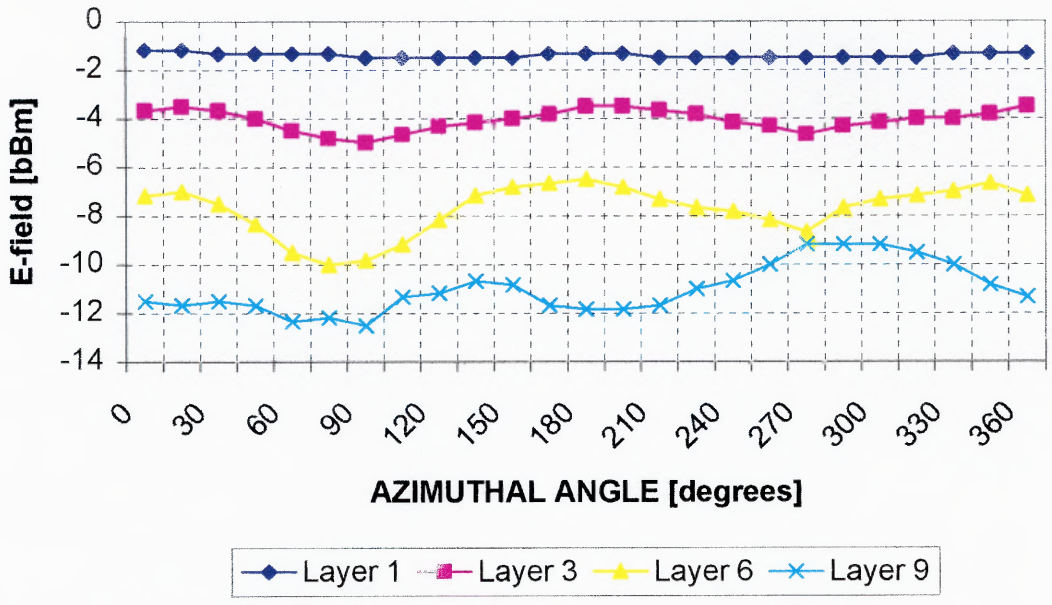

Figure 6.8a Multilayer plot of transmission with respect to azimuthal angle, polypropylene and metal fcc crystal, d = 10 mm, f = 10 GHz.

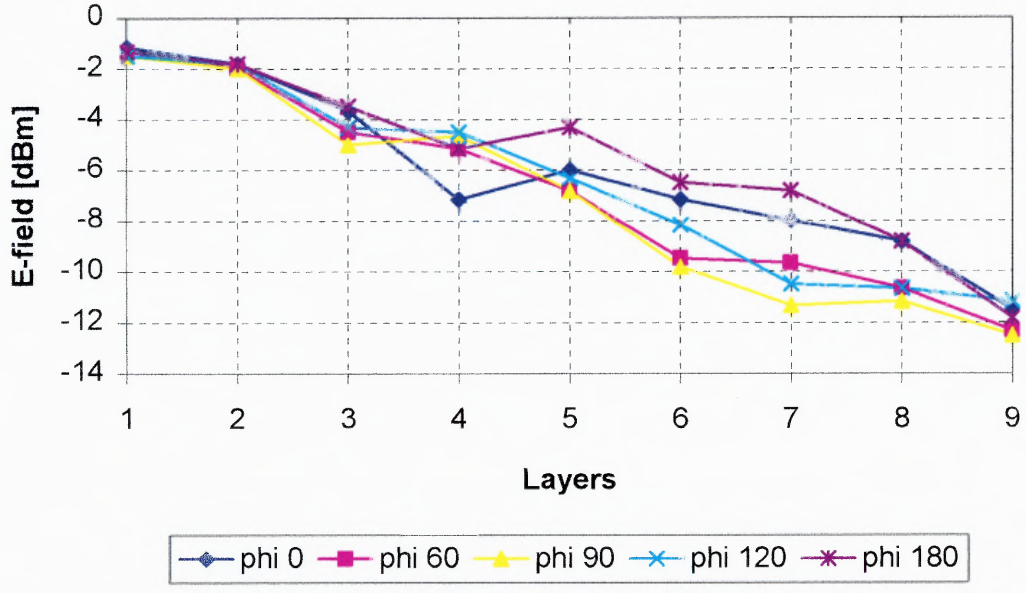

Figure 6.8b Transmission variation as a function of crystal layers, for selected azimuthal angles. Sample is polypropylene-metal, d = 10 mm, f = 10 GHz.

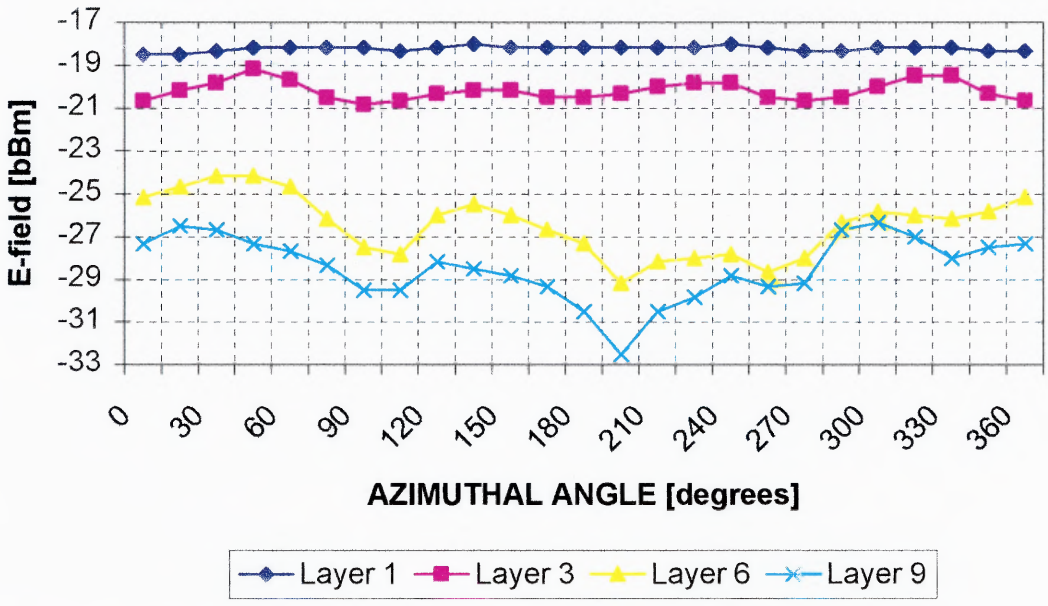

Figure 6.9a Multilayer plot of transmission with respect to azimuthal angle, polypropylene and metal fcc crystal, d = 10 mm, f = 15 GHz.

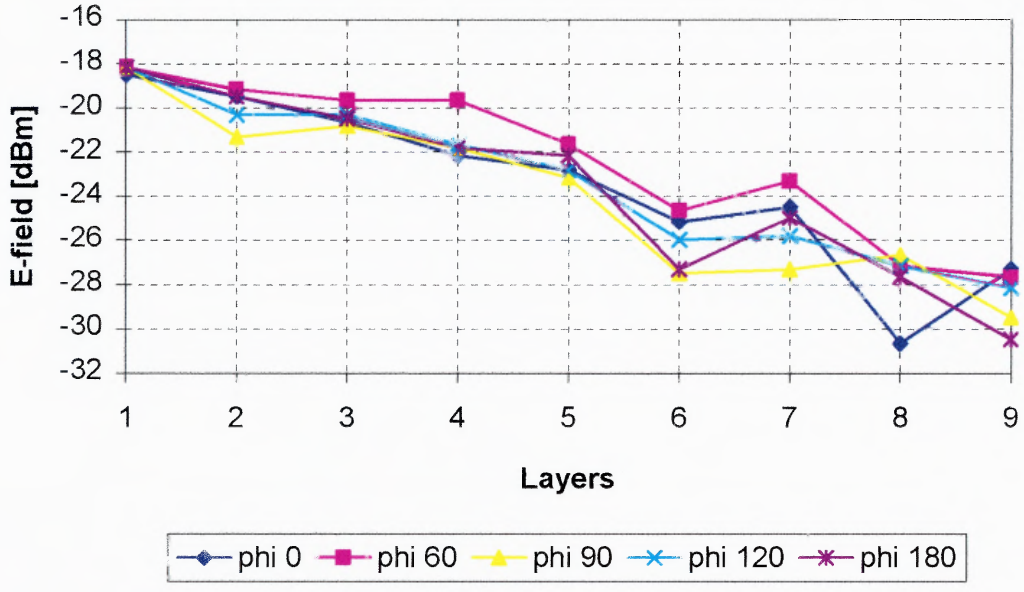

Figure 6.9b Transmission variation as a function of crystal layers, for selected azimuthal angles. Sample is polypropylene-metal, d = 10 mm, f = 15 GHz.

180° peaks are slightly skewed) which becomes more apparent at greater layer numbers (Figure 6.9a).

A few explanations can be proposed for this phenomena. It is noted that the matching of the surface plasmon wavevector material component, $G_y = G_z = 2\pi/\Lambda$, more closely matches the incident beam wavevector as the incident wavelength becomes comparable in size to the crystallographic pitch. Thus, the variation in transmission at ϕ = 90° intervals is expected as the distance between the metal minority spheres in their square array within the fcc lattice changes. Yet, artifacts like the plot for 10 GHz, 9-layer (Figure 6.8a) remain where there is an irregular transmission with respect to polarization. This leads to the possibility that the slight misalignment between small numbers of crystal layers with metal spheres has an effect on transmission.

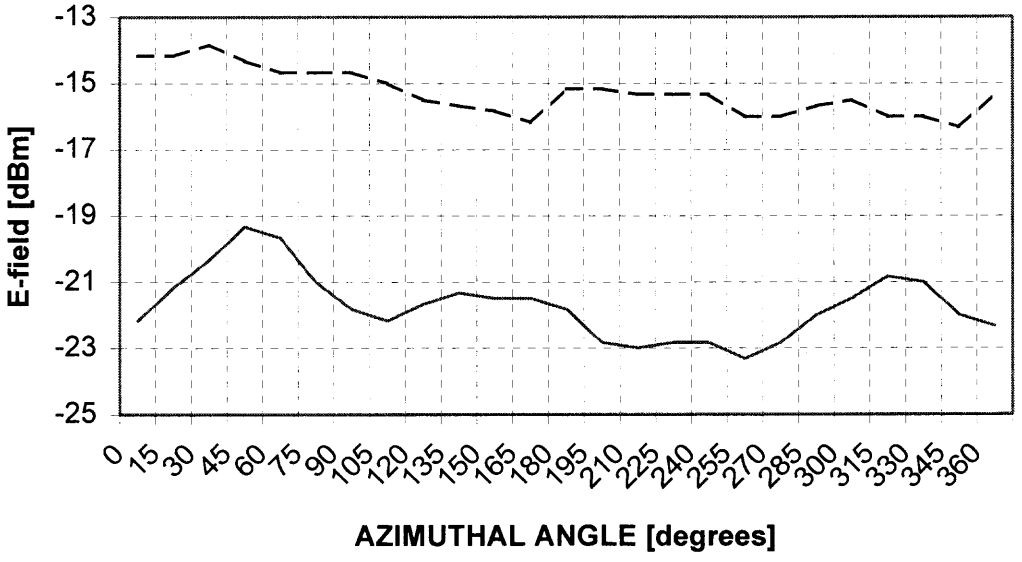

Figure 6.10 Comparison of 15 GHz, 4-layer results for pure dielectric (polypropylene, dotted line) and hybrid crystal.

In the stacking of these crystals, the 'B' layer of the fcc lattice was used for the minority steel spheres. This was an intentional measure to ensure alignment of the spheres through the depth of the crystal as much as possible. It can also be postulated that the number of complete crystal periods also has an effect. The artifact is observed at nine layers, which does represent three complete crystal periods in the direction of propagation. Note that the artifact is not present in the 15 GHz results, thus it is expected that it is a wavelength dependent phenomena. An immediate observation is the difference in wavelength of the incident beam compared to the crystal period between metal and pure dielectric layers. At four layers, the incident beam variation between 10 GHz and 15 GHz ($\lambda \approx 18$ mm) approaches matching the period of the metallic minority sphere period in the crystal ($\Lambda_{metal} \approx 16$ mm). This approach leads into nearly infinite possibilities of arrangement of minority conductive elements in three-dimensions for spectral filtering.

Although azimuthal variation filtering is more effective at higher frequencies due to the matching conditions for the surface plasmon wavevector, note that changing the frequency changes the azimuthal location of relative stop and pass bands. For example, see Figures 6.7a and 6.9a, specifically the nine-layer results. In Figure 6.7a (5 GHz), there is a maxima at $\phi = 180°$ while in Figure 6.9a (15 GHz) a minima is at the same position. Although this may be construed from the expression for the surface plasmon wavevector, $k_{sp} = k_y \pm nG_y \pm mG_z$, note that this expression is formulated for a general square array. In the case of these experiments, there is periodic square array in the direction of propagation as well. Thus, the differences in transmission point to coupling between the elements, or to an effect on the coupling of the propagating modes in the

dielectric. As such, it is possible that a Fabry-Perot standing wave is set up between layers, affecting the transmission through coupling with the propagating beam. To reinforce this possibility, note the position of the minima at $\phi \approx 180°$ and that the wavelength nearly matches the Λ_{metal}, (minority metal sphere period). Formation of this standing wave would vary with azimuthal crystal orientation with respect to beam polarization due to the surface plasmon wavevector relationship.

6.9 Conclusions

Transmission through the metal-dielectric crystal is dependent upon azimuthal orientation, frequency, thickness and upon the patterning of the metal features. Thus it may be possible to construct devices for polarization or wavelength division filtering once a structure is completely characterized.

The modification of the permittivity and consequently the self-imaging distance in three-dimensional photonic crystals by the introduction of metal elements was demonstrated. Results of this are consistent with the pure dielectric case. Lower than expected interpeak loss through the range of the crystal, comparable to the pure dielectric media, suggests low attenuation making this type of crystal viable for applications. Further, by demonstrating the selectivity of the crystal azimuthal morphology as a function of thickness and frequency, polarization selective filtering is possible.

A major finding is that selectivity of crystal azimuthal morphology reinforces the significant role of modification of the transverse wavevector in affecting crystal transmissivity. This finding provides significant insight toward development of photon crystalline optical principles. Since the modification of the transverse wavevector is

related to the photonic band gap, the technique of dispersal or patterning of negative permittivity elements may lead to novel ways to engineer the band gaps. Changing the slope or location of the band gap could result in the realization of novel optical devices. Lastly, recall that modification or attenuation of the transverse wavevector was a primary feature of the transverse Bragg waveguide. This feature can be combined with the concept of a defect mode, that is, an intentional perturbation to change the density of states of the propagating modes.

CHAPTER 7

INVESTIGATION OF DEFECT MODES IN FCC CRYSTAL

7.1 Introduction

One of the effects of the photonic crystal on radiation is photon localization. In 1987, John conjectured that an analogous effect to electron localization could exist in photonic crystals[25], based on Yablonovitch's predictions of the inhibition of spontaneous emission[23].

Since then, the primary emphasis in photonic crystal is the identification and characterization of photonic bandgaps. Propagation of radiation is prohibited in the electromagnetic bandgaps in photonic crystal, at least for selected crystal directions. The existence of a band gap is useful and is proposed for the construction of lossless mirror, resonant cavities and so on[36]. Localization occurs when a property is introduced into the crystal that allows the existence of an eigenmode for propagation within a bandgap. One technique of doing this is to introduce a void, or gap into the photonic crystal. Such an introduction is called a *defect mode* implying there is an irregularity in the crystal along which radiation can propagate in permitted modes. An analogy to this is the transverse Bragg waveguide, already discussed. The periodic media on one or both sides of a guiding region attenuate the transverse wavevector. In this context, the periodic media in a photonic crystal affect the transverse wavevector propagation while the defect modifies, or permits propagation in a particular direction.

Defect modes have been demonstrated by numerical simulation. Mekis details a numerical method that simulates defect mode transmission through a one-dimensional

slice of two-dimensional photonic crystal. In this work, propagation is calculated to occur in a physical gap in a direction of the two-dimensional crystal where there is a photonic band gap. Nearly lossless transmission is supported through the physical gap turning very sharp bends[26]. In standard waveguides or optical fiber, the bend radius must greatly exceed the wavelength of the radiation, otherwise light leaves the waveguide. The incident angle upon such a bend would not support total internal reflection and the radiation would leave the guide. On the other hand, a metallic guide would also direct the radiation, but with significant loss.

With this background the introduction of linear voids in the fcc crystals under investigation is explored. Characterization of the fcc system for defect modes would be particularly useful toward realization of microwave and optical devices. By extension of the experimental work already done, an attempt to identify simple defect modes in the crystal can be made.

7.2 Experimental Setup

For this phase of the experiment, crystal assemblies identical to the other experiments are used. Input powers to the crystals were the same in all of the experiments, with some exception where noted. Concentration is placed on the use of polypropylene and polypropylene-metal crystals. These particular crystals are relatively well characterized by the previous experiments and show lossy characteristics at f = 10 GHz. It is not expected that this crystal will demonstrate a photonic bandgap since Yablonovitch demonstrated that is it unlikely that a close-packed fcc crystal, especially one of relatively

low index contrast will possess a band gap[21]. Thus, experimental data already determined is relied upon to determine a situation that frustrates propagation.

Figure 7.1 illustrates the introduction of the void for the polypropylene crystal. The material is transparent to microwave radiation. While the size of the void is quite small compared to the wavelength at 5 GHz, the size becomes comparable at 15 GHz. The photograph shows the cylindrical spacer just below the center of the crystal face, but within the resolution of the detector. This spacer holds the spheres to construct a void somewhat larger than the diameter of the cylindrical tube. It was difficult to preserve the stacking order of the fcc crystal and introduce the void, some dislocations of spheres can be noticed at the periphery of the crystal. However, it is expected that edge effects will not contribute greatly. The general procedure of the experiment was to take a measurement at each sector of the crystal face, illustrated in Figure 7.1. Measurement of individual sectors was performed for each crystal layer. Each sector is the size of the cross-section of the detector, thus a high-resolution field map is not possible. Despite this lack of fine resolution it will be possible to gain enough information to detect differences in power distribution across the crystal face as well as to make comparisons to the bulk polypropylene and polypropylene-metal crystals.

7.3 Results

The 5 GHz results for the polypropylene with void resemble the bulk crystal, with three significant differences. First, there is a significant power offset for the void results. Power transmitted through the crystal with void is higher through all layers, with little

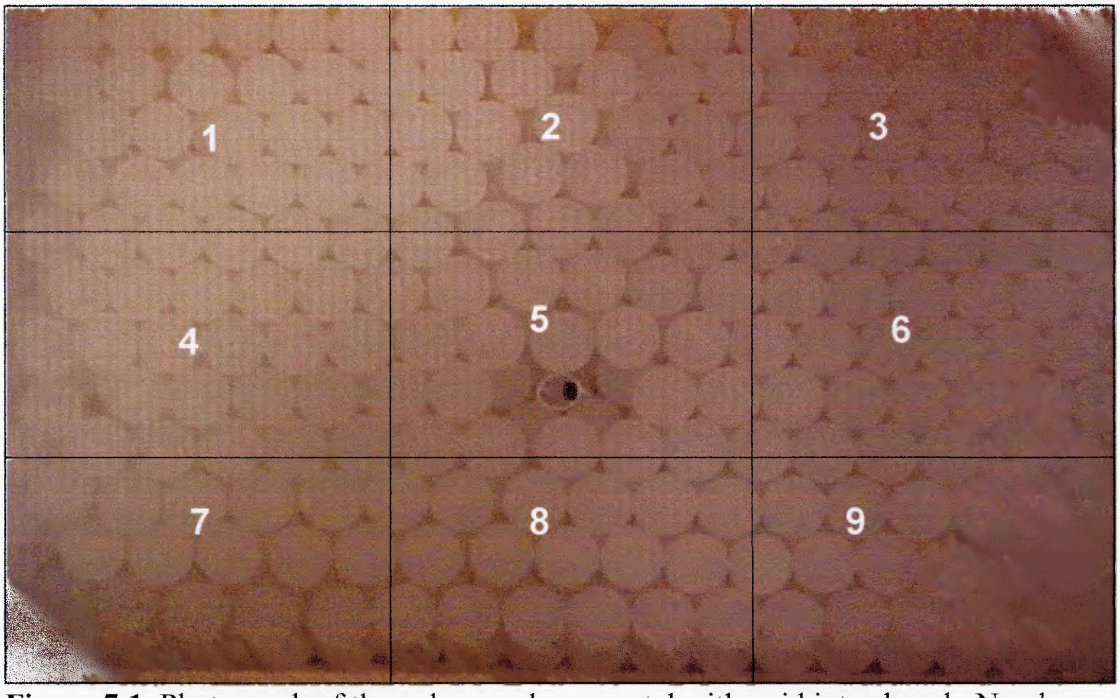

Figure 7.1 Photograph of the polypropylene crystal with void introduced. Numbers represent sectors of the crystal face used in measurement. Beam propagation is out of the page. The transmitting antenna is on crystal lower face, opposite sector 5.

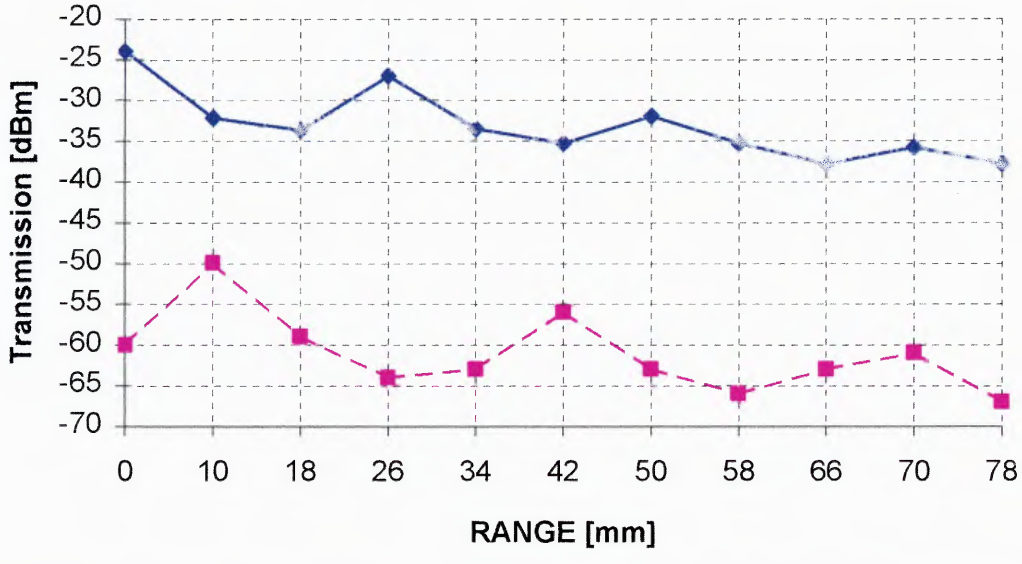

Figure 7.2a Transmission through successive crystal layers, bulk polypropylene (dashed line) and polypropylene with void near center, d_{sphere} = 10 mm, f = 5 GHz.

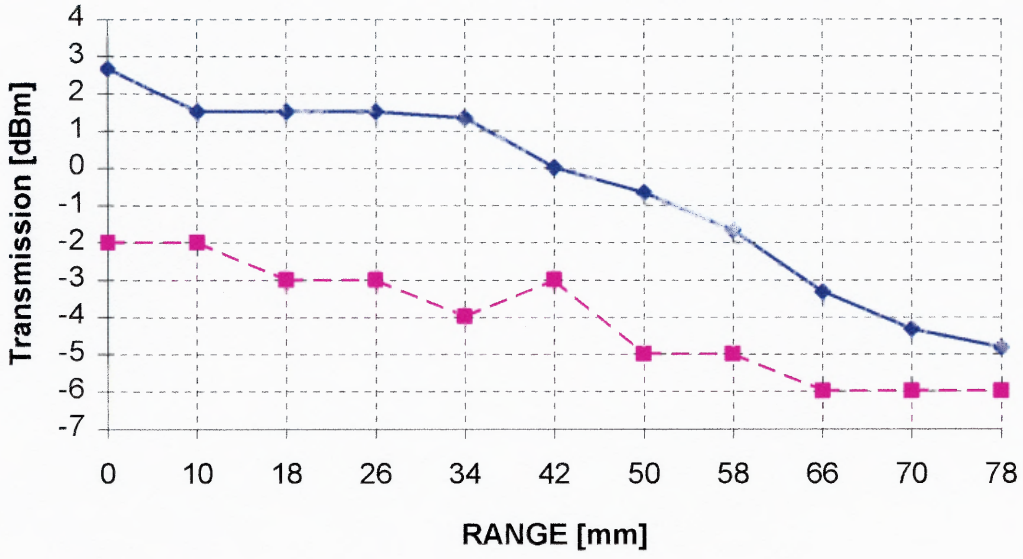

Figure 7.2b Transmission through successive crystal layers, bulk polypropylene (dashed line) and polypropylene with void near center, d_{sphere} = 10 mm, f = 10 GHz.

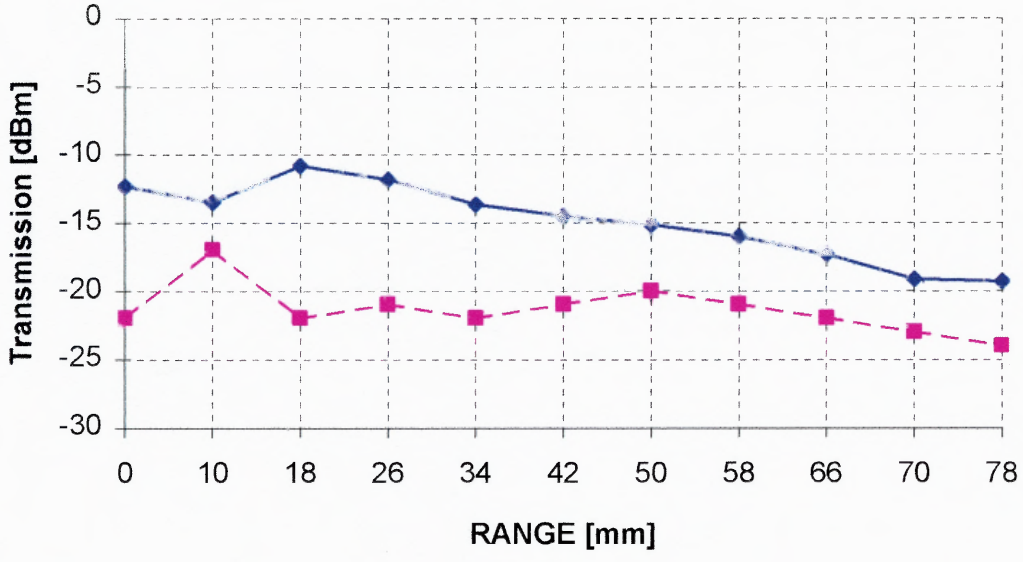

Figure 7.2c Transmission through successive crystal layers, bulk polypropylene (dashed line) and polypropylene with void near center, d_{sphere} = 10 mm, f = 15 GHz.

loss. In this case, it is suspected that this difference is due to an input power mismatch between trials, since the zero layer result should be nearly the same for each of the plots in Figure 7.2a-c. Despite this unknown, the qualitative nature of the result remains useful. Imaging occurs as in the bulk result, which leads to the second difference. The self-imaging distance has decreased in the crystal with void. Lastly, the crystal with the void has the interval of the maxima shifted. The initial maxima occurs at x = 0, unlike the results for the bulk crystal where the initial maxima occurs at x = 10 mm. At 10 GHz, the same structure again yields a surprise. It is expected that it is more likely that a propagation mode will exist as the wavelength becomes closer to the void size. Yet in the 10 GHz case, the loss is actually greater than in the bulk crystal over an equivalent range. Initially, the transmission is higher, possibly indicating propagation in the void but by the tenth layer, the output is within 1 dBm of the bulk crystal. Effect of the void is pronounced at 15 GHz also. Initially, the transmission through the crystal with void shows a flat response, compared to the bulk crystal.

7.4 Discussion

Without zero-layer matching input powers in the 5 GHz result, only conjecture is possible about any localization in the void. At the outset, it seemed that localization might have been occurring in the void, with the modes excited outside the waveguide superimposing the self-imaging maxima onto the localized modes. Note that the magnitude of the maxima in the crystal with void is slightly less than those in the bulk crystal, supporting this theory. Unfortunately, the zero-layer power mismatch renders this conclusion as questionable. There is, however, no error in the observation of the change in the self-

imaging distance. The same void at 10 GHz appears to retard propagation more than the bulk crystal. At 15 GHz, the trends between void crystal and bulk are similar, yet there remains an offset.

Although this segment of the characterization of the fcc photonic crystal may seem less than conclusive it is possible to assume that, especially in the case of the void crystal at 10 GHz (Figure 7.2a), that energy is coupling out of the central portion of the crystal. To further investigate this line of thought, a void was placed off-center in the crystal to determine if modes could be coupled through the bulk crystal into an off-center void. While unsuccessful in demonstrating the coupling, this effort led to the observation of propagation through other directions in the fcc polypropylene crystal.

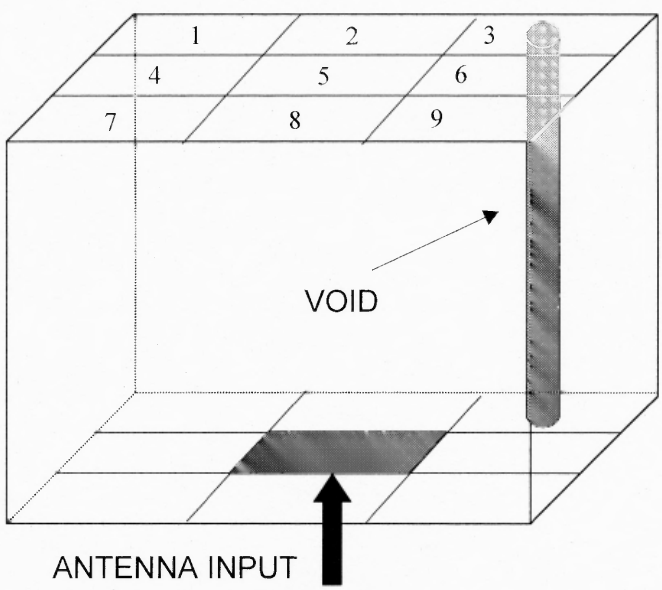

Figure 7.3 Repositioning of the void off-center in the photonic crystal. Spherical media fill is omitted for clarity.

Figure 7.4 shows propagation as a function of crystal layers measured in crystal position #1 (see Figure 7.1 for the detector positions). In this particular experimental trial, a void was introduced into crystal sector #3, so the propagation measured in position

#1 was entirely through bulk polypropylene crystal. The microwave beam was launched at the center of a {111} crystal face (as noted in Figure 7.3). Distinct self-imaging is noted as well as an increase in the measured power. This is not an instrumentation artifact, similar behavior was observed in the complimentary detector positions #3, #7 and #9. The introduction of the void in position #3 did not greatly affect the imaging pattern, consistent with the observations from the introduction of the void into crystal center, at position #5. These patterns were also highly reproducible in the center-void crystal at the same (corner) positions. The detector position corresponds generally to a <110> crystal direction, however, it is not possible to verify this exactly due to the detector size. Note that other crystallographic directions are contained within the area of the detector. Despite this, some conjecture can be made about this result.

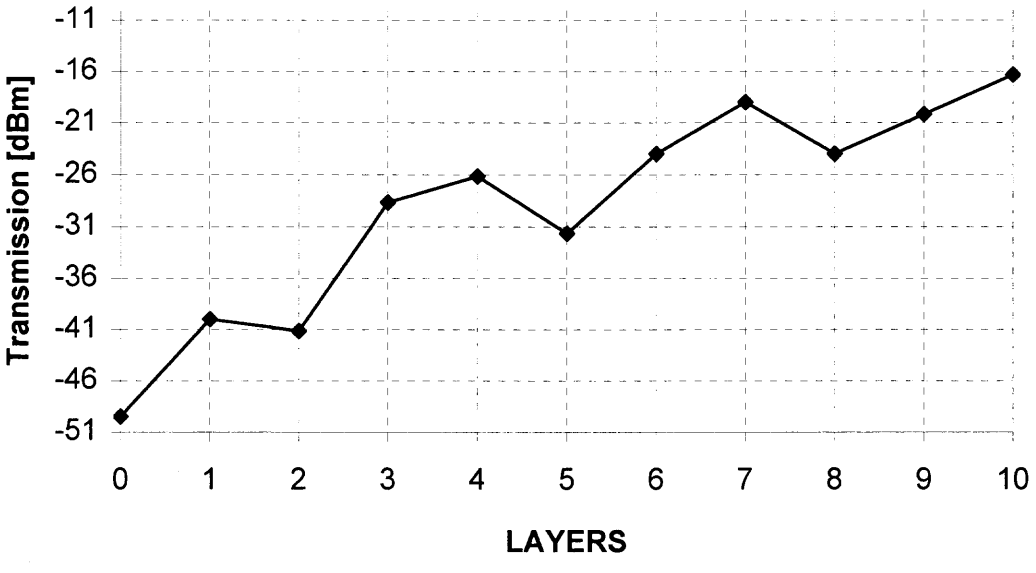

Figure 7.4 Propagation at 10 GHz measured in position 1, polypropylene crystal with void at position 3.

At 10 GHz, the center measurement as a function of layers shows more loss overall than the pure dielectric crystal. It can be concluded that loss from the center is coupling into modes propagating in the general <110> crystal direction. As power is lost from the center mode, it is transferred into the modes in the <110> directions. At the same time, the Bragg condition is fulfilled by the {110} planes. Recall that prohibition of transverse wavevector propagation[32] occurs when $k_x = k_0 n_{eff} \sin(\theta) = q\pi/\Lambda$, where q = 1/2, 1, 2 ,3..., where Λ is the structure pitch and n_{eff} = 1.369. It is also possible that $k_0 n_{eff} \sin(\theta) = q\pi/\sqrt{2}\Lambda$, recalling the spacing of Λ_{metal} with respect to the azimuthal crystal orientation. Using this relationship, it is possible to calculate approximate values of θ = 30°, 43° and 64° at f=10 GHz, for Λ = 10 mm, q=1 and q=1.5. These angles correspond roughly to the angle between the (111) plane which is the incident plane and the (311) or (100), (310) and (211) crystallographic planes, respectively. The detector cannot discriminate angles much smaller than 30 ° or 40° given the size of this crystal. So it is likely that the transverse Bragg condition for propagation is prohibited or modified within this range of angles in the crystal, resulting in the observed self-imaging.

The experimental observation of redirected self-imaging also confirms the prediction of ultrarefraction and beam splitting in photonic crystal[33]. Moreover, it has been demonstrated in three dimensions by these experiments, representing an experimental first in the field. Although the initial exploration of propagating defect modes in the fcc crystal met with limited success, this line of inquiry is continued for completeness. The next step in the exploration of defect modes in the crystal is to attempt redirection through the crystal through the defect mode.

7.5 Redirection Through Defect Mode

A new experiment was devised where a field map was constructed of the five non-incident crystal boundaries for ten-layer fcc crystals comprised of d_{sphere} = 10 mm polypropylene spheres, and a polypropylene/metal hybrid crystal. In this experiment a 90° void was introduced into the crystal, as illustrated in Figure 7.5. The void began on the incident face and continued along the incident beam direction until the fifth layer where it was redirected 90° to the side of the crystal, toward position A. Measurements of the output microwave radiation with the detector polarization oriented vertically and horizontally on selected side crystal faces were undertaken.

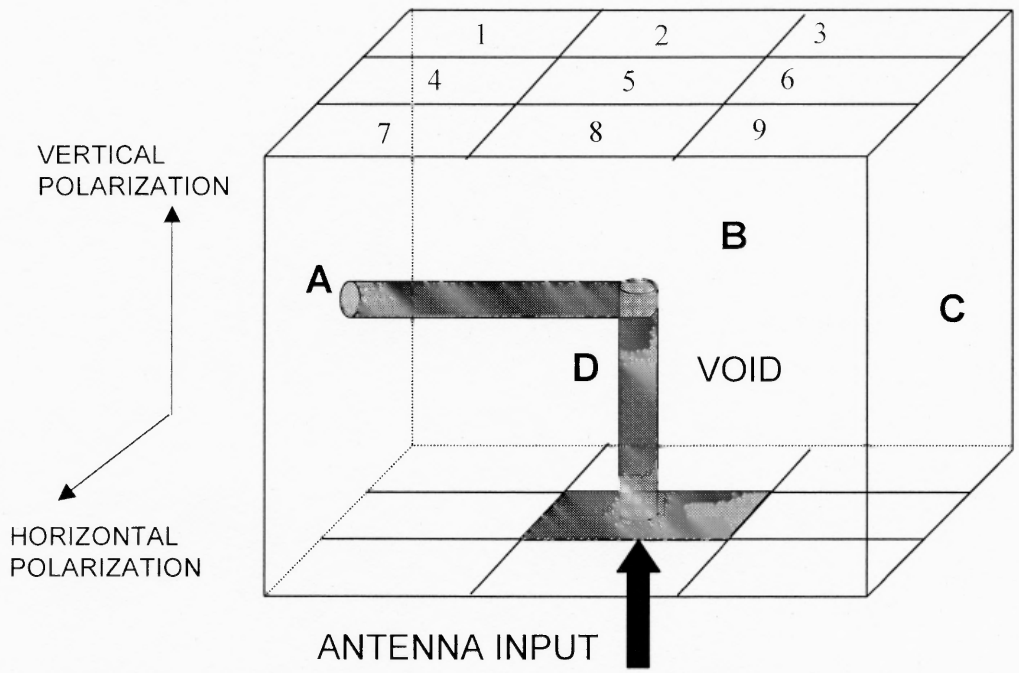

Figure 7.5 Introduction of a 90° void into the 10-layer crystal (spherical media omitted for clarity). A, B, C and D positions are on the side faces (center) of the crystal. Positions 1-9 are on the upper crystal face. Receiving antenna polarization with respect to the A, B, C and D is noted.

7.6 Redirection Results and Discussion

From the mapping effort, it is possible to examine redirection of energy at 90° through the introduced defect mode. Table 7.1 enumerates the results. Very significant power differences are noted at 10 GHz between results for the bulk polypropylene crystal (with and without void) and the polypropylene/metal hybrid. In general, power output at position A is highest for metal hybrid crystal, less for bulk polypropylene with void and small for bulk crystal. This is visualized by the plot at Figure 7.6. Since birefringence is not expected, the polarization of the redirected beam will be horizontal at positions A and D, but vertical at position D. This is accompanied by a loss of throughput power at 10 GHz for the on-axis (center) measurement. For the polypropylene crystal with void, the throughput at center is approximately 6 dBm less than the same crystal without a void.

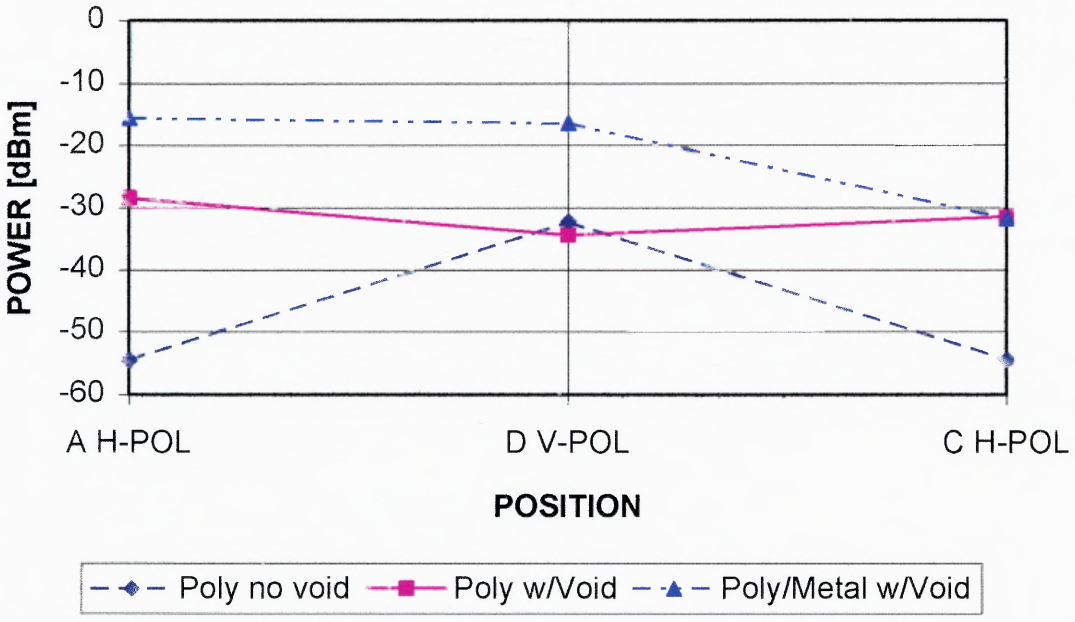

Figure 7.6 Power throughput at side crystal faces A, D and C at noted polarization. The void output is at position A.

Comparison of the polypropylene/metal with void shows 9 dBm less center throughput than the bulk crystal. Comparing the horizontal polarization measurements at positions A and C, at 10 GHz, it can be concluded that there is redirection of energy along the void. A difference of approximately 16 dBm is noted for the polypropylene/metal crystal with void between the A and C positions (horizontal polarization). Yet, a difference in throughput of only 3 dBm is noted in the polypropylene-only crystal with void. Horizontal polarization measurement is consistent with the polarization of the input mode and minimal birefringence. The output at position D is also noteworthy. No void is installed at position D, yet a large throughput difference is noted there when compared to both the polypropylene cases. These two observations point to wide redirection of the propagating beam in absence of the void. Numerical predictions assert that this is possible in close-packed fcc crystal systems[33]. The effect is also observed in the hybrid metal crystal. The redirection of the beam is far from lossless in this media, however. Consider also that the size of the transmitter (identical to the detector) made it impossible to confine the input beam to the void. Therefore other modes will always be present, as well as energy scattered in the case of the crystal faces parallel to the crystal x-axis.

7.7 Redirection Conclusions

Summarizing the experimental findings:

1) Redirection along the 90° void is occurring for the hybrid dielectric/metal crystal.

2) Significant energy leaves the crystal through the D-side.

Table 7.1 Void measurement results, polypropylene and poly/metal

Vertical polarization, position A			
f [GHz]	NO VOID (Poly Only)	VOID (Poly & Metal)	VOID (Poly Only)
5	-57.67	-63.50	-63.17
10	-44.33	-39.33	-46.17
15	-42.17	-38.83	-48.17

Horizontal polarization, position A			
f [GHz]	NO VOID (Poly Only)	VOID (Poly & Metal)	VOID (Poly Only)
5	-51.00	-50.67	-49.17
10	-54.50	-15.67	-28.50
15	-42.67	-37.00	-33.67

Vertical polarization, position C			
f [GHz]	NO VOID (Poly Only)	VOID (Poly & Metal)	VOID (Poly Only)
5	-57.67	-59.33	-56.67
10	-44.33	-34.17	-40.50
15	-42.17	-37.17	-49.50

Horizontal polarization, position C			
f [GHz]	NO VOID (Poly Only)	VOID (Poly & Metal)	VOID (Poly Only)
5	-57.67	-51.67	-50.33
10	-54.50	-31.83	-31.50
15	-42.67	-37.00	-41.33

Vertical polarization, position D			
f [GHz]	NO VOID (Poly Only)	VOID (Poly & Metal,)	VOID (Poly Only)
5	-43.33	-42.33	-43.50
10	-32.33	-16.50	-34.50
15	-49.67	-43.83	-45.67

Horizontal polarization, position D			
f [GHz]	NO VOID (Poly only)	VOID (Poly & Metal)	VOID (Poly Only)
5	-63.50	-56.83	-65.00
10	-41.50	-34.17	-41.33
15	-42.67	-31.00	-41.50

Parallel to transmitter polarization, Position 5			
f [GHz]	NO VOID (Poly only)	VOID (Poly & Metal)	VOID (Poly Only)
5	-36.67	-37.83	-40.33
10	- 0.33	-9.00	-6.33
15	-17.17	-21.50	-23.67

From this segment of the experiment it is concluded that propagation can be enhanced by the inclusion of defects in the fcc crystal. Due to the lack of a complete bandgap, at least in the crystal directions examined, the redirection of energy is not nearly lossless. However, the phenomena is frequency-selective and may be useful for device realizations. Another conclusion is that redirection of the energy may also be occurring due to ultrarefraction without influence of the void defect, evidenced by the position D measurements in the polypropylene/metal hybrid crystal. Thus, the polypropylene/metal crystal will be examined in more detail.

7.8 Evidence of Ultrarefraction in the Polypropylene/Metal Hybrid Photonic Crystal

Seeking the presence of defect modes in the hybrid crystal yielded strong evidence for ultrarefractive behavior, illustrated in Figure 7.4. To this end, a complete field map of all five non-incident sides of a solid hybrid metal crystal was constructed. Templates on each side of a microwave-transparent box were setup for the detector in both vertical and horizontal polarizations. Measurements for eight and ten-layer crystals were conducted with the beam input at the center of a (111) crystal plane. The criteria for ultrarefractivity is the presence of a power measurement within 6 dBm of the center output face power measurement.

7.8.1 Results of Field Mapping

Enumeration of the field maps for selected polarizations is given in Tables 7.2 and 7.3. The positions of the numerical results in the table reflect their position on that particular crystal face. In the experiments with crystal voids significant transmission was noted on

Table 7.2 Field maps for the B and D crystal sides, all values in dBm.

Side B (Metal & PP Solid ,10 LAYERS) – Vertical Polarization:

5: -52.67 10: -28.17 15: -35.83	5: -46.17 10: -15.17 15: -50.83		5: -46.83 10: -17.17 15: -44.17	5: -54.33 10: -34.17 15: -40.33
		5: -42.33 10: -20.00 15: -31.17		
5: -55.83 10: -27.83 15: -37.83	5: -44.83 10: -17.50 15: -44.83		5: -45.67 10: -16.17 15: -36.17	5: -53.33 10: -34.67 15: -47.67

Position 5 (top center) 5: -37.85 10: -9.00 15: -21.50

Side D (Metal & PP Solid ,10 LAYERS) – Vertical Polarization:

5: -66.00 10: -37.67 15: -32.83	5: -46.50 10: -22.33 15: -34.17		5: -46.50 10: -28.83 15: -36.67	5: -64.50 10: -27.17 15: -47.50
		5: -42.50 10: -24.83 15: -26.67		
5: -51.50 10: -32.50 15: -32.17	5: -42.17 10: -12.17 15: -32.50		5: -43.33 10: -15.83 15: -30.00	5: -62.50 10: -28.33 15: -40.00

Position 5 (top center) 5: -37.85 10: -9.00 15: -21.50

the D-side center. Field mapping of this side and the complimentary B-side in hybrid bulk crystal reveals less significant power being directed to these positions at 10 GHz (-10 dBm), compared to throughput noted in the crystal with the void. In comparison, the top crystal face power (at center, position #5) is –10.33 dBm. On the B-side for vertical polarization, sectors surrounding the face center show significant power throughput (-15 to -17 dBm). These values are underlined as a guide to the eye. In addition, the power just below and left of center on the D-side for vertical polarization is -12 dBm, also underlined. The power at the complimentary position to the right is only a little lower, at –15.83 dBm. Since these are at acute angles to the incident beam, it may be a reflection from a crystal plane.

Consider that the size of the detector resulted in some overlap of these measurements, so it is possible that the beam is being redirected through some solid angle, generally perpendicular to the crystal center axis. This behavior is not entirely

Table 7.3 Field maps for the A and C crystal sides, all values in dBm.

Side A (Metal & PP Solid ,10 LAYERS) – Horizontal Polarization:

5: -53.00 10: -42.17 15: -33.33	5: -67.33 10: -23.67 15: -32.00		5: -54.83 10: -21.50 15: -43.17	5: -52.17 10: -29.00 15: -28.33
		5: -50.17 10: -19.67 15: -28.83		
5: -55.33 10: -39.67 15: -43.33	5: -50.00 10: -15.83 15: -33.00		5: -48.17 10: -14.83 15: -37.67	5: -57.67 10: -30.00 15: -29.17

Position 5 (top center) 5: -37.85 10: -9.00 15: -21.50

Side C (Metal & PP Solid ,10 LAYERS) – Horizontal Polarization:

5: -51.17 10: -38.50 15: -32.33	5: -57.17 10: -20.00 15: -32.67		5: -54.50 10: -24.67 15: -37.83	5: -53.67 10: -22.67 15: -31.33
		5: -52.33 10: -13.83 15: -40.67		
5: -61.00 10: -22.83 15: -37.00	5: -61.83 10: -17.83 15: -50.17		5: -54.83 10: -19.00 15: -34.33	5: -53.83 10: -27.00 15: -47.67

Position 5 (top center) 5: -37.85 10: -9.00 15: -21.50

unexpected, since some predictions based on numerical results have been made concerning redirection in opaline three-dimensional photonic crystals. Predictions have the beam redirected through large azimuthal and transmitted angles compared to the incident angle[33]. This experiment provides experimental confirmation of the phenomena in three-dimensional crystals. In addition, the results of azimuthal and incident morphology provide a reciprocal confirmation of the numerical predictions. Comparison

of the A and C-sides at horizontal polarization confirm the redirection of the beam, particularly to the C-side (center value of –13.83 dBm, underlined compared to the –9.00 dBm value at the top of the crystal at position #5). Again evidence of reflection, or possibly obtuse beam redirection, in solid dielectric/metal crystal is observed.

7.9 Conclusions Regards Ultrarefractivity

The results qualitatively suggest ultrarefractivity since significant, although lossy, redirection of the beam is taking place through 90° without the presence of a void. Since the detector size is large compared to the crystal face, exact determination of the angle from the incident beam is not possible making comparisons to particular crystal planes difficult. Yet, there is a consistency in the results since the crystal side sectors exhibiting the higher power transmission may be in similar crystal planes to the observations of Figure 7.4. It is difficult to express observations on the transverse wavevector propagation for the crystal side sector results, since it was not possible to examine the propagation through the crystal layer by layer, as can be done with the top face. Despite these difficulties, beam splitting and ultrarefractivity is demonstrated in the three-dimensional metal/dielectric crystal system. Of course, the frequency selection, dielectric contrast, minority metal sphere pattern are all variables that have not been explored in detail.

CHAPTER 8

CONCLUSIONS

8.1 Contributions

In this dissertation, the characteristics of three-dimensional face center cubic (fcc) photonic crystals were explored as self-imaging components and as polarization and frequency selective components. The experimental work performed represents a first detailed examination of the fcc photonic crystal system, in particular for it's optical properties.

The experimental characterization advances work started in 1836, by F. Talbot and his initial observations of self-imaging. Photonic crystals studied in the experiments presented here show some analogous behavior to the self-imaging developed from Talbot's work. In addition, a short-range imaging effect, where the images form at intervals shorter than the beam wavelength caused by propagation through media of features smaller than the beam wavelength, was also identified. Such a phenomena was not predicted by Talbot or Rayleigh, since it is below the Fraunhofer diffraction limit. Dependence of the self-imaging phenomena was correlated to frequency, polarization, dielectric contrast and feature size. The mechanisms of transverse wavevector frustration and ultrarefractivity are proposed as the causative factors for these phenomena. Work performed in this dissertation experimentally confirms several numerical studies of predicted optical effects in photonic crystals. Further, it demonstrates a three dimensional analogue to behavior observed in photonic crystals of less than three dimensions.

In addition, frequency selectivity and polarization selectivity was demonstrated as a function of crystal morphology. The bulk of photonic crystal work performed to date concentrates on the identification of a photonic band gap as a function of crystal morphology, whereas this study concentrates on the transmission characteristics. The results provide evidence for some predicted effects from numerical work and identify significant new findings that arise from the use of small crystals that are a few wavelengths of the incident radiation in overall dimension. One result is the dependence on azimuthal morphology matching of crystalline planes. Frustration of the transverse wavevector, as in a transverse Bragg waveguide, is explored as an explanation for the incident morphology's effect on transmissivity of the crystal.

Throughout this effort, simulations based on finite element solving of Maxwell's equations were used to guide the development of experiments. In doing so, the utility and limitations of these simulations were identified. It was also found out quite early in the effort that classical expectations based on diffraction left much to be desired in predicting the behavior of these systems and that other analytical methods were intractable. Overall, it was found that electromagnetic simulations in common use cannot fully characterize this photonic crystal system, in particular, the polarization dependencies. Moreover, inconsistencies between simulations used to determine band gaps in generalized photonic crystal and the experimental realities of finite photonic crystals have been identified.

Efforts led to novel experimentation with elements of negative permittivity in the photonic crystal in an attempt to engineer the effective index of refraction, modify the dispersion relation and/or enhance the formation of surface plasmons. Effects were

examined in terms of self-imaging and azimuthal morphology. These effects were correlated to the dielectric contrast and frequency and matching of surface plasmon wavevectors. It was demonstrated that addition of these elements provides an additional means to control the propagation of radiation through the crystal. Lower than expected losses in propagation through the metal/dielectric hybrid also demonstrate it's usefulness as an optical component.

Led on by analogous behavior predicted in two-dimensional systems, propagation along void defects in the pure dielectric and metal/dielectric hybrid crystal was investigated. While significant evidence for defect mode propagation was found, it is recognized as being far from efficient and needs optimization. With the knowledge of theoretical correlation of negative permittivity at the edge of photonic band gaps with ultrarefractivity, the crystal was examined for ultrarefractive effects. Pursuing evidence of defect modes led to the discovery of self-imaging ultrarefractivity in the metal/dielectric hybrid photonic crystal. Unfortunately it was not possible to correlate the ultrarefractivity to the dispersion relation since known models were suspect due to the finiteness of the crystal and the resolution of the detectors. In the particular case observed, however, energy lost to the center of the structure was coupled into a series of images of increasing intensity along another crystal direction. This is the first known report of beam splitting self-imaging ultrarefractivity in photonic crystal and may be a particular consequence of the addition of elements of negative permittivity. Further, reciprocity is suggested by the results, where beams can be redirected and filtered through solid angles of the photonic crystal media.

Overall, the fcc opaline crystal system, thought not to possess great usefulness due to the lack of complete photonic band gaps (e.g., band gaps in all crystal directions) has been demonstrated to have novel, interesting and possibly useful transmission properties than can ultimately be characterized and controlled.

8.2 Applications

Several applications of these properties of the fcc opaline photonic crystal come to mind. First, a frequency selective imager or filter can be envisioned. Beams of different frequency can be input into the crystal and be redirected or imaged at various crystal output direction, or possibly split into several beams. Arranging detectors judiciously at these output directions may have application to optical switching, multiplexing or optical interconnection. With the short range subwavelength self-imaging effect examined, one can also envision very thin optical elements for use in detection or integrated optics applications. Another use of this may be in optical masks for microcircuit production.

8.3 Research Directions

Many possible directions for future research are possible. Ultimately, the goal is development of photonic crystal optics toward which it is hoped this experimental work is useful. Without this, researchers are confined to (what was first termed by Yablonovitch) the Edisonian experimental method adopted here. Analogous behavior in two-dimensional systems or numerical predictions was used as a guide in this exploration. In the short term, several specific topics for research for advancement in the field can be suggested.

First, advanced simulations that can accurately assess the propagation in the fcc opaline crystal structure are needed. It can be surmised that the computing power exists for such a task. To be fully functional, the simulation must account for the polarization states and the surface plasmon coupling. Simulation and numerical methods are crucial in the effort to fully characterize propagation in photonic crystal since the analytical solutions are often intractable (as in Mie scattering, with the exception of a few special cases) and the complexity of the problem is high.

Further characterization of ultrarefractivity is needed, as well. Limitations in the extent of the crystals compared to the detector sizes made the exploration of ultrarefractivity somewhat approximate. (Note that facilities and budget are a consideration in the scale of the experiment!) Two avenues to do this are open. All of the experiments performed here can be repeated in the optical regime. Or higher resolution methods can be developed to better determine the angles. While construction of optical monolayers poses a challenge, determined researchers could construct crystals of larger extent or differing scale and measure it through 4π steradians of solid angle.

Another aspect of the research that is relatively unexplored is the construction of three-dimensional metal/dielectric hybrid crystals. Design parameters used were chosen in order to preserve some predictability in the context of gratings, surface plasmons, and effective medium theories. Variation of the distribution or layering of the metal minority spheres is an obvious starting point. However, it is possible to extend analogous behavior to the large body of knowledge available concerning microwave propagation and consequently explore other possibilities. In addition, extension of the fcc crystal properties to microfabrication of pseudo-fcc opaline crystal with metal elements could be

explored. Demonstration of these effects in the optical regime would be a notable accomplishment in the field and verify the expected scalability of the crystal.

A low loss redirection of energy through the introduction of a defect mode has yet to be demonstrated in three-dimensional crystal. The information of this experimental study will provide useful insight to researchers making these attempts.

8.4 Final Remarks

In conclusion, several novel propagation effects have been identified for the fcc opaline photonic crystals. Some are surprising, while other effects were hinted at through analogous behavior observed or predicted in other crystal systems. Verification of analogous phenomena in other crystal systems is an important contribution since it will provide further study with a point of departure in the quest for cause. Armed with this new knowledge of these experimental successes and failures, it is hoped that it will provide direction and some inspiration to researchers investigating photon crystalline optics.

APPENDIX

SIMULATION OF BODY-CENTERED CUBIC CRYSTAL

Early in the conduct of the study of wave propagation in photonic crystals, body-centered cubic (bcc) crystals (Figure A.1) were subject to the same basic HPHFSS simulations as the fcc crystals. For completeness, this data is included for reference purposes.

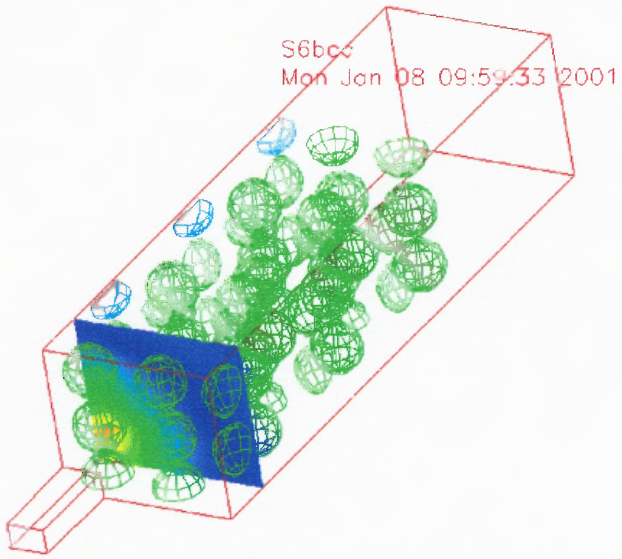

Figure A.1 Body-centered cubic simulation realized in HPHFSS. A cross-section of the electric field magnitude is depicted within the structure at a range of approximately 11 mm from the incident face of the crystal.

The material parameters of the bcc crystal were $n_{sphere} = 1.5$, $\Lambda = 1.5d_{sphere}$ and $d_{sphere} = 10$ mm. Simulations were run at frequencies of 5, 7, 10, 12, 15 and 17 GHz. A field cross-section was taken at intervals of 10 mm in the structure and the electric field magnitude values at the center of the cross-section were plotted as a function of range in Figures A.2 through A.7.

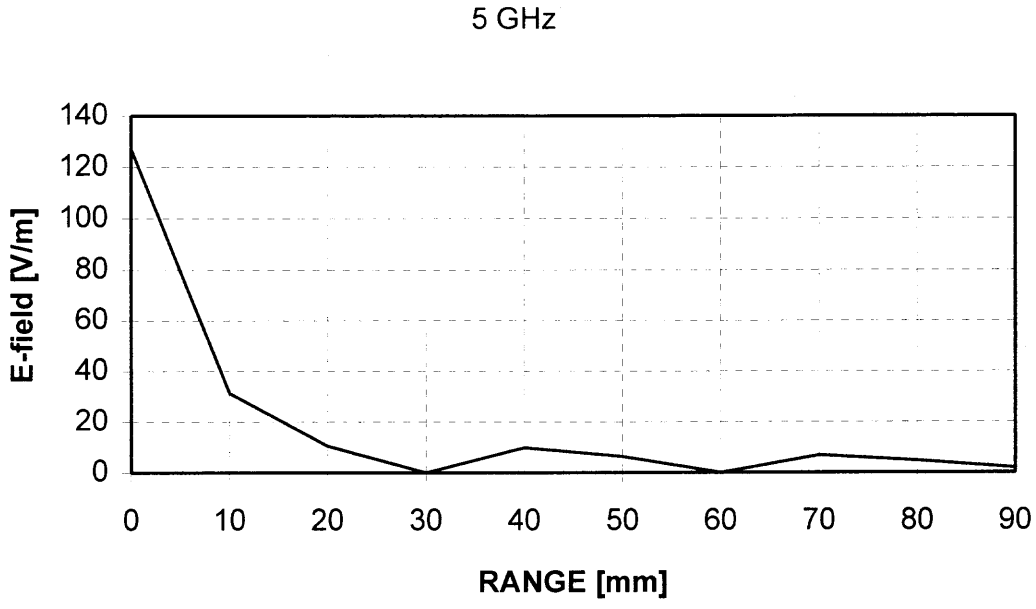

Figure A.2 HPHFSS result for transmittance as a function of range within the bcc crystal, f = 5 GHz, n_{sphere} = 1.5, 6-layer media.

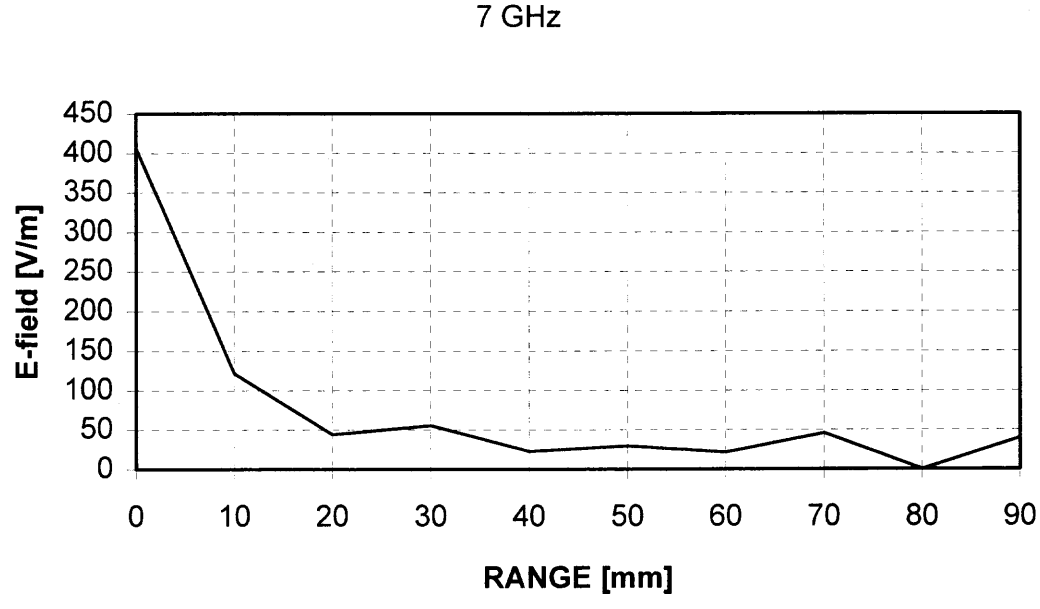

Figure A.3 HPHFSS result for transmittance as a function of range within the bcc crystal, f = 7 GHz, n_{sphere} = 1.5, 6-layer media.

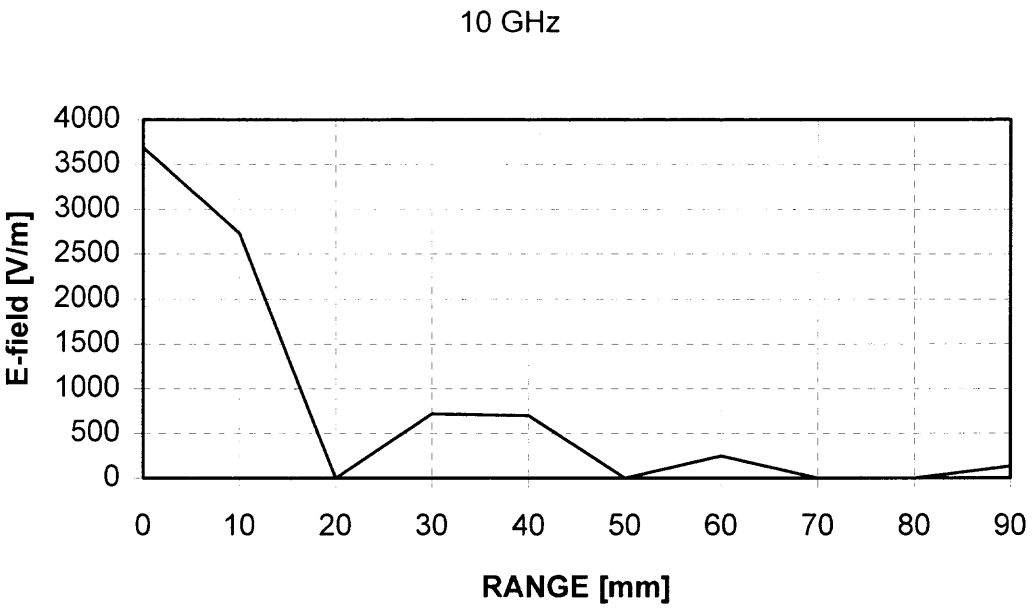

Figure A.4 HPHFSS result for transmittance as a function of range within the bcc crystal, f = 10 GHz, n_{sphere} = 1.5, 6-layer media.

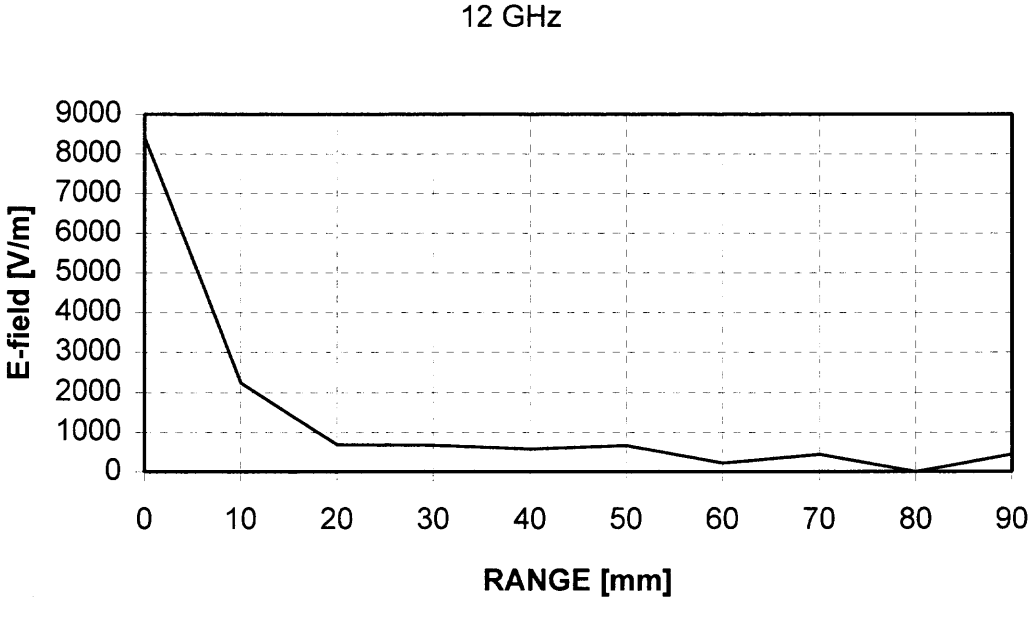

Figure A.5 HPHFSS result for transmittance as a function of range within the bcc crystal, f = 12 GHz, n_{sphere} = 1.5, 6-layer media.

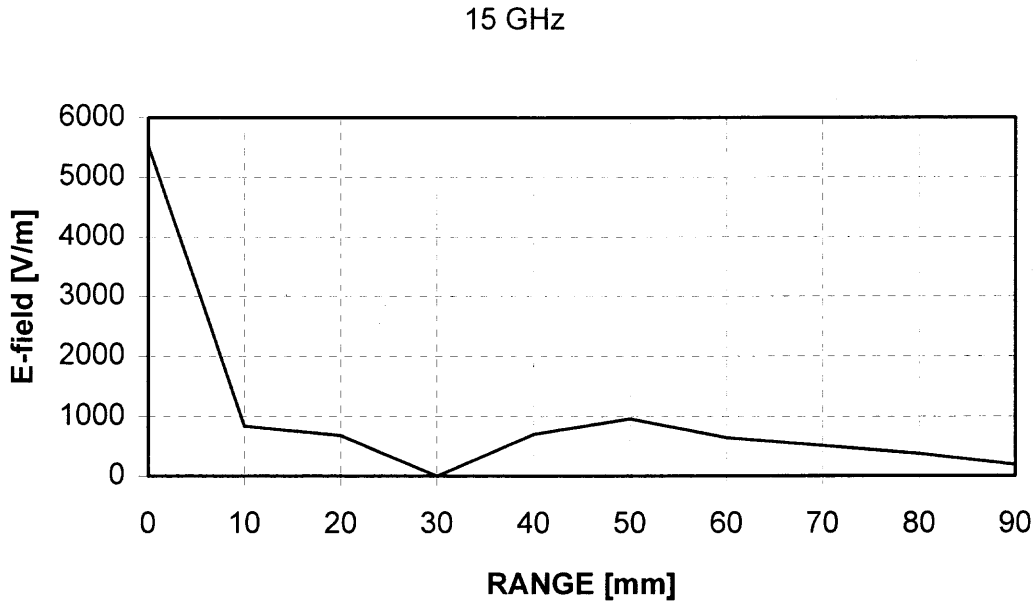

Figure A.6 HPHFSS result for transmittance as a function of range within the bcc crystal, f = 15 GHz, n_{sphere} = 1.5, 6-layer media.

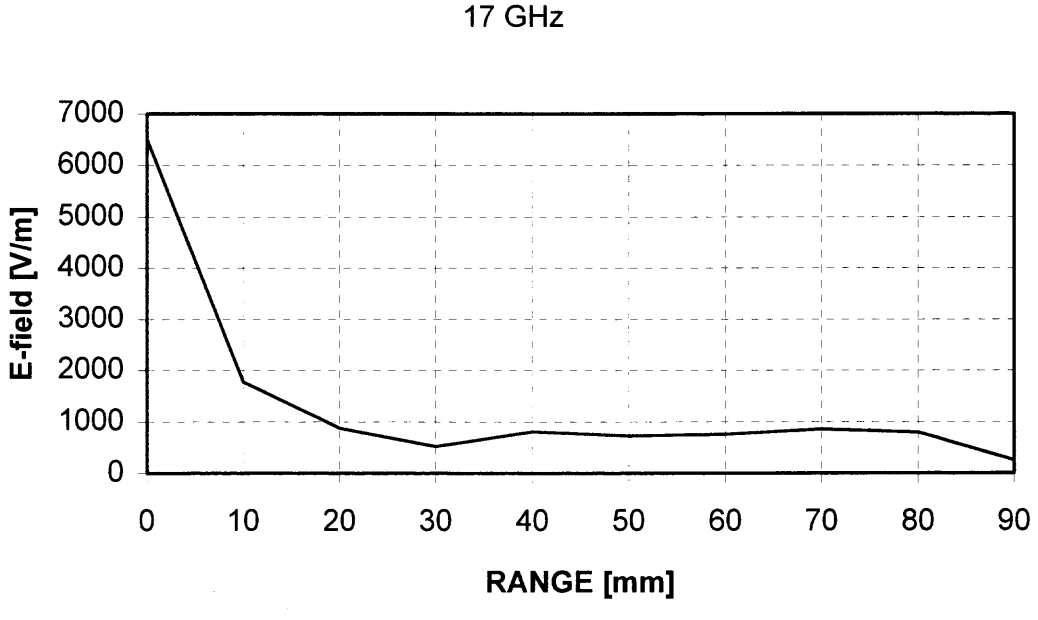

Figure A.7 HPHFSS result for transmittance as a function of range within the bcc crystal, f = 17 GHz, n_{sphere} = 1.5, 6-layer media.

Comparing these simulations to the fcc simulations of Chapter 2, one finds great similarity. Periodic maxima occur, especially at 5 and 10 GHz, generally at the same range as the fcc result. At 5 and 10 GHz, these maxima appear at Ls = 30 mm, while at the 7 GHz the maxima are less distinct and further apart. For f = 15 GHz the maxima may occur outside of the simulation bounds (assuming the media were continued) or, in other words, the Ls is larger than the structure. At f = 17 GHz, periodic behavior is not discernable.

Overall, it is reasonable to expect these similarities between the bcc crystals and fcc crystals to become manifest in physical behavior. Imaging and azimuthally dependent transmissivity can be assumed, since the {110} and {111} crystallographic planes exist in the bcc system as well as the fcc system. Note, however, that this simulation suffers the same constraints as the more detailed simulations of the fcc crystal so the similarities may become more pronounced in a close-packed system.

Although the bcc system may be of less interest in terms of device development (since the bcc system is generally more difficult to fabricate at small scales and is found less commonly in nature) it may be of greater interest as a basic science problem. Due to the lower filling fraction and simpler stacking symmetry, the bcc crystal system may be of interest for simulation or numerical method development .

REFERENCES

1. von Blaaderen, A., Ruel, R., & Wiltzius, P. (1997). Template-directed colloidal crystallization. Nature, 385, 321-324.

2. Hecht, E., & Zajac, A. (1979). Optics. Reading, Massachusetts: Addison-Wesley.

3. Petit, R. (Ed.). (1980). Electromagnetic Theory of Gratings. Berlin: Springer-Verlag.

4. Sentenac, A., Lalanne, P., & Maystre, D. (2000). Symmetry properties of the field transmitted by inductive grids. Journal of Modern Optics, 47, 2323-2333.

5. Dawes, D.H., McPherdan, R.C., & Whitbourn, L.B. (1989). Thin capacitive meshes on a dielectric boundary. Applied Optics, 28, 3498-3510.

6. Astratov, V.N., Whittaker, D.M., Culshaw, I.S., Stevenson, R.M., Skolnick, M.S., Krauss, T.F., & De La Rue, R.M. (1999). Photonic band-structure effects in the reflectivity of periodically patterned waveguides. Physical Review B, 60, R16255-R16258.

7. Ebbesen, T.W., Lezec, H.J., Ghaemi, H.F., Thio, T., & Wolff, P.A. (1998). Extraordinary optical transmission through sub-wavelength hole arrays. Nature, 391, 667-669.

8. Bomzon, Z., Biener, G., Kleiner, V., & Hasman, E. (2002). Radially and azimuthally polarized beams generated by space-variant dielectric subwavelength gratings. Optics Letters, 5, 285-287.

9. Talbot, H.F. (1836). Facts Relating to Optical Science. Philosophical Magazine, 3, 401-407.

10. Rayleigh. (1880). On Copying Diffraction-gratings, and on some Phenomena connected therewith. Philosophical Magazine, 11, 196-205.

11. Patorski, K. (1989). The Self-Imaging Phenomenon and its Applications. Progress in Optics XXVII. Elsevier, 1989.

12. Cowley, J.M., & Moodie, A.F. (1957.) Fourier Images: I. Proceedings of the Physical Society B, 70, 486-496.

13. Rogers, G.L. (1963). Calculations of intermediate Fourier images of a finite line grating on a digital computer, with an application to an unusual case. British Journal of Applied Physics, 14, 657-661.

REFERENCES

14. Latimer, P., & Crouse, R.F. (1992). Talbot effect reinterpreted. Applied Optics, 31, 80-89.

15. Winthrop, John T., & Worthington, C.R. (1965). Theory of Fresnel Images I: Plane Periodic Objects in Monochromatic Light. Journal of the Optical Society of America, 55, 373-381.

16. Soldano, L.B., & Pennings, E.C.M. (1995). Optical multi-mode interference devices based on self-imaging principles and applications. IEEE Journal of Lightwave Technology, 13, 615-627.

17. Tsay, S-C., & Grebel, H. (1994). Transverse holographic interconnect design. Applied Optics, 33, 6747-6754.

18. Grebel H., & Zhong, W. (1993). Holographic interconnects: transverse Bragg waveguides. Optics Letters, 18, 1123-1125.

19. Grebel, H., Graziani, J., Vijayalakshmi, S., Shacklette, L., Stengel, K., Eldada, L., Norwood R., & Yardley, J. (1997). Self-imaging chirped holographic optical waveguides. Applied Optics, 36, 9391-9395.

20. Yariv, A., & Yeh, P. (1984). Optical Waves in Crystals. Wiley-Interscience, 1984.

21. Yablonovich, E. (1989). Photonic Band Structure: The Face-Centered-Cubic Case. Physical Review Letters, 63, 1950-1953.

22. Sakoda, K. (2001). Optical Properties of Photonic Crystals. Berlin: Springer-Verlag, 2001.

23. Yablonovich, E. (1987). Inhibited Spontaneous Emission in Solid-State Physics and Electronics. Physical Review Letters, 58, 2059-2062.

24. Yablonovich, E., Gmitter, T., & Leung, K. (1991). Photonic Band Structure: The Face-Centered-Cubic Case Employing Nonspherical Atoms. Physical Review Letters, 63, 2295-2298.

25. John, Sajeev. (1987). Strong Localization of Photons in Certain Disordered Dielectric Superlattices. Physical Review Letters, 58, 2486-2489.

REFERENCES

26. Mekis, Attila, J. C. Chen, J., Kurland, I., Fan, S., Villeneuve, P., & Joannopoulos, J. (1996). High Transmission through Sharp Bends in Photonic Crystal Waveguides. Physical Review Letters, 77, 3787-3790.

27. Mingaleev, S. F., & Kivshar, Y. S. (2001). Self-Trapping of light and Nonlinear Localized Modes in 2D Photonic Crystals and Waveguides [Paper posted on arXiv: physics, http://arxiv.org/]. Retrieved April 30th, 2001 from the World Wide Web: http://arxiv.org/PS_cache/physics/pdf/0104/0104088.pdf.

28. Lin, Shawn-Yu, Hielala, V.M., Wang, L., & Jones, E.D. (1996). Highly dispersive photonic bandgap prism. Optics Letters, 21, 1771-1773.

29. Kosaka, H., Kawashima, T., Tomita, A., Notomi, M., Tamamura, T., Sato, T., & Kawakami, S. (1998). Superprism phenomena in photonic crystals. Physical Review B, 58, R10096-R10099.

30. Enoch, S., Tayeb, G., & Maystre, D. (1999). Numerical evidence of ultrarefractive optics in photonic crystals. Optics Communications, 161, 171-176.

31. Kosaka, H., Kawashima, T., Tomita, A., Notomi, M., Tamamura, T., Sato, T., & Kawakami, S. (1999). Self-collimating phenomena in photonic crystals. Applied Physics Letters, 74, 1212-1215.

32. Tobias, J.M., Ajgaonkar, M., & Grebel, H. (2002). Morphology-dependent Transmission Through Photonic Crystals. Journal of the Optical Society of America B, 19, 385-389.

33. Ochiai, T., & Sanchez-Dehesa, J. (2001). Superprism effect in opal-based photonic crystals. Physical Review B, 64, 245113-1 – 7.

34. Gralak, B., Enoch, S, & Tayeb G. (2000). Anomalous refractive properties of photonic crystals. Journal of the Optical Society of America A, 17, 1012-1020.

35. Lalanne, Philippe, & LeMercier-Lalanne, Dominique. (1996). On the effective medium theory of subwavelength periodic structures. Journal of the Optical Society of America, 43, 2063-2085.

36. Joannopolous, J. D., Meade, R.D., & Winn, J.N. (1995). Photonic Crystals. Princeton, New Jersey: Princeton Univ. Press.

37. Tobias, J.M., & Grebel, H. (1999). Self imaging in photonic crystals in a subwavelength range. Optics Letters, 24, 1660-1662.

REFERENCES

38. Bogaerts, W., Bienstman, P., Taillaeert, D., Baets, R., & DeZutter, D. (2001). Out-of-Plane Scattering in Photonic Crystal Slabs. IEEE Photonics Technology Letters, 13, 565-567.

39. Netti, M.C., Charlton, M.D.B., Zoorob, M.E., Parker, G.J., & Baumberg, J.J. (2000). Mode propagation and radiative coupling in photonic crystal waveguides. PELS-2000 Conference, Polarisation effects in lasers, spectroscopy & optoelectronics, 136-138.

40. Ajgaonkar, M., Zhang Y., Grebel H., & White, C. W. (1999). Nonlinear optical properties of a coherent array of sub-micron SiO2 spheres (opal) embedded with Si nanoparticle. Applied Physics Letters, 75, 1532-1534.

41. Pendry, J. B. (1994). Photonic band structures. Journal of Modern Optics, 293, 49-57.

42. Halevi, L, Krokhin, A., & Arriaga, J. (1999). Photonic Crystals as Optical Components. Applied Physics Letters, 75, 2725-2727.

43. Wyatt, O.H., & Dew-Hughes, D. (1974). Metals, Ceramics and Polymers. London: Cambridge Univ. Press.